POLITECNICO DI TORINO

Master's Degree in Automotive Engineering

Master's Degree Thesis

Mechanical design of Autonomous Robot for Last Mile Delivery

Supervisors

Prof. Andrea Tonoli

Prof. Alessandro Scattina

Ing. Giacomo Mussino

Candidate

Alessia Antonini

December 2022

Summary

Autonomous Delivery robots are an emerging technology aimed at resolving complexity existing in the last phase of transportation to the final customer. Their application inserts in a complicated context in which a growing emerging awareness of a need of improvement of urban mobility is forcing companies to think in smarter and greener ways to complete deliveries. For these reasons, these fully electric vehicles are thought to operate on pedestrians' domain avoiding, and simultaneously limiting, the effects of last mile delivery on traffic. Delivery accounts for 25% of all urban emissions and 20% of urban traffic is due to shipments.

The fundamental purpose of this thesis is to design a fully electric traction system that is able to allow the vehicle to deliver parcels in several districts of the city, to overcome architectural barriers, to have a sufficiently high autonomy without being a hindrance for pedestrians and therefore well integrated with the surrounding environment. From this point of view, mechanical requirements and constraints are evaluated. Since there are no published data on delivery robots application, hypothetical driving cycle was employed on common drone routes. It is based on the place of start and end of the delivery services and on the basis of the route simulations, the factors contributing to the energy demand and its variation have been analyzed. As a result of this examination the propulsion system and energy source are selected.

The idea conceived for this delivery robot is to adopt a system of four in-wheel motors that allow independent management of the torque and the possibility of steering each individual wheel. The steering and suspension systems will also be analyzed, designed not only for their natural function, but also to allow safety and adaptability to the movement of pedestrians.

To ensure the integrity of the parcels and the possibility of travelling uneven roads, simulation of the dynamic response of the vehicle's body is conducted and vertical accelerations respect to the relative displacement of the suspension where analysed. The drone is also equipped with four servo motors on each driving wheel in order to ensure the independent steering and the possibility of achieving all types of curvature except horizontal translation for reasons of encumbrance.

The result of the project is Pacci, a unique concept of delivery robot, modular and capable of transporting a large number of packages, as well as adapting the dimensions of the compartments to the user's needs. All this by exploiting existing urban infrastructures such as the bus line, modified exclusively in the back with a luggage carrier for drone transportation, to reach different areas of robot competence and to further reduce polluting emissions.

Acknowledgements

At this stage of my thesis I would want to express my gratitude to everyone who supported and assisted me with suggestions, criticisms and observations, allowing me to work in a friendly, but at the same time formal atmosphere. People always available to provide useful advice and explanations to overcome the critical issues that I gradually encountered in the development of this work. All of this has enabled me to gain a lot of knowledge and fully benefit from this significant experience..

First of all I thank my Supervisors Prof. Alessandro Scattina and Prof. Andrea Tonoli who gave me the opportunity to work on an interesting and current topic, always offering me a valid support, availability and expertise during my dissertation.

Sincere thanks to the team of the Competence Center Industry Manufacturing 4.0 and the Sustainable Mobility Technology Center , in particular to Eng. Giacomo Mussino who has allowed the realization of this project and has followed with enthusiasm the whole phase of planning directing me towards valid technical choices and making me available useful material.

I would also like to pay particular attention in thanking Prof. Carmelo Di Bartolo, who has allowed an enthusiastic collaboration with the students of the European Institute of Design in the first project phase in which the innovative concept was defined. It was a very formative experience in a new reality for me, a dynamic environment in which designers and engineers come back to discuss common choices and problems. Of fundamental importance were also Ilaria Piolanti and Prof. Michele Albera who provided the keys to understanding the working dynamics for an interaction and constructive clash between two different worlds such as engineering and design. A special thanks to the Heritage Hub that hosted us in its gallery of the Automotive world and gave us the opportunity to present our project.

My thoughts also go to all my friends with whom I shared this path that lasted five years and to those who helped me in writing the report, regarding the use of

software and the care of the foreign language. I especially thank Davide for being close to me in all the critical moments both in the academic period and in the period of writing the thesis and for having helped and supported me in the best way. I also want to thank Riccardo for sharing this experience with me, for having supported me both technically and morally, always providing me with a better perspective and for being a point of reference.

I thank my roommates Maria, Marica, Claudia and Camilla who have endured me in five years of living together and have contributed to my personal growth, with them I have established a relationship of sisterhood.

I thank all my friends who from afar followed my study path with video calls and messages. You have been fundamental, for the affection you have always shown me and for encouraging me in any academic and personal choice.

Finally, I want to express my gratitude to my parents, brother, and the rest of my family for their unwavering support and guidance during my university career, for having believed in me and actively contributed to the achievement of this important objective.

Table of Contents

List of Tables

List of Figures

Acronyms

EV

Electric vehicle

BEV

Battery electric vehicle

ADR

Autonomous delivery robot

SADR

Sidewalks autonomous delivery robot

RADR

Road autonomous delivery robot

ADV

Autonomous delivery vehicle

BLDC

Brushless DC motor

EM

Electric motor

MG

Motor generator

SOC

State of charge

DOD
Depth of discharge

FOC
Field oriented control

2WS
Two wheels steering

4WS
Four wheels steering

FRF
Frequency response function

Chapter 1

Introduction

This thesis aims to present an innovative concept design of an autonomous robot that takes care of the last mile deliveries: PACCI.

The project was born thanks to the collaboration of CIM4.0, Competence Center Industry Manufacturing 4.0 and SMTC, Sustainable Mobility Technology Center.

With the target of defining innovative engineering concepts and solutions for new urban mobility systems, the concept has been developed through a shared work between automotive engineering students of the Polytechnic of Turin and car transportation designer of the European Institute of Design of Turin.

Delivery Robot is an automated system that brings delivery directly to customer's doorstep without involving any human intervention in the entire process; delivery robot can navigate around people and public spaces thanks to their integrated sensors. The increased use of internet along with the expansion in e-commerce industry has increased the demand for product to be purchased online which requires a better and efficient means to deliver the product to the customer. Thus, various delivery services have been adopted by the companies. Our goal was to identify the shortcomings and defects of existing systems to conceive an innovative and improvement idea.

1.1 Concept description

1.1.1 Context

The first analysis that was undertaken was the environmental context in which Pacci will be set, with a careful research of the issues related to the last mile.

In Italy, the volume of deliveries that moves every month is estimated at 15 million euros. The transport sector in Italy is responsible for 1/4 of greenhouse gas emissions; in particular, 92.6% of emissions are produced by road transport.

Use electric vehicles to combat pollution is a solution of the present that must be exploited. [1]

Take into consideration environmental aspect 25% of all urban emissions are due to delivery and 20% of urban traffic is due to shipments. In addition, a 200% increase in deliveries is expected by 2030. Regarding the scenario of the enterprises 53% of the shipping costs are due to the last mile, 14.7 euros for every returned and the 8% of the first attempts of shipment fails. From the consumer's point of view 2/3 of the people prefer the delivery at the door and 95% of the deliveries fail because the customer is not at home. The concept also aims to improve the delivery mode for people with disabilities, given that 7 million people with disabilities have problems with weekly deliveries. The aim is to create an inclusive design that can also allow people with limited mobility to access the delivery service. In Italy there are about 150,000 people with reduced mobility.

1.1.2 Operating scheme

The aim of the system is to exploit the existing infrastructure in the cities such as buses. A change on the back will allow the drones to be placed in their special drone carrier. Each drone has an area of expertise in which it will carry out its task, this area includes areas of about a kilometer radius. The drone will reach its zone of action for the delivery of packages thanks to the use of the bus that will cover the longest stretch of the route, will carry out its mission and will resume a bus. The diagram below explains in detail the functionality of the entire shipping system. Fig 1.1, and 1.2

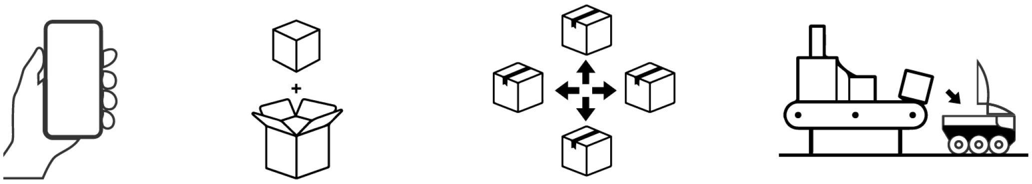

1. Received order

2. The order shall be prepared and packed

3. Orders are arranged by location

4. Orders are loaded into drones (by location and route number)

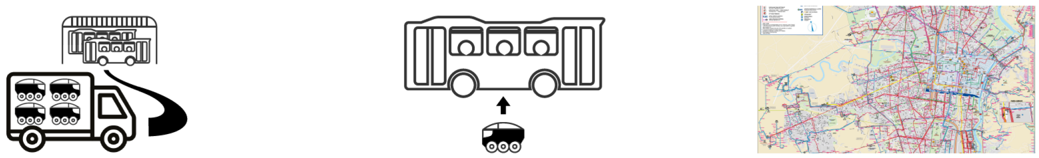

5. Filled drones are left at the corresponding bus stop

6. Drones are loaded into the bus

7. Buses proceed on their usual route

Figure 1.1: Diagram of the entire shipping system

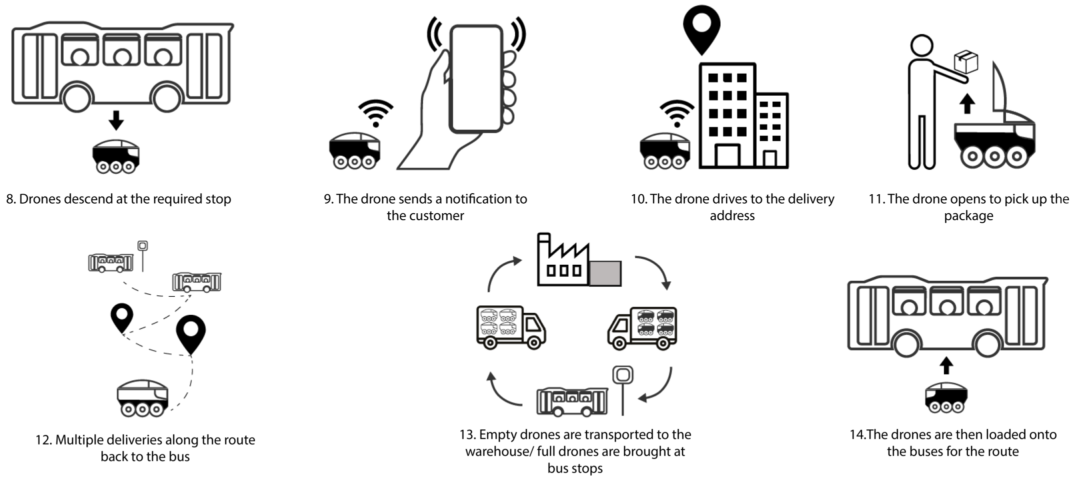

Figure 1.2: Diagram of the entire shipping system

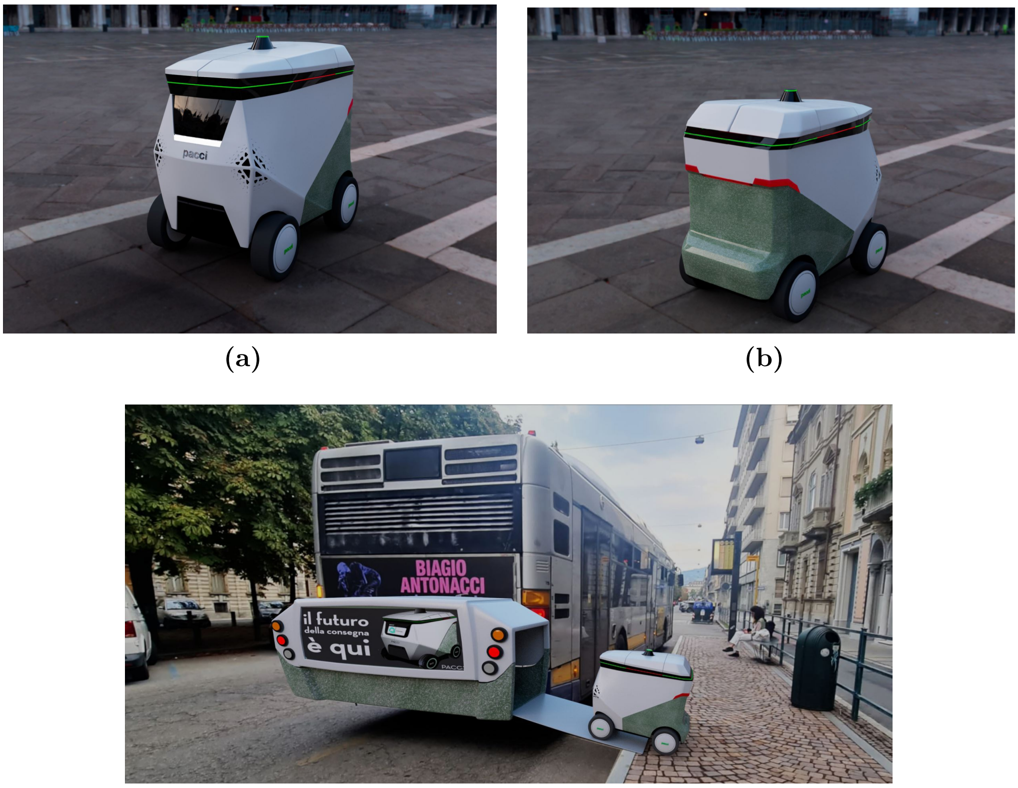

(a) (b)

(c)

Figure 1.3: Concept design of Pacci immersed in the urban context

1.1.3 Drone design

The design of the drone has been conceived so that it is perfectly integrated with the surrounding environment. Being able to travel both in the streets and on the sidewalks it must constantly interact with pedestrians and be able to move and maneuver. The Drone is designed so that it had a friendly appearance a sustainable behaviors and curvilinear shapes. The resulting surfaces are rounded for safety reasons in the event of impact. In figura 1.4 the drone is shown in all its profiles and the luggage carrier that will be applied behind the buses.

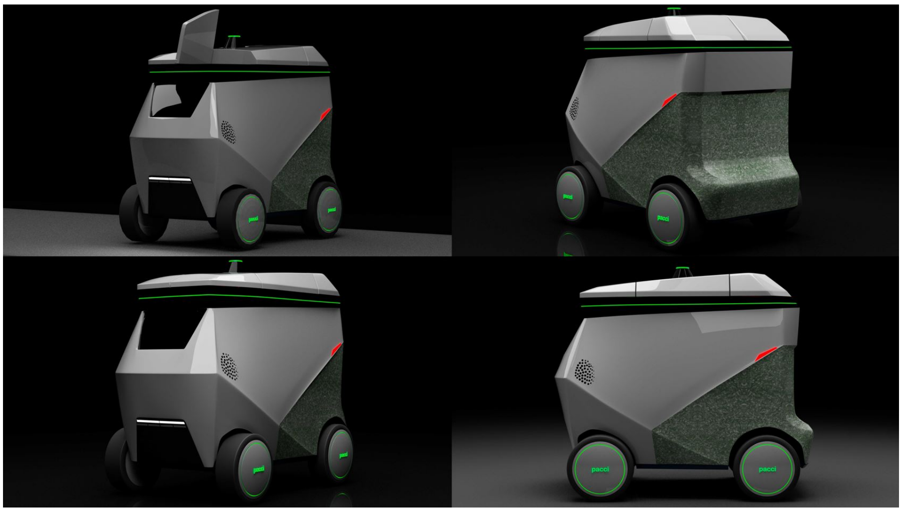

(a) *Pacci*

(b) *Pacci house*

Figure 1.4: Different profiles images of robot Pacci and its cabin

Dimension

Ground height and dimensions are set so that the robot can be able to climb steps, ramps and footrests. The front dimension of the drone is similar to that of a person so as not to be in the way of his movements. The user can autonomously interact with the drone with the aim of picking up or sending a package. It has been important therefore in the analysis of the dimensioning of the drone the necessity to favor the activities of withdrawal of the package from the consumer. Pacci must not be too low to force the user to bend down to pick up his package, but not too high to be difficult to reach for people who are disabled in a wheelchair. Another prerequisite taken into account is the capacity of the drone. Being programmed to provide an entire neighborhood, about one square meter of area, Pacci will have to contain a fairly large number of small parcels. The final dimensions of the drone are shown in the figure 1.5

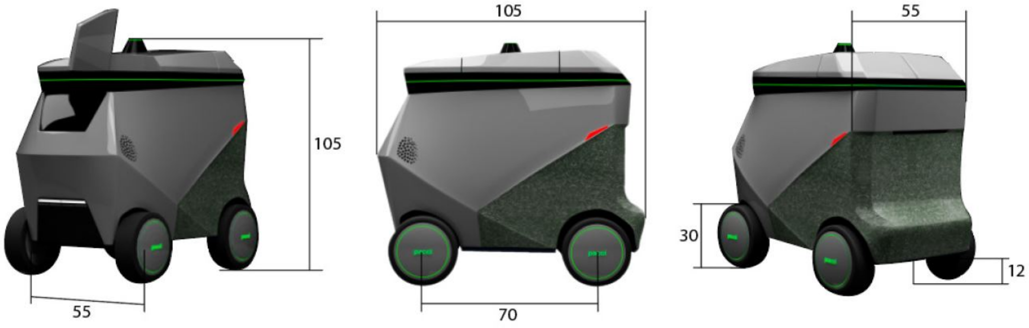

Figure 1.5: Drone dimensions in centimeters

Parcel extraction

What gave our drone its conformation is the package extraction system. This is in fact of considerable importance as it must ensure easy collection of the package by the customer and make sure that the latter should not lean or bend over to the drone. It will therefore be the package to rise outside the drone thanks to a system of piston as we can see in the image 1.6 where the piston runs its guide until reaching the package to be extracted. The compartments that contain the package have a variable volume thanks to a system of folding doors that open in case the package is large. The upper flaps for the exit of the pack are designed to have the size of the smallest compartment. At this point, when a larger pack of the smallest has to be extracted, more consecutive doors will open. This mechanism allows not to have fixed compartments but to be able to carry any package size. The only limitation will be a partition panel in the middle of the drone that will divide the latter into two regions.

From this we can then define the dimensions of our vehicle that are as much as possible integrated in an urban and human context will then have a maximum carriageway of 55 cm that is equal approximately to the width of a pedestrian and a wheelbase of 70 cm.

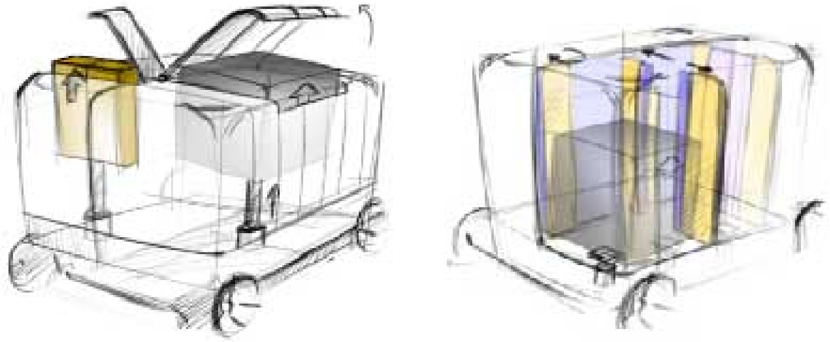

Figure 1.6: Package extraction mechanism with piston and folding flaps

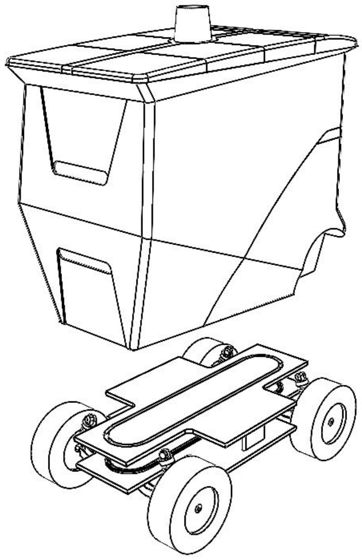

Figure 1.7: Upper cabin on the drone platform

Robot components

The choice for the motion transmission system is four electric motors integrated in the wheels that allow a system of 4 steering wheels. We have adopted tubless tires, disc brakes and suspension type Mcpherson. The main reason for this choice is to want to simulate the human trend, in this way in fact the Drone can make its movements between pedestrians by rotating all four wheels and then be more camouflaged in the context. 250 watt electric motor will allow the vehicle a maximum speed of about 30 km/h in flat and 26 Km/h on a 15% gradient This vehicle will have a range of about 30 km estimated through a simulated route that presents numerous standard situations that the drone will be to sheep such as climb traffic lights, stops for parcel deliveries, the most crowded areas of the city center and various gradients such as ramps and cobblestones. This path will also be useful for the study of the suspension system in which the done is examined in different load situations and therefore of centre of gravity.

As for the devices that the drone is equipped with so that it can move independently we have the Lidar, indispensable so that Pacci can recognize the surrounding environment and then know how to distinguish a stationary object on the roadside from a person walking next to it, this device in fact is able to recognize and catalog what is around (unlike a radar sensor), proprioceptive sensors that serve to monitor the status of the drone itself, and then angular velocity to the wheels, moments to the wheels, steering angle of the wheels, accelerations and also the pressure of the wheels so you can handle an emergency situation as in the case of a perforated wheel, and finally mounts four stereocamers.

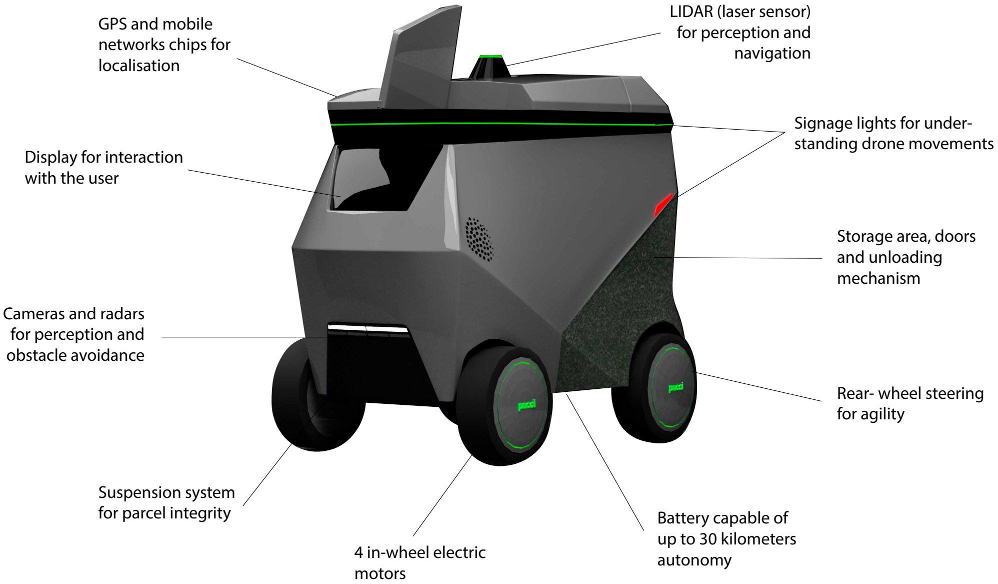

Figure 1.8: Main components of delivery robot Pacci

Chapter 2

State of the art - Delivery robots

In this section, analyzing the environmental and social background and the issues related to the last mile, emerge the main reasons that led to the birth of our autonomous delivery robot called Pacci. This chapter aims to survey the existing research and review the literature on ADR-based delivery systems and related operations. Foremost, we discuss various technology, design, and legal factors that impact ADR operations. Subsequently, we are the first to review the state-of-the-art research in ADR-based deliveries concerning the following areas: infrastructure and fleet planning, factors affecting efficiency, technology acceptance, and social intelligence.

2.1 Background

The rapid growth of the e-commerce industry, whose deliveries are characterized by small package sizes, high volume, and varying frequency, poses serious challenges for logistics service providers [2]. Additionally, e-commerce expanded two to five times faster in 2020 than it did in the past in the majority of nations, including the United States, China, the United Kingdom, Spain, Germany, India, France, and Japan.[3]. Particularly noteworthy are the enormous gains in the food, grocery, and medication delivery businesses. For instance, the worldwide market for food delivery quadrupled over the preceding five years to reach 150 billion, with the US industry alone experiencing a two-fold increase during that time.[4] Due to the instantaneous and on-demand nature of food, medication, and grocery deliveries, the astronomical growth rates in these industries have made logistical difficulties even more severe. Fig. 2.1 outlines the major difficulties that delivery services face, including rising consumer demands, high prices, a severe labor shortage, and sustainability issues.

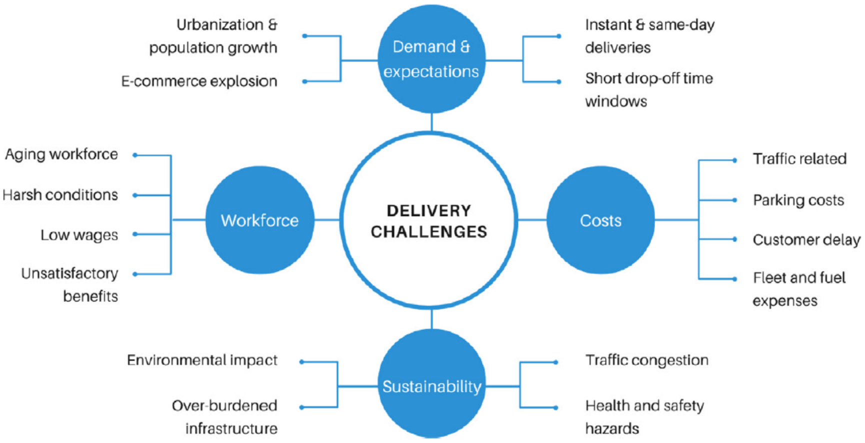

Figure 2.1: Conventional delivery challenges

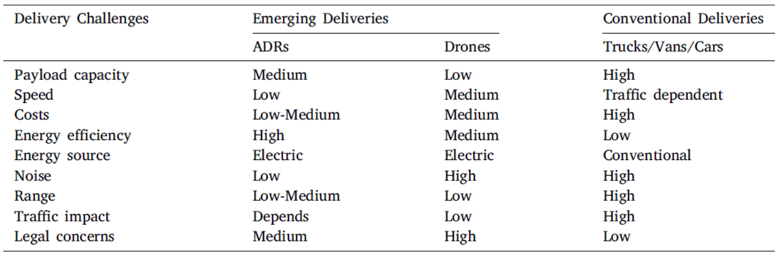

Delivery Challenges	Emerging Deliveries		Conventional Deliveries
	ADRs	Drones	Trucks/Vans/Cars
Payload capacity	Medium	Low	High
Speed	Low	Medium	Traffic dependent
Costs	Low-Medium	Medium	High
Energy efficiency	High	Medium	Low
Energy source	Electric	Electric	Conventional
Noise	Low	High	High
Range	Low-Medium	Low	High
Traffic impact	Depends	Low	High
Legal concerns	Medium	High	Low

Figure 2.2: Overview of emerging and conventional delivery methods.

In addition, the current rates of urbanization and population expansion have made the already problematic delivery problems in polluted and congested cities worse. Within the next ten years, it is anticipated that the top 25 US cities with the highest traffic will lose over 480 billion as a result of rising fuel use, lost productivity, and carbon emissions [5]. For addressing higher delivery quantities, rising consumer expectations, and other conventional delivery issues, new, creative, efficient, and automated delivery techniques have thus become essential. Currently, a large number of multinational corporations, start-ups, and worldwide research organizations are concentrating on utilizing airborne drones and autonomous ground robots, also known as Autonomous Delivery Robots (ADRs), to reinvent deliveries and address current difficulties. Utilizing these autonomous delivery methods provides benefits for all stakeholders: 1) individual customers, 2) business owners, and 3) community. Autonomous innovations assist consumers with quick deliveries, and business owners profit from expanded reach and revenues. Overall, the neighborhood benefits from less traffic and pollutants from vehicles, and people also have better lives because to greater access to commodities. Despite the fact that autonomous aerial drones and ADRs offer comparable advantages, each technology nevertheless has its own operational advantages and disadvantages. Table 1 compares ADRs, drone deliveries, and traditional deliveries in an overview of key areas. Notably, aerialdrones can travel at higher speeds and in direct Euclidean paths, putting the ADR at a disadvantage [6]. However, ADRs are superior to drones in numerous aspects. For instance, ADRs can make up for their slower speeds with many deliveries in a single trip thanks to their multiple compartments, increased payload capacity, and extended operational range. Similarly, even while drones and ADRs assist reduce carbon emissions from transportation, in medium to high wind situations, drones use roughly 3–10 times more energy than electric ground vehicles (applicable to ADRs). Additionally, drones can use more energy than diesel delivery vehicles in situations with more customers and stops (like dense urban settings). ADRs are also seen positively in legislative frameworks, in addition to the design and operational advantages already highlighted, because drones are thought to pose greater risks to individuals and public infrastructure.

Similarly, drones also contribute to noise pollution, which can soon become a public health issue, while ADRs are both safer and quieter. The ADRs used for delivery applications nowadays can be classified into one of the following groups based on their design and operational capabilities: Road Automatic (or Autonomous) Delivery Robots (RADRs), Sidewalk Automated (or Autonomous) Delivery Robots (SADRs), or Autonomous Delivery Vehicles (ADVs) are three examples of autonomous delivery vehicles [7]. (see Fig. 2.3). Additionally, ADR-based deliveries might also be supported by traditional vehicles like motherships and rely on infrastructure like robot depots and robot stations. The terms used frequently in the literature on ADR-based delivery are included in Table 2.3.

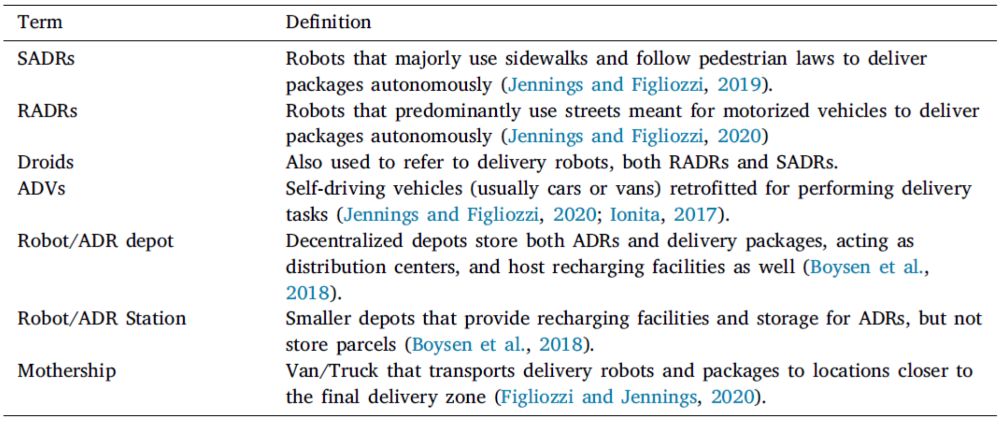

Term	Definition
SADRs	Robots that majorly use sidewalks and follow pedestrian laws to deliver packages autonomously (Jennings and Figliozzi, 2019).
RADRs	Robots that predominantly use streets meant for motorized vehicles to deliver packages autonomously (Jennings and Figliozzi, 2020)
Droids	Also used to refer to delivery robots, both RADRs and SADRs.
ADVs	Self-driving vehicles (usually cars or vans) retrofitted for performing delivery tasks (Jennings and Figliozzi, 2020; Ionita, 2017).
Robot/ADR depot	Decentralized depots store both ADRs and delivery packages, acting as distribution centers, and host recharging facilities as well (Boysen et al., 2018).
Robot/ADR Station	Smaller depots that provide recharging facilities and storage for ADRs, but not store parcels (Boysen et al., 2018).
Mothership	Van/Truck that transports delivery robots and packages to locations closer to the final delivery zone (Figliozzi and Jennings, 2020).

Figure 2.3: Common terminologies in ADR-based deliveries.

2.2 ADR-based deliveries

The use of drones for last-mile delivery has been the subject of numerous studies, but ADR-based delivery research is still in its infancy. However, a number of businesses, including Amazon, Walmart, and FedEx, currently use ADRs to carry out their delivery tasks. The current robot-aided delivery routing model can be divided into the following three categories based on the system features.

- • Two-tier model: In the first tier, conventional vehicles are in use and move a sizable volume of parcels from a central depot to regional hubs (here ADR depots). These packages are delivered to the end users by the ADRs working in the second tier.(see Fig. 2.4-a);
- Mothership model: Traditional trucks and vans are converted into a "mothership" system to transport and store many SADRs. In this approach, the mothership visits several neighborhoods and sends out its SADRs with parcels to deliver to the clients there.(see Fig. 2.4-b);
- Platoon model: When traveling in non-AV zones, RADRs join a manual vehicle lead platoon, a group of closely spaced vehicles moving nose-to-tail while driving in unison. (see Fig. 2.4-e). The following subsections will formally describe the three problems and review related literature.

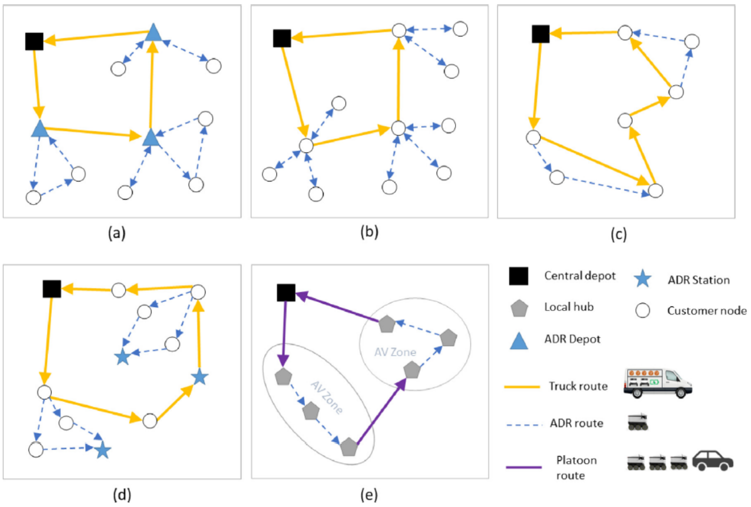

Figure 2.4: Overview of prevalent routing concepts in ADR-aided hybrid delivery literature: (a) two-tier, (b) mothership (dispatch–wait–collect), (c) mothership (dispatch–move–collect), (d) mothership (dispatch-leave), (e) platoon model.

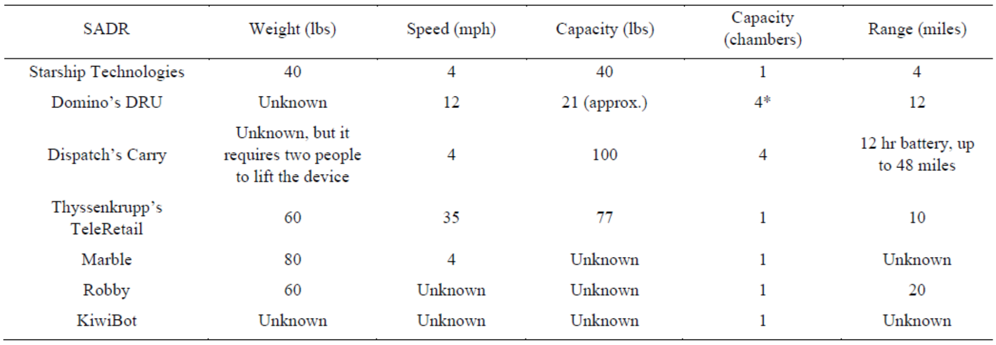

SADR	Weight (lbs)	Speed (mph)	Capacity (lbs)	Capacity (chambers)	Range (miles)
Starship Technologies	40	4	40	1	4
Domino's DRU	Unknown	12	21 (approx.)	4*	12
Dispatch's Carry	Unknown, but it requires two people to lift the device	4	100	4	12 hr battery, up to 48 miles
Thyssenkrupp's TeleRetail	60	35	77	1	10
Marble	80	4	Unknown	1	Unknown
Robby	60	Unknown	Unknown	1	20
KiwiBot	Unknown	Unknown	Unknown	1	Unknown

Figure 2.5: SADRs Specifications

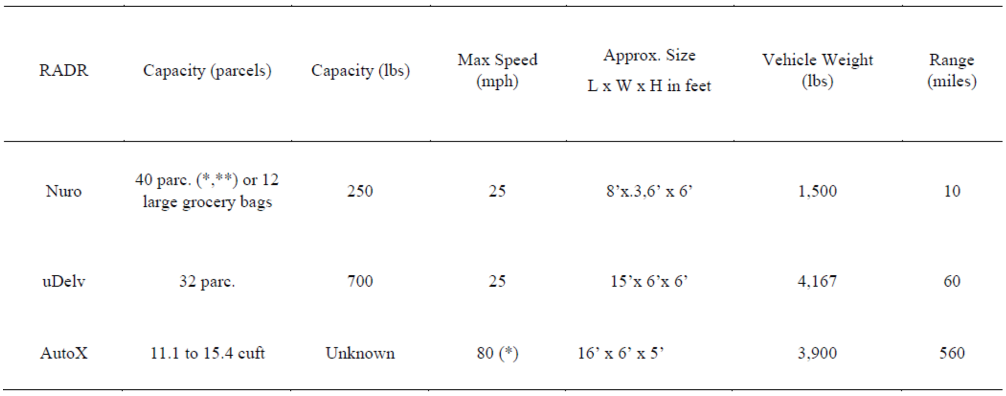

RADR	Capacity (parcels)	Capacity (lbs)	Max Speed (mph)	Approx. Size L x W x H in feet	Vehicle Weight (lbs)	Range (miles)
Nuro	40 parc. (*,**) or 12 large grocery bags	250	25	8'x.3,6' x 6'	1,500	10
uDelv	32 parc.	700	25	15'x 6'x 6'	4,167	60
AutoX	11.1 to 15.4 cuft	Unknown	80 (*)	16' x 6' x 5'	3,900	560

Figure 2.6: RADRs Specifications

Table 2.5 compares the five SADRs discovered and demonstrates that the majority of the vehicles are rather slow and light due to rules in many towns and states that place restrictions on speed and gross weight.

Table 2.6 compares the three RADRs found. New designs like NURO are significantly lighter and smaller than traditional delivery vehicles. The other two cars (uDelv and AutoX) are based on currently used conventional cars or chassis that have been automated or slightly modified to accommodate autonomous delivery. Although NURO is lighter and smaller than traditional cars, it has a lower capacity and shorter range. Specialized vans, often referred to as "mothership" vans, can be used to drop-off and pick-up several RADRs. See Figure 2.7(d). However, even the smallest RADRs are made to drive independently and share the road with regular powered vehicles.

(a) *SADR (Kiwibot)* **(b)** *RADR (Nuru)*

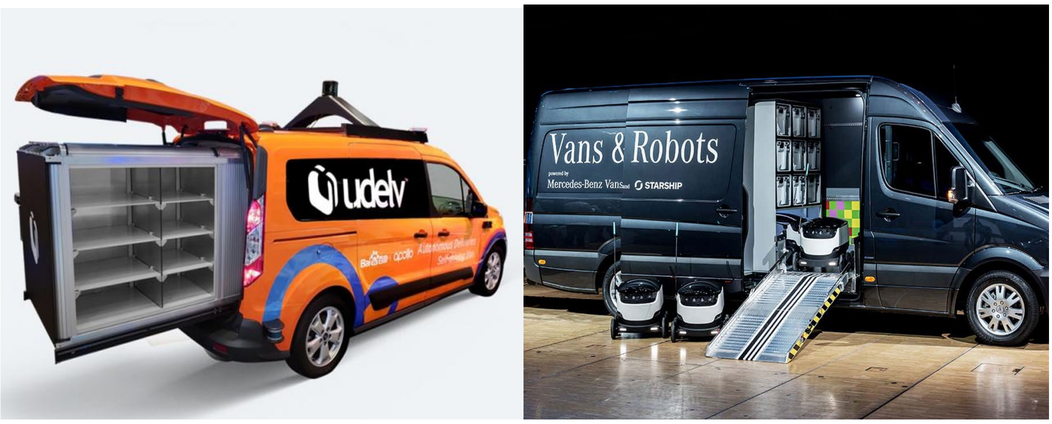

(c) *ADV (Udelv)* **(d)** *Mothership (Mercedes - Benz).*

Figure 2.7: Different ADR concepts currently employed

Customers are already being served by small robot cars like KiwiBot, Starship, and Amazon Scout, among other experimental locations. These delivery robots mostly deliver takeaway food. Due to its close-spaced four wheels, the KiwiBot is prone to tipping over on curbs and other uneven surfaces. Additionally, it is considerably smaller than the other two. Starship and Amazon Scout both feature three wheels on each side of the robot, which is a comparable design. Starship began operations years before Amazon Scout and uses dynamic suspension to climb obstacles. However, Starship has an inherent limitation of small wheeled robots in that it can only go over shallow snow (less than 2 cm) [8].

2.2.1 Improvements on distance travelled

Quantifying variations in the distance traveled by commercial vehicles is crucial for freight planning. The percentage decrease in mothership van on-road travel when SADRs are used is seen in Table 2.8. When client density is low and the service region is all around the SADR depot, the reductions are at their maximum or $d = 0$. In Table 2.8, it is assumed that the SADR mothership van still needs to travel across the service area in order to discharge and pick up the SADRs. If motherships are not necessary, there is a 100% decrease in trip costs (i.e. no on-road travel). New SADR traffic on sidewalks is negatively impacted by the decrease in on-road travel. As density rises, SADR sidewalk travel rises by 2, 4, and 8 correspondingly. According to what is covered in the last part, this generates additional externalities and possible problems.

Long-haul travel d (kms)	Density			
	Low	Medium	High	Very high
0*	18.4%	18.4%	18.4%	18.4%
5	15.0%	12.7%	9.7%	6.6%
10	12.7%	9.7%	6.6%	4.0%
15	11.0%	7.9%	5.0%	2.9%
20	9.7%	6.6%	4.0%	2.3%
25	8.7%	5.7%	3.4%	1.9%
30	7.9%	5.0%	2.9%	1.6%
35	7.2%	4.5%	2.5%	1.4%
40	6.6%	4.0%	2.3%	1.2%

Figure 2.8: Percentage reduction of on-road distance traveled

2.2.2 Improvements on energy consumption

By dividing the distance traveled by the energy efficiency of each vehicle, the energy required to deliver to 48 clients was calculated. Estimating the mothership van's and the delivery robots' contributions is crucial in the case of SADRs. Table 2.9 lists the outcomes for each kind of vehicle in two improbable situations (low density and very high density). Two conclusions are immediately observable: The mothership van uses more energy than the eight SADRs do for the following reasons: 1) the mothership van uses more energy than the eight SADRs do; and 2) high density and short long-haul distance have a significant influence on overall energy consumption. Table 2.10 presents the RADR values for each vehicle type in the identical two severe circumstances (low density and very high density). Three conclusions can be drawn: 1) the energy consumption of the NURO and UDelv is only a small portion of the energy consumption of the mothership van, which is reported in Table 2.9; 2) the NURO is severely constrained by its short range of 10 miles (16.09 kilometers) and can only operate in scenarios with $d < 10$ kilometers; and 3) the NURO only outperforms the UDelv in terms of energy efficiency when the density is extremely high. These findings suggest that the compact NURO could only be the most effective vehicle in densely populated metropolitan areas with heavy traffic and little parking. In every other situation, the Udelv is more effective. ADRs are significantly more energy-efficient than ordinary diesel vans, drones, and unmanned aerial vehicles when compared to other vehicle types.

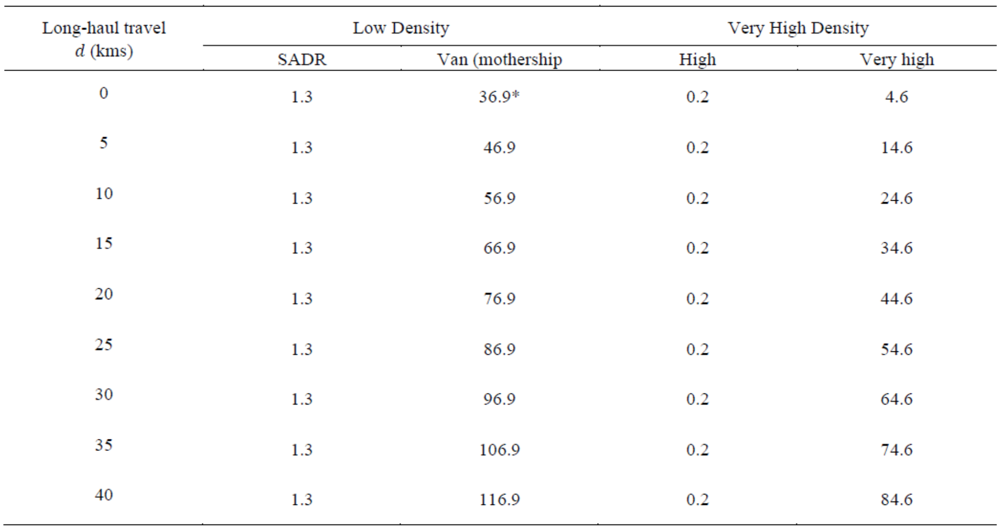

Long-haul travel *d* (kms)	Low Density		Very High Density	
	SADR	Van (mothership	High	Very high
0	1.3	36.9*	0.2	4.6
5	1.3	46.9	0.2	14.6
10	1.3	56.9	0.2	24.6
15	1.3	66.9	0.2	34.6
20	1.3	76.9	0.2	44.6
25	1.3	86.9	0.2	54.6
30	1.3	96.9	0.2	64.6
35	1.3	106.9	0.2	74.6
40	1.3	116.9	0.2	84.6

Figure 2.9: SADRs Energy consumption in kWh

2.2.3 Improvements on emissions, vehicle size, and safety

Emissions are not reported but can be discussed by taking into account that each kWh generated from diesel fuel generates 22.5 more CO_2 emissions than the emissions generated to produce one Kwh from the electric grid [7]. Hence, the conventional SADR mothership van is hardly appealing in terms of CO_2 emissions.

In conclusion, Sidewalk autonomous Delivery Robots (SADRs) might be a practical substitute for conventional delivery vehicles if they are utilized in combination with a mothership van to transfer them to and from service sites. According to this research, SADRs have the potential to dramatically cut on-road vehicle miles traveled as well as delivery times and costs when compared to traditional deliveries

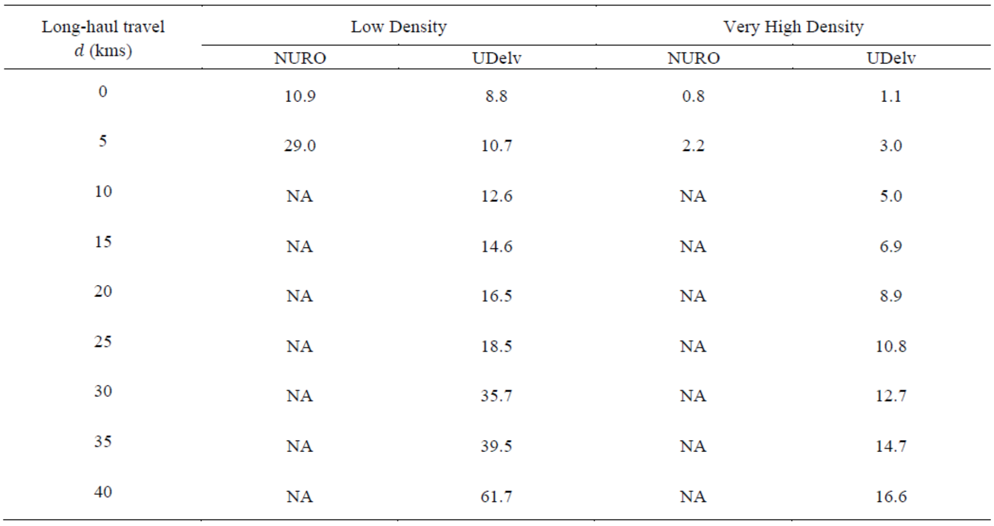

Long-haul travel d (kms)	Low Density		Very High Density	
	NURO	UDelv	NURO	UDelv
0	10.9	8.8	0.8	1.1
5	29.0	10.7	2.2	3.0
10	NA	12.6	NA	5.0
15	NA	14.6	NA	6.9
20	NA	16.5	NA	8.9
25	NA	18.5	NA	10.8
30	NA	35.7	NA	12.7
35	NA	39.5	NA	14.7
40	NA	61.7	NA	16.6

Figure 2.10: RADRs Energy consumption in kWh

in specific circumstances, assuming present SADR attributes are maintained. When service locations are located distant from the depot, the implementation of SADRs could not be as successful as the deployment of RADRs in terms of energy usage, emissions, and parking utilization.

2.2.4 Costs reduction

It is understandable that the last mile expenses for package deliveries are greater than half of the total transportation cost due to many pauses, heavy traffic, and tiny package delivery [9] . By 2025, robots might complete up to 85% of all last-mile deliveries, according to a McKinsey prediction [10]. This forecast is subject to public opinion, laws, and labor prices. When an autonomous delivery robot (ADR) is used in place of a human delivery person, it is predicted that the cost of delivery would decrease by 40%. According to McKinsey, two thirds of customers choose the least expensive home delivery option, proving that delivery is a price-sensitive industry. The labor cost can be greatly reduced by using a robot deliverer rather than a person.

The last delivery mile is the most expensive part of the route from the supplier to the client, often accounting for up to 53% of the overall expenditures. As autonomous delivery robots expand, the cost of a last-mile delivery, which is currently 1.60 dollars via human drivers, might plummet to just 0.06 dollars, as demonstrated below. Fig. 2.11

Because of its complexity and accompanying personnel expenses, the final mile of delivery is disproportionately expensive and polluting. Robots can help businesses

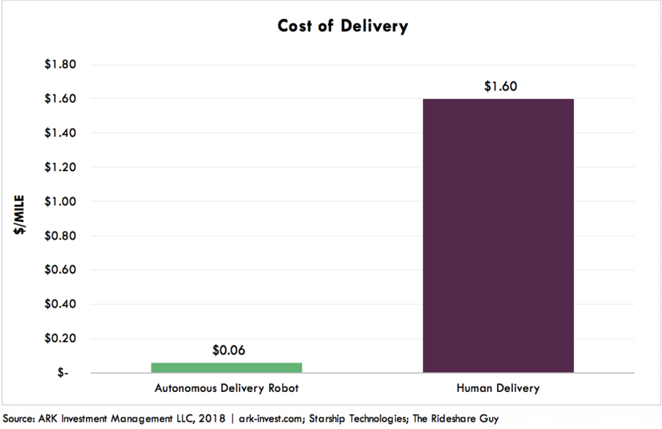

Figure 2.11: Cost comparison between human delivery and robot delivery

gain a competitive edge and solve this puzzle.

2.2.5 Segmentation of delivery robot market

The delivery robot market is segmented on the basis of load carrying capacity, number of wheels end user application and region. Thanks to the graph 2.12 we had a starting point for the construction of our drone in such a way that it reflected the needs of the customer and was as respectful as possible of the most lucrative segments.

Boxbot, Cleveron AS, Kiwibot, Ninebot, Nuro, Robby Technologies, and Starship Technologies are some of the major companies competing in the worldwide delivery robot business.

As we can see from Figure 2.12, based on number of wheels, the market is divided into three categories: 3 Wheels, 4 Wheels, and 6 Wheels. Because of its superior turning radius and shorter separation between the front and back wheels, the 4-wheel sector is predicted to dominate the market. The market is divided into three categories based on load carrying capacity: 10 Kg, More than 10 KG up to 50 Kg, and more than 50 Kg. Throughout the projection period, robots with a weight carrying capability of 10 to 50 Kg are anticipated to dominate. This is as a result of its widespread use in the retail sector. And finally as regard End User Industry, the market is segmented into Food and Beverages, Retail, Healthcare, Postal, and Others. Food and Beverages has the maximum chance of adopting delivery robots at a very high rate, but also the shipment of parcels which is what interests us in our application has a high potential.

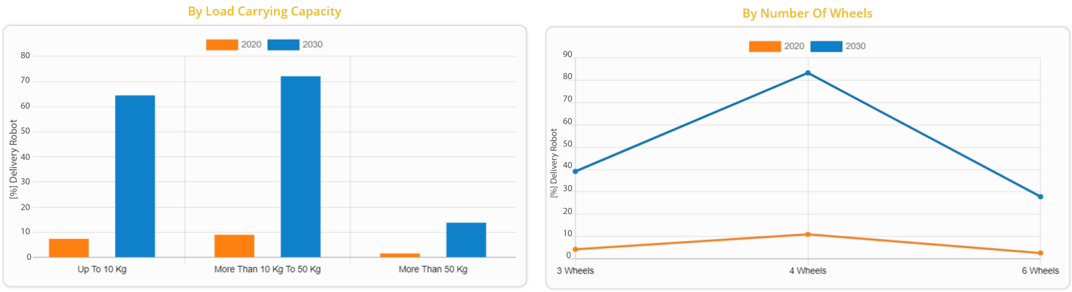

(a) *Load* **(b)** *Wheel*

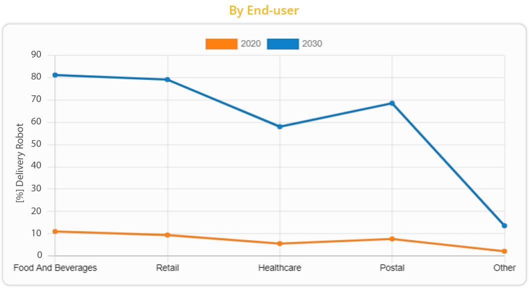

(c) *Utility*

Figure 2.12: Segmentation of delivery robot market

Chapter 3

Traction system

The idea conceived for this delivery robot is to adopt a system of four in-wheel motors that allow independent management of the torque and the possibility of steering each individual wheel. It is important to integrate the drone with the surrounding environment and this steering mode will allow the drone to move smoothly between people and obstacles placed on the sidewalks. The presence of four motors will also be useful as a safety system, in the event of a malfunction of one of the 4 motors the drone will not get stuck in the middle of the road where it could be cluttered. In the next paragraphs we proceed with the analysis of the design constraints, calculation of the power and torque required by the vehicle and then with the sizing of the electric motors and their control system. Powertrain architecture is composed as shown in figure 1, with a FOC controller for each brushless DC electric motor and a battery pack in a central position that powers the four motors.

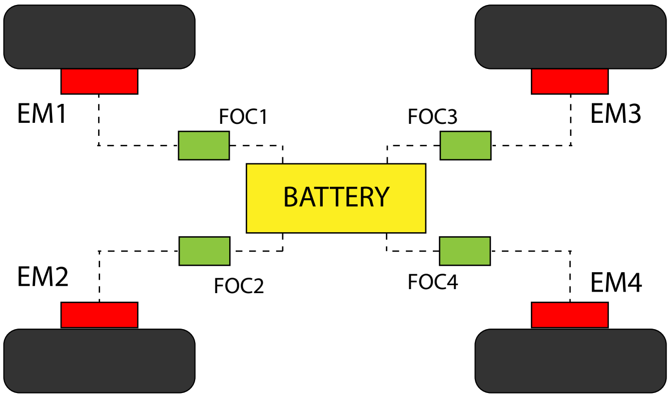

Figure 3.1: Powertrain architecture

3.1 Design requirements of propulsion system

3.1.1 Robot driving cycle

To better predict the type of propulsion to be adopted for this specific vehicle, it is important to find a driving cycle that can better represent real driving situations instead of using predefined standard driving cycles. A simulated route was therefore created, considering the area of competence for each drone of 1 km radius in which Pacci will get off the bus, make its deliveries or any returns and then go to the bus stop assigned to it. We have chosen to take the San Salvario area of Turin as a reference because this presents numerous standard situations that the drone will find itself on, such as climbs, traffic lights, more crowded areas of the city centre and various gradients such as ramps and cobblestones.

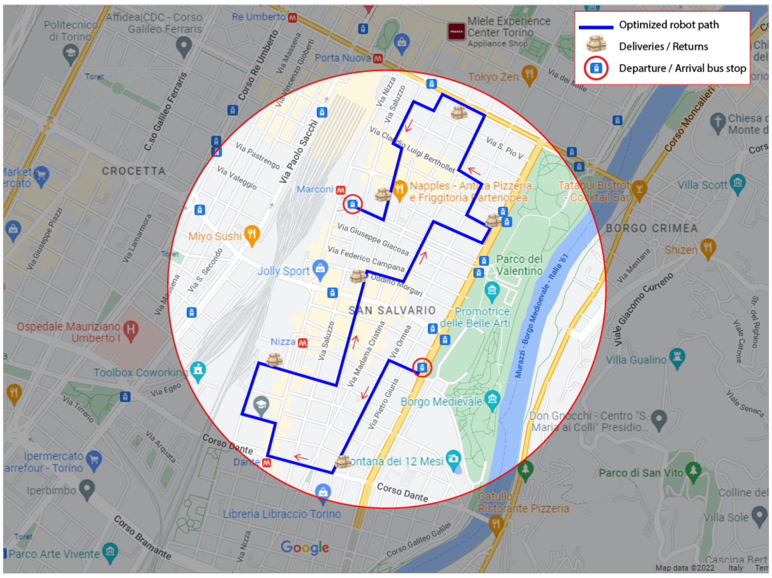

Figure 3.2: Robot parcel delivery route in a district of the city

From this simulated route, the powers required by the vehicle to tackle the journey were taken into consideration, setting the achievement of a maximum speed of 30 Km/h in urban areas, 20 Km/h on city streets and finally 6 Km/h in pedestrian areas or on the sidewalks. The drone is analyzed in operating condition of all four engines at the same time for the completion of the route. The analyzed route includes a total length of 7 Km .

Drone driving cycle is customized according to the following situations:

- Frequent changes in speed due to the path between pedestrians, ramps and obstacles

- Get off and get on the sidewalk
- Stop at the Traffic Light with a duration ranging from 40 to 60 seconds
- Short stops due to pedestrian crossing, about 5-7 seconds
- Long stops due to the delivery of the package of varying duration from 2 to 5 minutes, according to customer needs
- Maximum flat speed of 30 Km/h
- Smooth accelerations up to 2,1 m/s^2
- Average speed of 8,5 Km/h considering also the times at zero speed
- Cycle length considered 1493 seconds
- Distance travelled in a cycle 3,5 kilometres

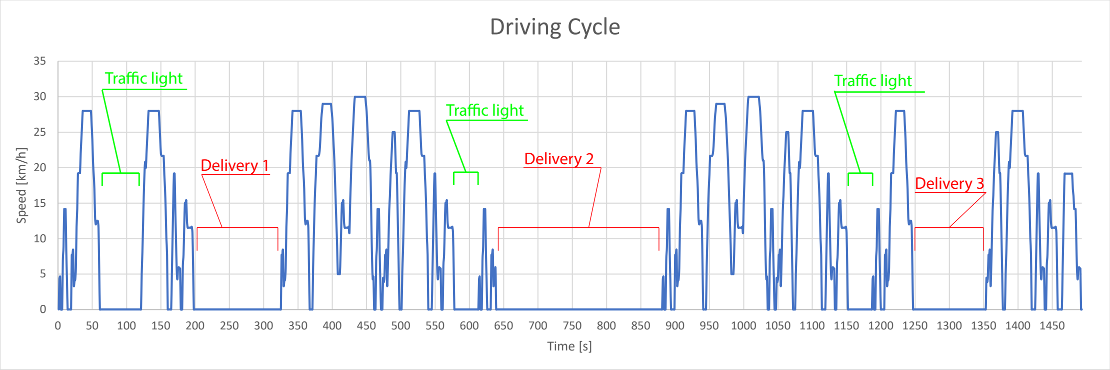

Figure 3.3: Robot's driving cycle

Parameters	Values	Unit
Duration	1493	s
Distance	3,5	km
Avg. speed	8,5	km/h
Avg. acceleration	0.13	m/s^2
Max speed	30	km/h
Max acceleration	2,1	m/s^2

Table 3.1: Data of the dedicated driving cycle

As we can see from figure 3.3 during a driving cycle the examined drone will meet 3 red traffic lights and will be able to make 3 deliveries to customers, this means that in the simulated path in figure 3.2 having length around 7 kilometers, Pacci will carry out about 6 deliveries in its zone of action. The duration of a mission in fact, in an area of competence of the drone lasts about an hour, that is two driving cycles of 1493 seconds covering 3,5 kilometers. At this point the robot can take the bus and move to his new work area. In the chapter dedicated to the analysis of the energy demand it comes estimated the number of cycles that the robot will be able to complete before being completely discharged.

Thanks to the above driving cycle the force, torque, and power dimensioning procedures are performed, which will lead to the choice of the propulsion system. Then, it will also be used for the estimation of regenerative braking abilities along with the energy analysis.

3.1.2 Longitudinal dynamics of the vehicle

To evaluate the longitudinal dynamic behavior of the vehicle, it is implemented the equations proposed by [11] and [12] for a conventional vehicle adapted for an EV configuration. The model is based on the movement resistance forces as the rolling and climbing resistance, aerodynamic drag and vehicle acceleration. The propulsion drive design of a battery electric vehicle is obtained by the maximum cruising speed, gradeability and acceleration desired.

Before proceeding with the analysis of the longitudinal dynamics of the vehicle it is necessary to specify some adopted simplifications of a practical nature:

- deformation that occurs on the tire towards the direction of motion that is a consequence of the mechanical characteristics of the same, is not considered; consequently there will be no displacement towards the direction of motion of the contact point between wheel and ground or the effective rolling radius;
- aerodynamic lift are neglected;
- the coefficient of adhesion between wheel and ground does not depend on speed but coincides with the μ_r value;

For propelling, the BEV motors generates a traction effort in the contact area between the tires of the driven wheels and the road surface. This effort should exceed the total resistive force F_{total} completely determined by a fourdimensional vector:

$$F_{total} = F_a + F_r + F_c + F_d \tag{3.1}$$

consisting of the following components: the aerodynamic drag force F_a, the rolling resistance force F_r, the climbing force F_c, and some additional disturbance described as F_d which summarises other effects, but which can be neglected.

The aerodynamic drag force considers three aerodynamic effects, such as the friction resistance of the air flow skin in the boundary layer, the induced drag due to

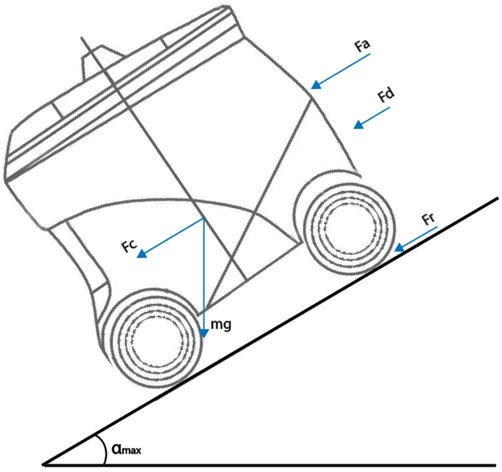

Figure 3.4: Free body diagram of the different longitudinal forces acting on the vehicle

the downwash of the trailing vortexes behind the vehicle, and the normal pressure resistance around the Robot. The first two factors are usually small compared to normal pressure resistance and are therefore generally neglected. Therefore, the remaining air friction is as follows:

$$F_a = \frac{1}{2}\rho C_d A_f v^2 \tag{3.2}$$

Where

- ρ air density;
- C_d dimensionless aerodynamic drag coefficient;
- A_f area of the vehicle front;
- v vehicle speed,

The rolling resistance force, wheels friction, is due to the deformation of the wheel and the road surfaces. The factors affecting the wheels friction are the tire types, pressure, temperature, BEV speed, thread thickness. This force is expressed as follows:

$$F_r = \mu_r M_v g \cos\alpha \tag{3.3}$$

Where

- M_v total mass of the vehicle;

- α slope angle of road;
- μ_r dimensionless wheel friction factor;

Finally the gravitational force influences considerably the vehicle behaviour as follows:

$$F_c = M_v g \sin\alpha \tag{3.4}$$

3.1.3 Power and Torque estimation

The robot model is a backward-facing model, which means that the robot is assumed to follow the speed profile exactly and the energy consumption is calculated based on that behavior.The traction power required for keeping the BEV at the desired speed of the driving cycle is as follows:

$$P_{trac}(t) = M_v v(t)\frac{dv(t)}{dt} + P_{res}(t) \tag{3.5}$$

Where the resistant power P_{res} is:

$$P_{res}(t) = F_{res}(t)v \tag{3.6}$$

$$P_{res}(t) = (\mu_r M_v g\cos\alpha + \frac{1}{2}\rho C_d A_f v^2 + M_v g\sin\alpha)v \tag{3.7}$$

And the acceleration $\frac{dv(t)}{dt}$ is computed with derivative method of backward difference:

$$a(t) = \frac{dv(t)}{dt} = \frac{v_t - v_{t-1}}{\Delta t} \tag{3.8}$$

When the EM is used in-wheel, its inertia is added to the wheels and tires inertia (I_{wh}). Considering the moment of inertia on the wheels during traction the power at wheels level become:

$$P_{wh}(t) = P_{trac}(t) + J_{wh}\cdot\dot{\omega_{wh}}\cdot\omega_{wh} \tag{3.9}$$

Where

$$\omega_{wh} = \frac{v_t}{r} \tag{3.10}$$

$$J_{wh} = \frac{1}{2}4(m_{wh} + m_{EM})r^2 \tag{3.11}$$

The vehicle data required for the implemented Matlab code calculations are as follows:

Parameters	Values	Unit
Wheel radius	0,15	m
Mass at full load	79	kg
Frontal area	0,48	$m\hat{}2$
Wheelbase	0,70	m
Track	0,55	m
Friction coeff. (μ_r)	0,01	
Drag coeff. (C_d)	1,05	
Slope (α)	8,53	°

Table 3.2: Preliminary design and dimensional parameters of the Robot

3.2 Powertrain design

3.2.1 Electric motor selection

The model on which the choice is oriented is the three-phase DC brushless motor. This type of permanent magnet electric motors offers numerous advantages, especially in the context of the required application. Electronic commutation provides greater efficiency over conventional DC motors with improvements of 20 to 30% for motors running at the same speed and load. Greater efficiency allows BLDC motors to be made smaller, lighter and quieter for a given power output [13].

Figure 3.5: Exploded view of an in-wheel brushless DC motor

Further, the BLDC motor is more durable,the precision control in turn reduces energy consumption and heat generation. It maintains its high performance while the efficiency and power of an equivalent conventional motor decreases due to wear from bad contact with the brush, the arc between the brushes and the switch that dissipates energy and creates dirt by compromising the electrical conductivity. Other advantages of BLDC motors include superior speed versus torque characteristics, a more dynamic response, noiseless operation, and higher speed ranges. The only downside of BLDC motors is their complexity and the associated increase in cost. Electronic commutation demands supervisory circuits to ensure precise timing of coil energization for accurate speed and torque control, as well as ensuring the motor runs at peak efficiency.

3.2.2 Electric motor sizing

From the calculations made in the previous paragraph, it is possible to obtain the maximum values of torque, power and angular speed required by the vehicle to travel the driving cycle. Being the electric motors distributed on each wheel the power will be divided by the number of driving wheels as well as the torque, while the angular speed required to the motors will be the same as that handled by the wheel. For the sizing of the electric motor it is assumed the use of the vehicle in four-wheel drive mode throughout the driving cycle, so all the engines work simultaneously providing the same percentage of torque required by the vehicle, but also takes into account the possibility of operating the vehicle with 2-wheel drive.

$$P_{Req,max} = \frac{P_{wh,max}}{4} \tag{3.12}$$

$$T_{Req,max} = \frac{P_{Req,max}}{\omega_{wh}} \tag{3.13}$$

$$\omega_{req,max} = \omega_{wh,max} \tag{3.14}$$

Required Parameters		
$P_{Req,max}$	182	W
$T_{Req,max}$	7,4	Nm
$\omega_{Req,max}$	55,5	Rad/s
$n_{Req,max}$	530	rpm

Table 3.3: Required Parameters

In order to evaluate power and torque that the electric motor must deliver is necessary to take into account its efficiency, so a vehicle modelling approach should be considered:

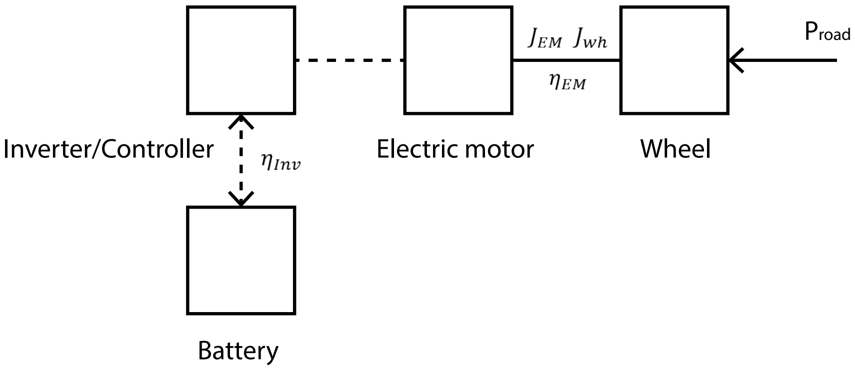

Figure 3.6: Schematic architecture of the powertrain

where η_{EM} is the efficiency of an electrical motor, η_{inv} is the efficiency of the inverter or the controller according to the type of electric motor (80 to 95%) and J_{wh} is the inertia of the wheels that in this case being the motors integrated in the wheel is equal to the inertia of the engine.

$$\begin{aligned} P_{EM,max} &= \frac{P_{req,max}}{\eta_{EM}} \\ T_{EM,max} &= \frac{T_{req,max}}{\eta_{EM}} \end{aligned} \tag{3.15}$$

For a correct sizing of the motor, the place of loads must be within its operating range. Taking into consideration the results of the Tab.3.3 we chose the brushless DC hub motor, model HJ-017. Being available in powers from 180-350 Watts and voltages from 24/36/48, a power of 250 Watts and a voltage of 36 Volt has been selected as at lower values the motor does not satisfy the required torque, while higher values involve a considerable weight of the battery pack which would excessively affect the overall mass of the vehicle. Below is reported the data sheet (Tab. 3.4) and the characteristic curves of the motor in question (Fig. 3.7).

Analysis of the Elettric vehicle model shows that the maximum torque the electrical motor can produce is the limiting factor to the permissible traction effort of the BEV. The torque curves of Fig. 3.7 initially are constant up to a certain speed, and then they hyperbolically decrease with the speed. Such dependencies are originated from the physical nature of the motor torque. The quantities restricted in a motor are first the current and then the torque and power. At low speeds, the current limitation is active, thus the torque is constrained to be constant. At higher speeds, the power limitation is active. This results in a constant output power while the torque declines hyperbolically with the speed.

Considering the speeds at which the drone is programmed for its field of application, the four engines will have to reach maximum speeds of 530 revolutions

MODEL: HJ-017		
Design	Gearless	
Voltage	36	*V*
Rated power	250	*W*
Peak Power	300	*W*
Peak Torque	11,6	*Nm*
Max Speed	650	*rpm*
Max Efficiency	84,5	*%*
Dimensions	220	*mm dia.*
Weight	3,3	*kg*

Table 3.4: Data-sheet of the HJ-017 Bldc motor

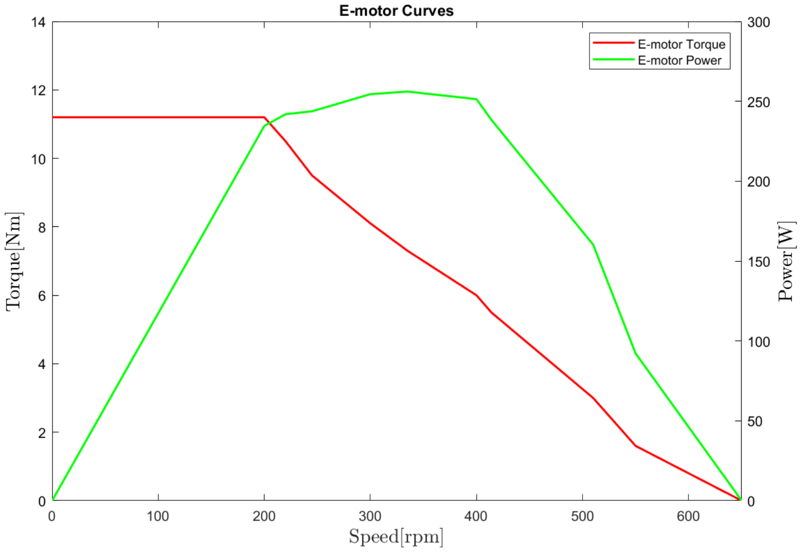

Figure 3.7: Characteristic curves of the HJ-017 Bldc motor

per minute. The electric motor analyzed meets this threshold, it is therefore not necessary to introduce a transmission between the engine and the wheel and this reduces the complexity of the system and its weight.

Through the datasheet of the electric motor available and the diagram of the cycle guide it is now possible to realize the motor map with the trend of the efficiencies and the distribution of the working points. Since the engine can also be used as a generator, the graph will be mirrored with respect to the x-axis, so as to analyze the negative torque curve useful for the management of energy and regenerative braking.

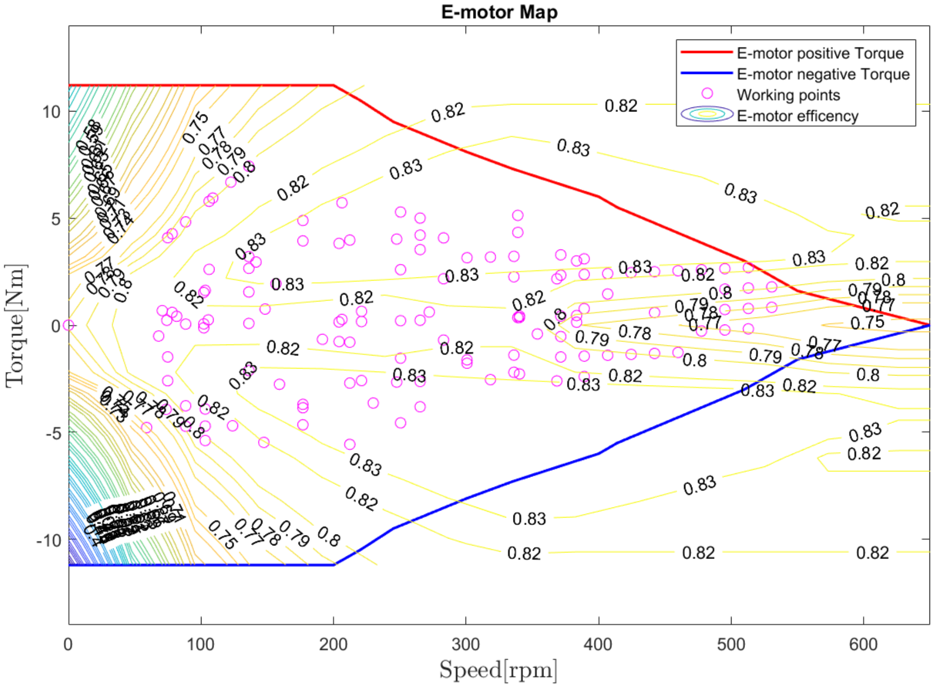

Figure 3.8: E-Motor/Generator map

For electric machines of this type is expected an efficiency map with maximum yield towards the center and minimum in the regions of high torque and low speed. In fact for high torque and low speed the efficiency reaches the minimum of its value, lower efficiencies are present even at high speeds and minimum torques.

3.2.3 Tests

From the analysis of the intersection points between the resistant curves of the vehicle and the characteristic curve of the engine, it is possible to note the effective maximum values of speed and torque that the drone can reach in three operating conditions examined:

- vehicle driving on a flat road in 4WD
- vehicle driving on a flat road in 2WD
- vehicle driving on a 15% inclined road in 4WD

As we can see from Fig. 3.9 In the case of 4-wheel drive on a flat road, the vehicle will reach a maximum speed of 32 km/h, while on a 15% gradient of 22

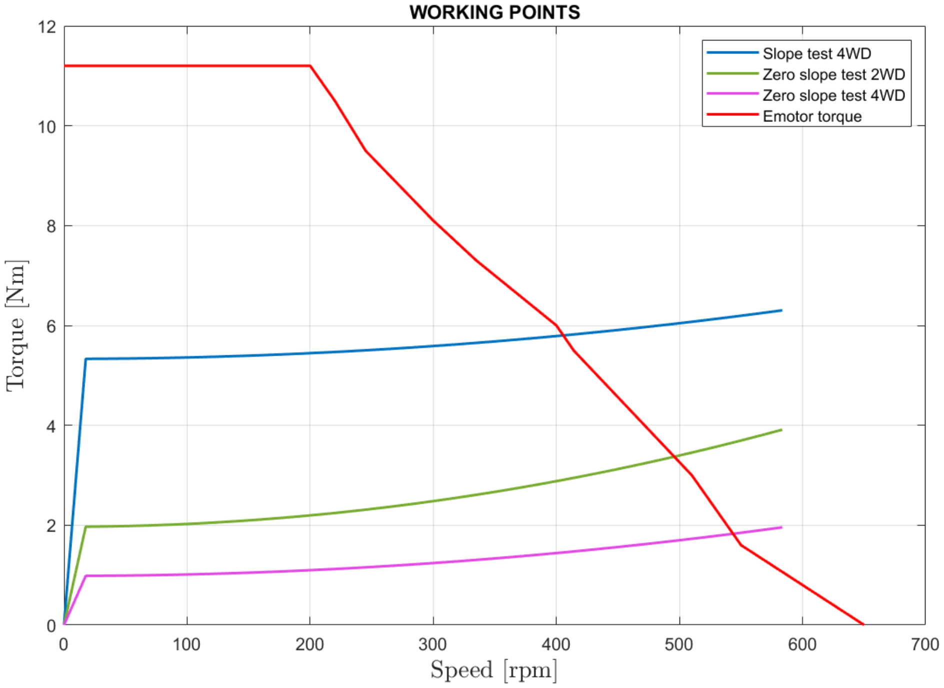

Figure 3.9: Resistant curves in three different operating conditions

km/h. If you choose to operate the vehicle in 2-wheel drive mode, it will travel at a speed of 27 km/h on a flat surface, while on sloping roads this mode is not allowed for too high torque values.

Working points				
	Torque		**Speed**	
Slope Test 4WD	5,8	*Nm*	405	*rpm*
Zero slope Test 2WD	3,4	*Nm*	495	*rpm*
Zero slope Test 4WD	1,8	*Nm*	543	*rpm*

Table 3.5: Tests results of three different operating conditions

In order to optimise the energy consumption of the vehicle on the instant-by-instant driving cycle, the efficiency of the engines has been calculated to satisfy the required power at ground level in both two-wheel drive and four-wheel drive modes, selecting the one that results in a lower required battery power. For the calculations, the formulas previously analysed are used.

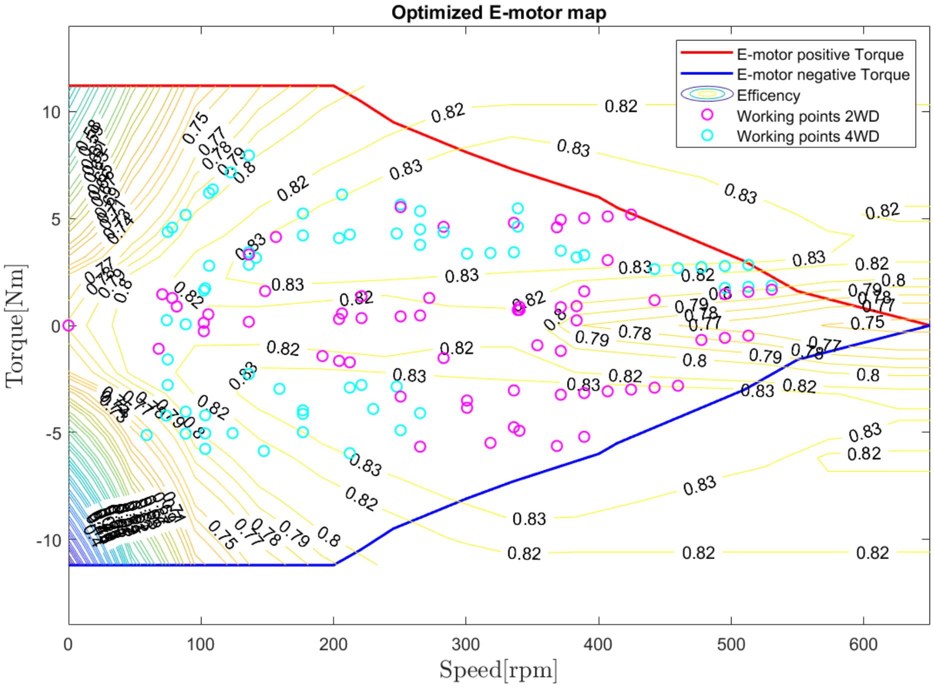

Figure 3.10: Optimized electric motor map and working points in two and four wheel drive mode

From the graph 3.11 you can see driving mode variation between two motors driven and four motors driven throughout the driving cycle.

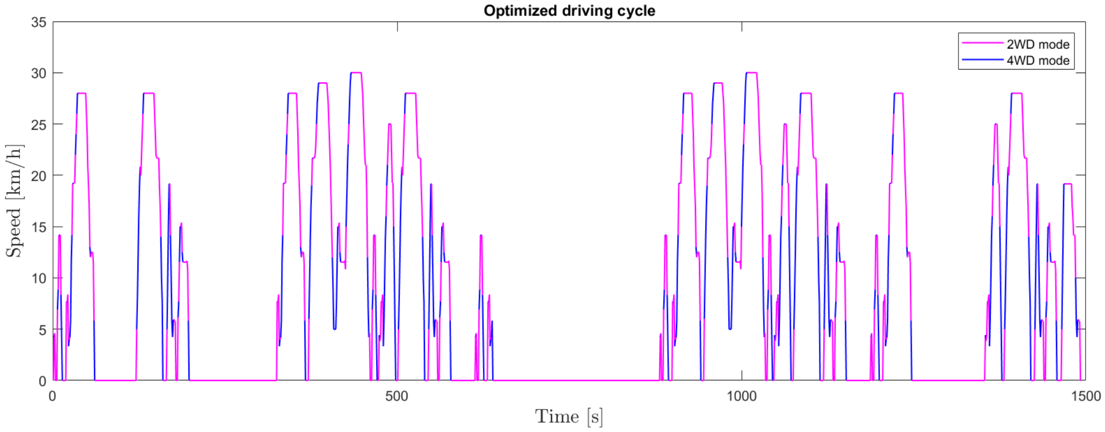

Figure 3.11: Optimized driving cycle in two and four wheel drive mode

3.2.4 Torque, speed and position control

To make a BLDC motor rotate, the stator windings must be energized according to a precise sequence, for this purpose it is essential to know the instants at which the currents must be switched, instants that depend on the position of the rotor. An electronic control unit is used for this purpose [14]. A FOC (Field Oriented Control) vector control unit was chosen, capable of overcoming the limitations of both trapezoidal and sinusoidal drives, providing smooth motion at low speeds and efficient operation even at high speeds; it also allows for higher positioning accuracies, power density and efficiency, and quiet operation.The operation of the controller is based on the management of the stator windings to maintain orthogonal the flux generated by the permanent magnets of the rotor with respect to the stator field. The main objective of the FOC control is in fact to maximize the torque of the motor and this is achieved when the flux vector of the stator is 90 degrees with respect to the flux vector of the rotor. With FOC, two PI current controllers can be used to separately control both components of the motor current vector. One current controller is used to control the torque of the motor and is therefore called the torque controller, the other controls the magnetic flux inside the motor, mainly generated by the rotor.

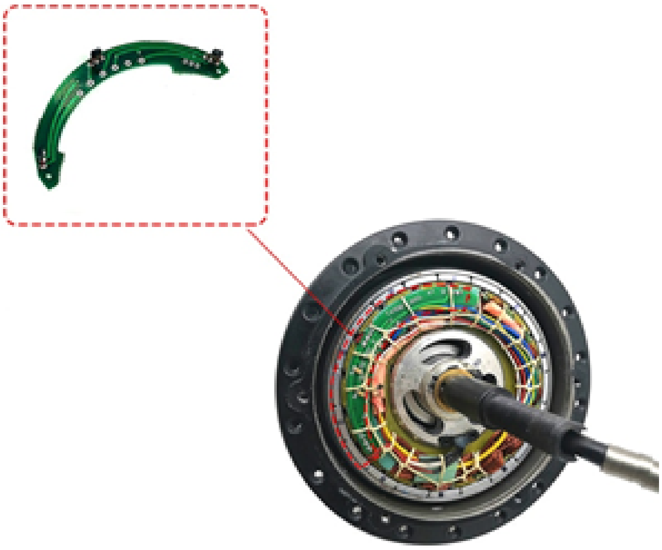

Figure 3.12: 250 Watt motor hall sensor

The estimation of the angular position can be carried out using magnetic transducers that exploit the Hall effect as they are able to detect the presence and intensity of a magnetic field.The decoding logic integrated in the device is a combinatorial logic that provides the appropriate driving signals for the outputs of the three-phase bridge, based on the signals coming from the three hall sensors. The Hall effect sensor is mounted on the rear of the motor, as shown in the Fig. 3.12

For the HJ-017 250 W motor analyzed in this thesis, we choose between FOC control products specially designed for brushless DC motors from 180 W to 1 kW with voltages between 24V and 96V.

Figure 3.13: FOC control device

Controller 250W Bldc Motor		
Type	CZD002S	
Motor Phase Angle	120	°
Rated Voltage	36	V
Rated Current	17 +1	A
Max Current	34+1	A
Dimension	150x88x45	mm
Weight	0,6	kg

Table 3.6: Controller data-sheet

3.3 Overcoming obstacles

The analysis of the possibility of overcoming an obstacle or a ramp is developed as the drone will often face the architectural barriers of the city to deliver the parcels exactly where the customer is located. The typical contact force changes while a wheeled robot is climbing an obstacle, which results in the development of an extra component of motion resistance at the tire/obstacle interface. In reality, the robot's posture varies as a result of climbing obstacles, and this has an impact on how much weight is distributed over the wheels, but this is negligible. A manageable configuration equation of obstacle resistance can be derived from the equations of static equilibrium of a wheel robot climbing a discrete obstacle on a hard surface or compacted soil. Consider for instance the case of the robot with rigid suspension climbing a square obstacle in four-wheel drive mode, so by considering the maximum torque that the electric motors can provide.

As we can see from Fig 3.14 the torque T coming from the motor of the front wheel (the one near the obstacles) will generate a traction force R and a normal force N in the contact point P. At the same time the motor of the rear wheel generate a torque corresponding to a force acting on the center of the front wheels F. To find out the value of these forces, we'll write the equilibrium equations for the forces acting in point P.

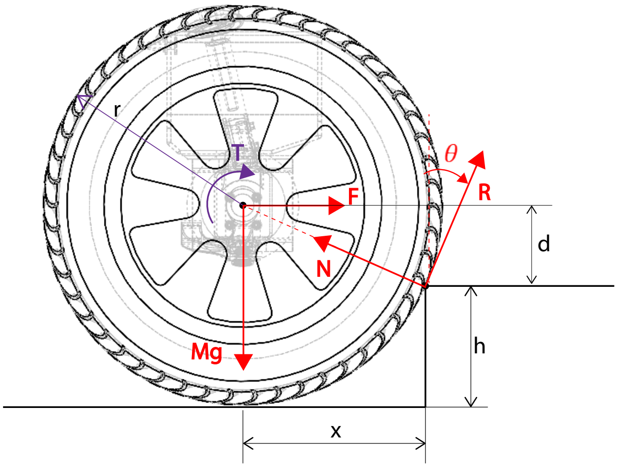

Figure 3.14: Overtaking the step during traction in four-wheel drive mode

$$\begin{cases} R_x - N_x + F = 0 \\ R_y + N_y - Mg = 0 \\ F \cdot d - Mg \cdot x = 0 \end{cases} \tag{3.16}$$

$$\begin{cases} F = \dfrac{\dfrac{mg}{4} \cdot x}{d} \\ R = \dfrac{\dfrac{mg}{4} - F \cdot \tan\theta}{\cos\theta + \sin\theta \tan\theta} \end{cases} \tag{3.17}$$

Where:

$$\begin{aligned} d &= r - h_{max} \\ x &= \sqrt{r^2 - (r - h_{max})^2} \end{aligned} \tag{3.18}$$

From the calculations made, we obtain a maximum step height that can be exceeded by the drone, of 70 mm in the case in which the four electric motors simultaneously emit their maximum torque of 12 Nm.

Another important study to be carried out is the crossing of a ramp without the edge of this touches on the base platform of the robot. According to the vehicle's ground clearance and its wheelbase, the maximum angle of a ramp that can be overcome corresponds to the breakover angle. Breakover angle can be defined as follow:

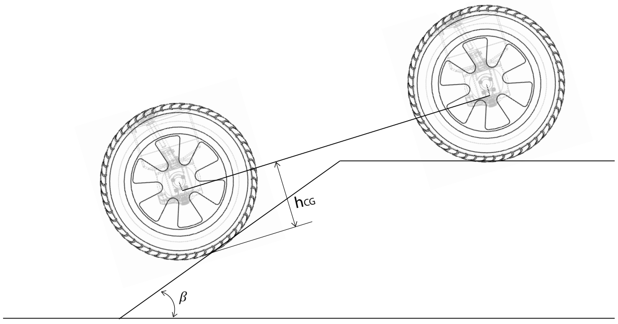

Figure 3.15: Admissible angle to overcoming ramps

$$\beta = 2 \cdot \arctan\left(\frac{h_{GC}}{\frac{Wb}{2}}\right) \tag{3.19}$$

Considering that the height from the ground of the Robot is set to 120 mm, the max Breakover angle can be of about 36 degree.

Ground clearance	120	mm
Max step height	70	mm
Breakover angle	36	^{o}

Table 3.7: Maximum hei angle to overcoming ramps

For the reasons mentioned in the first part of the section the robot is designed with a height above the ground that allows specific movements such as getting on the sidewalks, on the platforms of bus stops or entering the compartment of the bus dedicated to him.

Chapter 4

Energy management

In this section, the demand for instant-to-instant energy of the vehicle is analysed according to the desired performance. Following the trend of the driving cycle, therefore, the sizing of the battery pack is developed by finding a compromise between weight achieved and desired autonomy to perform the highest possible number of deliveries.

Power and energy demands depend on the performance and range to achieve with the vehicle. These system characteristics can be obtained by analytical calculations, data acquisition from a similar product, or via models; in this application is used the first one since this is a field still under development.

In the study of energy demand is also taken into account the regenerative braking that as we will see contributes significantly to the prolongation of the battery discharge. Once evaluated the possibility of producing the required power in traction or regenerative the available power during braking phases, the battery SOC variation can be analysed.

4.1 Battery selection

In the design of the battery pack it is essential to identify the right compromise so that the chosen cell can meet the energy and power requirements foreseen by the project; usually the cells that have high specific power are not very energetic and vice versa. In order to compare cells of different types, it is useful to analyze the Ragone diagram, which has the specific power as its abscissa and the specific energy as ordered. Through the study of different materials and energy storage technologies, in the Ragone diagram it is possible to observe the behavior of the cells in the charging or discharging phase as a function of the specific power. The optimal performance of the cell is identified by the knee of the curve, normally for a certain type of cells, once a certain specific power value is exceeded, there is a specific energy collapse.

Lithium-ion (Li-ion) batteries are the main technology currently used for most consumer electronic and EV applications. Their success has largely been spurred by their high specific energy and power ratings as shown in Fig. 4.1

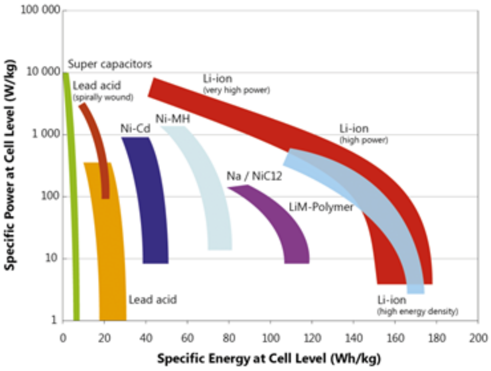

Figure 4.1: A Ragone chart depicting the range of specific energy and power levels achievable by current generation battery cell technology.

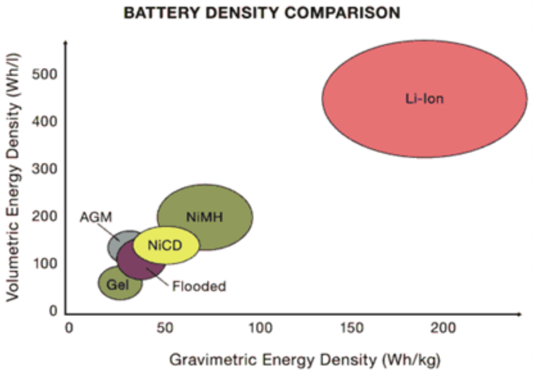

Figure 4.2: Comparison of energy densities of different battery systems.

For the application examined, are then chosen the type of lithium polymer battery for the reasons explained above, but especially because they can combine the ability to withstand high currents with its extreme lightness.

4.2 Battery sizing

4.2.1 Technical requirements and design target

Designing a battery pack begins by a good understanding of the vehicle it is meant to power. Thus, this section will introduce necessary cell characteristics need to calculate pack level specifications [15] and [16].
For EVs, the minimum power requirement of the battery pack is the maximum power needed by the electric propulsion system, i.e. the mechanical power at the wheel, plus all the losses. The estimation of the electric power can be realized based upon the operating map of the electric machine, considering also the regeneration of energy.

Three different conditions could be exploited in the electric powertrain:

1. One EM is used as motor during traction phases and another EM is used as generator during braking phases;

2. One motor/generator (MG) is used to manage both traction and braking phases;
3. A mixed version of point 1. and 2. (e.g. one MG and one EM).

The second condition has been adopted in this application. As mentioned in the previous chapter, the motor map (Fig. 3.8) is mirrored symmetrically with respect to the speed x-axis to also represent the operating conditions as a generator.

Assuming to ignore the overheating phenomena the trasformation of mechanical power to electric power relies only upon the EM efficiency point:

$$P_{EM,el} = \frac{P_{EM,mech}}{\eta_{EM}} \tag{4.1}$$

Where η_{EM} (< 1) is the EM efficiency as a function of EM torque and speed. During traction phases the electric side of the EM is responsible of producing the mechanical power required to move the axles plus the EM losses.

Therefore:

$$P_{EM,el} > P_{EM,mech} \quad \textit{during traction} \tag{4.2}$$

As far as a MG is considered from now onwards, a MG acts as a generator only during braking phases (P_{req}<0); in those cases:

$$P_{MG,el} = P_{MG,mech} \cdot \eta_{MG} \tag{4.3}$$

During braking phases, the electric side of the MG has not the possibility of receiving the entire mechanical power due to the MG losses.

Therefore:

$$P_{MG,el} < P_{MG,mech} \quad \textit{during braking} \tag{4.4}$$

The mechanical-to-electric (and viceversa) transformation for a MG can hence be resumed through the following equation:

$$P_{MG,el} = P_{MG,mech} \cdot \eta_{MG}^{k} \tag{4.5}$$

$$\textit{with} \begin{cases} k = 1 & \textit{braking phase} \\ k = -1 & \textit{traction phase} \end{cases}$$

The electric power required by the MG is provided by the energy storage system, but since the used MG is a Bldc motor, a controller is placed between the MG and the energy storage system.

In the power and energy analysis the controller can be modeled as an additional efficiency to be paid both in traction and braking phases. Its value, for the adopted device (Fig. 3.13) is 0,85.

$$P_{inv} = P_{MG,el} \cdot \eta_{inv}^{k} \tag{4.6}$$

$$with \begin{cases} k = 1 & braking\ phase \\ k = -1 & traction\ phase \end{cases}$$

The power required by the controller is the real power to be produced by the energy storage system in order to traction the vehicle during traction phases or recharge the system during braking phases.

$$P_{batt,el} = P_{inv} \tag{4.7}$$

The process is iterative as the required power will be dependent on the mass of the battery used.

$$M_{veh} = m_{curb\ weight} + m_{max\ load} + m_{batt} \tag{4.8}$$

We start the analysis assuming a battery mass of 10 kilograms and as if the vehicle is always fully loaded as it could recover parcels of returns during the delivery path.

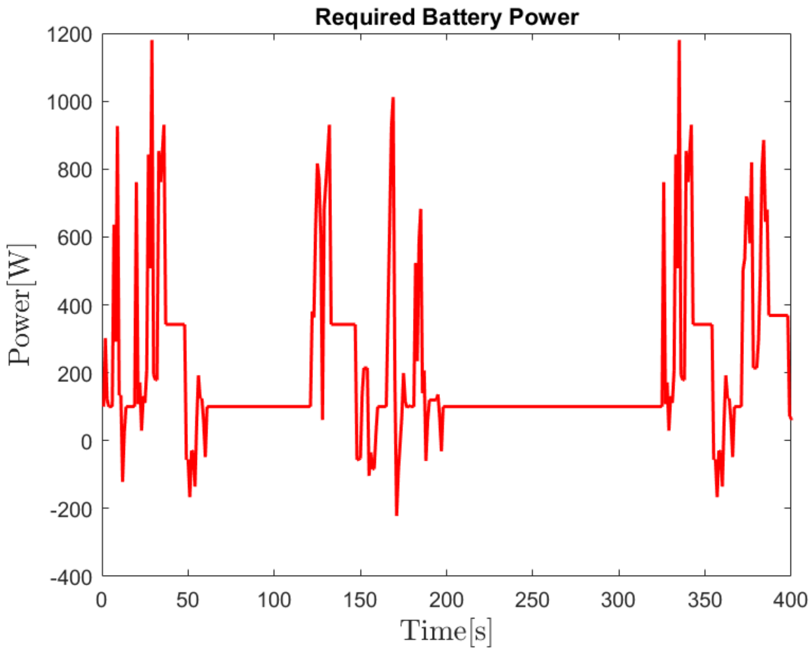

Figure 4.3: Required battery power variation during driving cycle up to 400 seconds

As we can see from the graph 4.3 the maximum instantaneous power required to the battery is about 1200 Watts, therefore since the four hub motors are connected in parallel with the energy source, battery needs a voltage of 36 Volts and must be able to supply a current of at least 35 Amperes during discharge.

$$P_{batt,req,max} = V_{batt} \cdot I_{batt,max} \tag{4.9}$$

In Fig. 4.3 is evident as even when the speed of the driving cycle is zero the vehicle consumes a power of 100 watts. This assumed power is required by all accessories such as the control unit, lights, displays, cameras and position and control sensors. Below is reported the Tab. 4.1 that summarizes the first parameters required for the sizing of the battery pack. In the next subsection will be dealt with in more detail.

BATTERY PACK TARGET SPECIFICATIONS			
Target	**Variable**	**Value**	**Units**
Maximum power	P$_{batt,req}$	$\geq$ 1,2	kW
Maximum current	I$_{batt,req}$	$\geq$ 35	A
Voltage	V$_{batt,req}$	36	V
Energy	E$_{batt,req}$	$\geq$ 120	Wh
Maximum width	y$_{batt,req}$	170	mm
Depth of discharge	DOD	80	$\%$

Table 4.1: Battery Target specifications

The discharge power $P_{batt,nom}$ needs to be greater to the maximum power demand of the vehicle $P_{batt,req}$. To avoid limiting the vehicle's power during normal operation, the battery's available power should remain higher than $P_{batt,req}$ even at low SOC. For this reason will be chosen a battery that will have a C rate that, after deciding the capacity of the battery according to the autonomy you want to obtain, will be able to withstand the passage of currents greater than 35 amps (Eq. 4.15). The capacity of the battery together with the number of cells in series and in parallel and the appropriate C-rate are defined in the next subsections.

4.2.2 Cell parameters

Cylindrical Lithium-ion cells were selected as the most suited for the application, because of their high capacity and low internal resistance.Although the theoretical energy density of cylindrical cells may appear to be smaller than those of prismatic cells, 18650 are a very good choice to maximize pack density in tight volumes or weirdly shaped spaces.The capacity of a single cell of 4.8 Ah has been decided according to how much autonomy you want to assign to the drone, which we see in the next paragraph. Like all other 18650 format cells,their operational voltage ranges from 2.5 V at $SOC = 0\%$ to 4.2 V at $SOC = 100\%$. However, in order to operate the cells safely and at in their best operational range, a lower voltage threshold value of 3.48 V is fixed, limiting discharge 20% SOC. Cell specifications are presented in Tab. 4.2

CELL SPECIFICATIONS

Parameter	**Variable**	**Value**	**Units**
Diameter	D_{cell}	14	mm
Lenght	I_{cell}	107	mm
Weight	m_{cell}	130	g
Maximum voltage	$V_{cell,max}$	4,2	V
Nominal voltage	$V_{cell,nom}$	3,7	V
Lower voltage limit	$V_{cell,SOC=20\%}$	3,48	V
Minimum voltage	$V_{cell,min}$	2,5	V
Nominal capacity	$Q_{cell,nom}$	4,8	Ah
Internal resistance	R_{cell}	150	$m\Omega$
Maximum power	P_{cell}	28,7	W

Table 4.2: Cell specifications

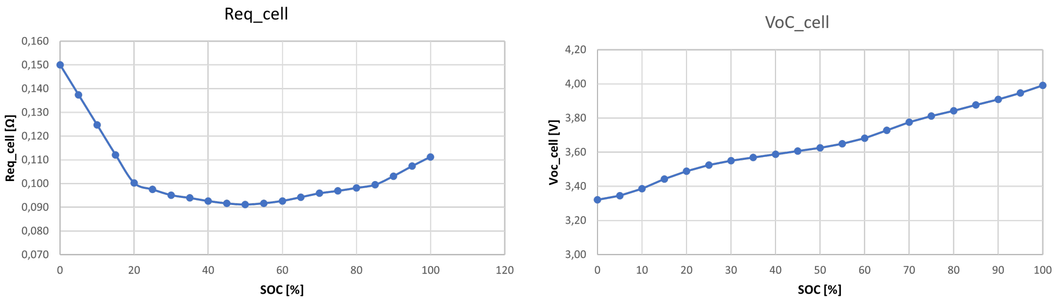

(a) *Cell internal resistance*

(b) *Cell open circuit voltage*

Figure 4.4: Cell characteristic curves

Internal resistance and open circuit voltage curves characteristic of the cells are necessary for the study of the variation in the state of charge of the battery pack.

4.2.3 Battery parameters

The number of cell in series is fixed to 10 cells since the voltage limits of the energy storage system is defined by technical considerations such as the operating voltage of the motor and the power electronics, so:

$$V_{batt,nom} = N_s V_{cell,nom} \tag{4.10}$$

$$N_s = \frac{V_{batt,nom}}{V_{cell,nom}} \tag{4.11}$$

The number of cells in parallel of the battery, which is equal to 5 cells, is defined by the relationship 4.13

$$P_{batt} = N_s N_p P_{cell} \tag{4.12}$$

$$N_p = \frac{P_{batt}}{N_s P_{cell}} \tag{4.13}$$

Now the total capacity of the battery can be calculated:

$$Q_{batt} = N_p Q_{cell,nom} \tag{4.14}$$

To ensure that the battery is able to withstand the passage of maximum discharge current, we calculate the necessary C-rate:

$$C_{dis} = \frac{I_{dis,max}}{Q_{batt}} \tag{4.15}$$

The energy contained within the battery pack E_{batt} is defined as the sum of the energy stored in each cell, assuming identical cell energy E_{cell} for all cells in the pack:

$$E_{batt} = N_s N_p Q_{cell} V_{cell,nom} \tag{4.16}$$

However, the usable energy $E_{batt,us}$ of a battery depends on the DOD, the allowable depth of discharge which is set to 80%:

$$E_{batt,us} = E_{batt} DOD \tag{4.17}$$

It is obtained a usable energy of about 800 Wh which is significantly higher than that required by the vehicle, obtained integrating the area defined by the curve of power on the driving cycle, which is about 120 Wh.

$$E_{batt,req} = \int_{t1}^{t2} P_{batt,req} \cdot dt \tag{4.18}$$

One of the most constraining aspect of the design is the battery volume, a characteristic that needs to be minimized because of the limited space available within the Robot. System integration is an empirical trade-off process that needs to consider all aspects at once. The battery pack maximum volume Vol_{batt} of the Drone was constrained by the wheel base, the width of the guides on which the piston slides and allows the automatic release of the pack , maximum height between the two vehicle platforms, one lower for the battery holder and all other electrical components and the other upper for the support of the packages to be shipped, for a total available of 0.08 m^2. Assuming the cells are uniformly distributed within the pack, one can estimate the volume of each arrangement. The fill ratio f_r for an orthogonal cell layout configuration is equal to $\frac{4}{\pi}$. Figure 4.5 shows the dimensions used to estimate pack volume such as cell diameter D_{cell}, cell length l_{cell} and the gap distance between cells d_{gap} are the main variables needed to estimate Vol_{batt} (4.19). Note that considerations for the volume of the auxiliary systems, such as the BMS and conductors, should always be taken into account for the final design.

$$Vol_{batt} = N_s N_p l_{cell} f_r \frac{\pi(D_{cell} + d_{gap})^2}{4} \tag{4.19}$$

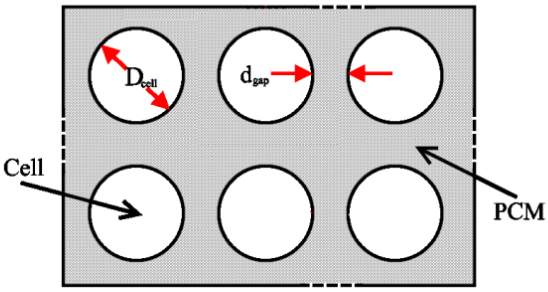

Figure 4.5: Cell layout in the pack

Battery weight is calculated with (4.20), as the sum of the weight of the cells m_{cell} and weight of the phase change thermal management material m_{pcm}.

$$m_{batt} = N_s N_p (m_{cell} + m_{pcm}) \tag{4.20}$$

BATTERY PACK SPECIFICATIONS			
Parameter	**Variable**	**Value**	**Units**
Number in series	N_s	10	
Number in parallel	N_p	5	
Total number of cells	N_t	50	
Nominal voltage	V_{batt}	36	V
Capacity	Q_{batt}	24	Ah
Rated discharge current	I_{dis}	35	A
Istantaneous maximum discharge current	$I_{max,dis}$	75	A
C-rate charge	$C_{max,ch}$	0,35	
C-rate discharge	$C_{max,dis}$	3	
Contained energy	E_{batt}	864	W
Usable energy	$E_{batt,us}$	690	W
Power	P_{batt}	1260	W
Volume	Vol_{batt}	210x107x70	mm
Weight	m_{batt}	6,5	kg
BMS additional weight factor	BMS	1,5	

Table 4.3: Battery pack specifications

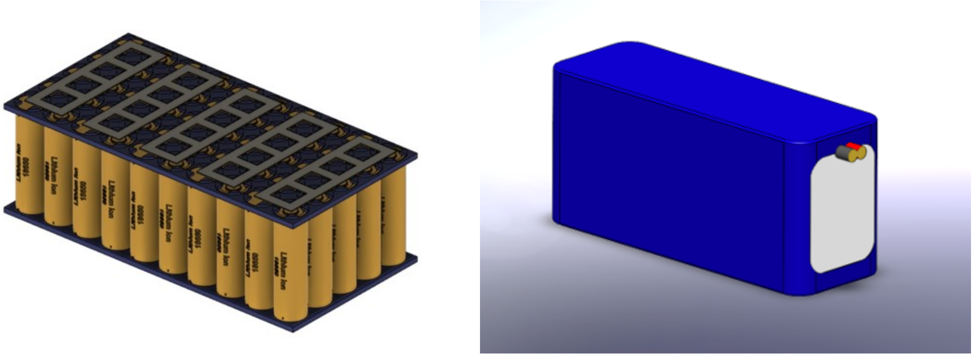

(a) *Cells configuration* **(b)** *Final assembly*

Figure 4.6: Battery pack size and layaut

4.3 Performance calculations

4.3.1 Battery operating power

It is important to understand how the ability to produce energy of the battery changes with its state of charge in order to evaluate its effective duration and therefore the maximum distance that the drone will reach [17]. ICE and MG show the capability of providing the power required to traction or brake the vehicle according to the maximum (and minimum) limit curves torques vs speed. For batteries a similar procedure has to be taken into account but only with electric links.

- The power limit curve of the battery during traction is evaluated as:

$$P^{tr}_{batt,max}(SOC) = min(P^{tr}_{batt,max,el}(SOC), P^{tr}_{batt,max,chem}(SOC)) \tag{4.21}$$

Where:

$$P^{tr}_{batt,max,el}(SOC) = \frac{V^2_{oc}(SOC)}{4 \cdot R_{eq}(SOC)} \tag{4.22}$$

$$P^{tr}_{batt,max,chem}(SOC) = V_{oc}(SOC) \cdot I_{max,dis} - R_{eq}(SOC) \cdot I^2_{max,dis} \tag{4.23}$$

According to the Rint model, the maximum power achieved by the battery is linked to both electric and chemical phenomena. Specifically the open circuit voltage $V_{oc}[V]$ and the equivalent internal resistance $R_{eq}[\Omega]$ of the battery have to be evaluated at each battery state of charge level.

$$R_{eq}(SOC) = R_{eq,cell}(SOC) \cdot \frac{N_{sm} \cdot N_s}{N_p} \tag{4.24}$$

$$V_{oc}(SOC) = V_{oc,cell}(SOC) \cdot N_{sm} \cdot N_s \tag{4.25}$$

With N_{sm} number of modules, which in this case is equal to 1.

The open circuit voltage typically increases together with the SOC whereas the equivalent internal resistance has minimum within a specific SOC window as we can see in Figure 4.7.

R_{eq} can be considered equal during both charge and discharge conditions.

About the maximum current admitted in the battery during discharging mode, the following equation has to be taken into account:

$$I_{max,dis} = \frac{C_{batt}}{1h} \cdot C_{max,dis} \tag{4.26}$$

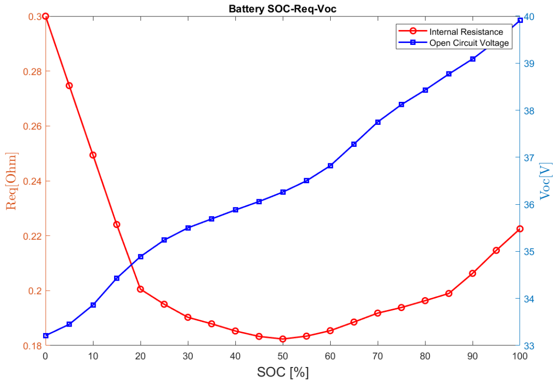

Figure 4.7: Variation of the internal resistance and the open circuit voltage of the battery depending on its state of charge

Where

$$C_{max,dis} = maximum\ C - rate\ during\ battery\ discharging\ phases$$

- The power limit curve of the battery during braking phases is evaluated as:

$$P^{br}_{batt,max}(SOC) = -(V_{oc}(SOC) \cdot I_{max,ch} + R_{eq}(SOC) \cdot I^2_{max,ch} \tag{4.27}$$

Where

$$I_{max,ch} = \frac{C_{batt}}{1h} \cdot C_{max,ch} \tag{4.28}$$

$$C_{max,ch} = maximum\ C - rate\ during\ battery\ charging\ phases$$

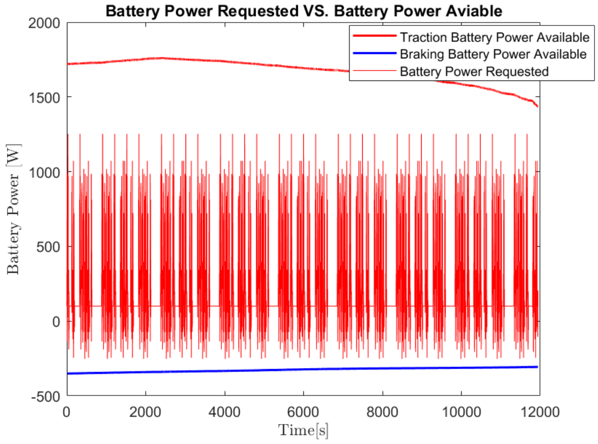

Figure 4.8: Battery Power Requested VS. Battery Power Available

As we can see from figure 4.8 interpolating the obtained values in both traction and braking phase the chosen battery always meets the requirements. The power requested by the vehicle is lower than the battery limit curves throughout the vehicle's range which corresponds to 8 driving cycles.

4.3.2 Battery State of Charge

Once evaluated the possibility of producing the required power in traction or regenerating the available power during braking phases the battery SOC variation can be computed. At time t:

$$SOC_t = SOC_{t-1} - \int \frac{I_{batt}}{C_{batt}} \cdot dt \tag{4.29}$$

Where

$$I_{batt} = \frac{V_{oc}(SOC) - \sqrt{V_{oc}^2(SOC) - 4 \cdot R_{eq}(SOC) \cdot P_{batt}}}{2 \cdot R_{eq}(SOC)} \tag{4.30}$$

The effects of regenerative braking can be seen from the SOC variation graph Fig. 4.9. The battery discharges 9,5% during the first driving cycle, this allows the vehicle to go through 8 driving cycles of 1493 seconds before completely discharging. Battery discharge should never drop below 20% to increase battery life.

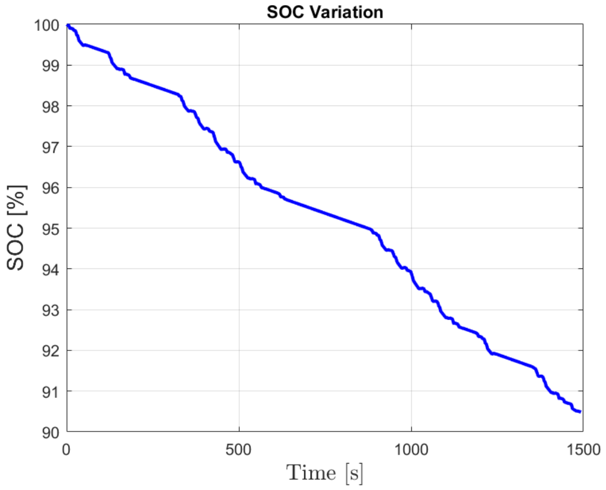

Figure 4.9: Variation of the battery state of charge during the first driving cycle.

As you can see from the graph Fig. 4.10 of the variation of the state of charge superimposed on the driving cycle of the drone, it is clearly evident that in the acceleration phases the battery will suffer a decrease of the SOC, which is significantly more impactful than the regeneration phase during braking.This is due to the fact that C-rates of charge and discharge have an order of magnitude of difference. When the drone is at zero speed, the battery discharged anyway because 100 Watts of constant consumption are considered for the operation of the accessories and the control unit.

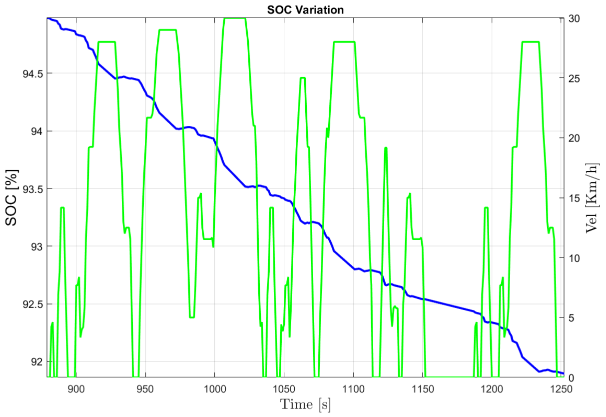

Figure 4.10: Enlargement of the state of charge variation superimposed on the driving cycle

Vehicle Performance		
Parameter	**Value**	**Units**
Driving range	30	*km*
Number of cycles	8	
Discharge I° cycle	9,5	*%*
Energy	120	*Wh*
Discharge limit	20	*%*
Fast charge	2-3	*h*
Normal charge	5-6	*h*
Number of missions	4	
Parcels delivered	24	

Table 4.4: Vehicle driving performance with reference battery pack

Thanks to the adopted energy supply system, the drone will be able to travel about 30 kilometers before completely discharging. This means that Pacci can accomplish within an operational mission, which includes the exit from the warehouse, deliveries, return to the warehouse, about 8 driving cycles and therefore 4 different neighborhoods within a kilometer radius. In a charging cycle a robot will have delivered about 24 packages. At this point you can return to stock, recharge the packages in the compartment, recharge the battery with a charging time from 5-6 hours in standard mode or 2-3 hours in fast mode and start a new mission.

Chapter 5

Suspension system

The purpose of this chapter is to define a suspension geometry that allows the drone to travel safely, avoiding overturning situations and allowing the overcoming of obstacles and the travel of uneven roads. The suspension is designed to provide a stable platform to keep the wheel treads on tract, to insulate the robot from the surface irregularities and to take part of good handling properties. Pacci will often find himself walking along streets with cobblestones and going down and up from the sidewalks, to avoid the damage of the packages it carries you need a suspension system. At the initial step, the stiffness and the damping constants are determined based on the quarter car model with 2 degree of freedom, then the absolute accelerations respect to the relative displacement of the suspension where analysed. The simulation of the dynamic response of the vehicle's body is conducted on the platform of Simulink-MATLAB and the interactions amongst the components within the system are observed in frequency domain to evaluate the effectiveness of the suspension.

5.1 Design preliminary outline

5.1.1 Suspension scheme

The greatest design constraint for the suspension system is the available space and the presence of the four servo motors for the independent steering of the 4-wheel drive, which we will discuss in chapter 6. The suspension can not be connected directly to the center of the wheel but it is necessary to add a small axis connected to a C-bracket on which rests the servo motor. Through a second bracket the shock absorber and the lower arm are positioned according to the calculated inclinations and both connected to the body of the vehicle.

As we can see from figure 5.1 the system used is a McPherson suspension because

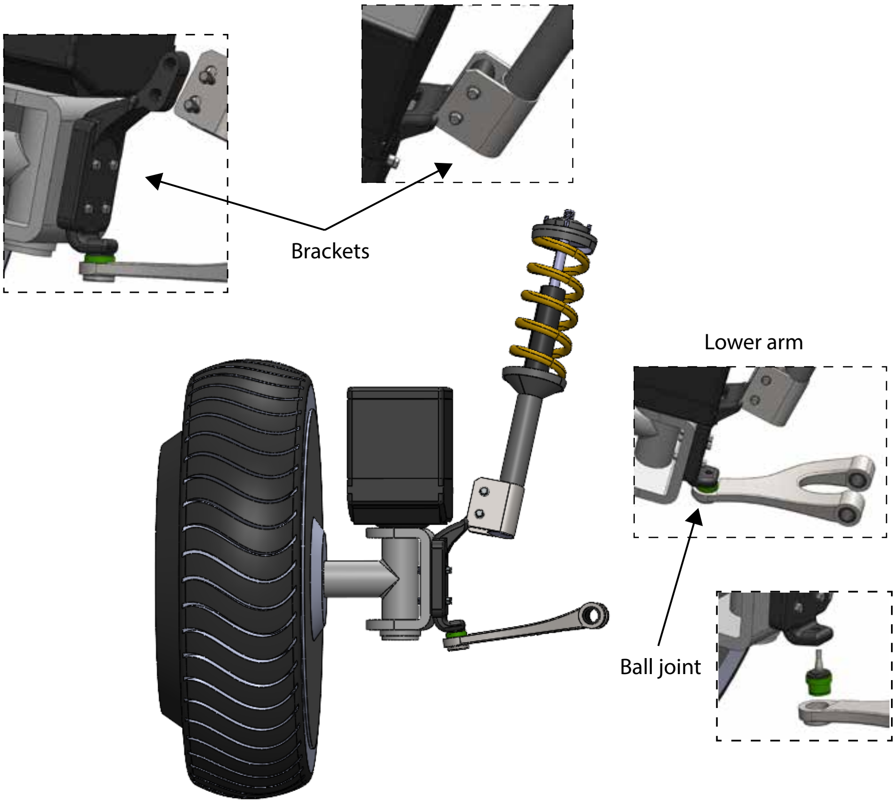

Figure 5.1: 3D Cad of suspension system components

for its geometric construction it is applicable to this type of small size vehicles. Consisting of a cylindrical helical spring mounted coaxially on a shock absorber with a structural function, the McPherson suspension scheme is one of the simplest geometries. The upper part of the unit is tied to the anchoring point of the body while the lower part is linked to a single lower arm, a pseudo-triangular shape which forms the joint in the lower area. The lower arm is connected to the body and it is also linked to the strut through a spherical joint. At the base of the shock absorber two welded brackets are used to fix the strut in a rigid way; the spring is contained between two seats, one connected to the shock absorber, the other to the thrust bearing; the upper ring of this bearing rests on the elastic element, fixed to the body.

This typology of suspension was chosen for the following reasons:

- Design simplicity and reduced cost.
- Wheels of the same axis are not rigidly connected by a transverse element.
- Because of the relevant separation of body joints, forces exerted on the body

are low in comparison, for example, to a low double wishbone suspension.

- Higher suspension stroke than in other suspensions (a high double wishbone one for example, because of the limitation on upper arm length).
- Contained transversal dimension, due to the absence of the upper arm.
- Does not reduce the height from the ground and is lighter than a crossbow suspension.

5.1.2 Geometry definition

The choice of suspension scheme has been made previously, taking into account the volumes of the mechanical components of the chassis, the minimum clearance from the ground, the body structure and the other conditions determined by costs and available production technology.

The preliminary design of a suspension scheme consists essentially of the determination of the geometric coordinates of the articulation points and of the position of the main axes. In this paragraph a step by step logic flow of the design outline operations is explained.

The first step consists of the identification of the king-pin axis position.The king-pin axis is determined by the center of the spherical joint A and the center of the upper pivot B (Fig. 5.2). To reduce as much as possible the reaction to lateral forces on the lower arm, the point A is set as low as possible. The point B position must allow the assigned suspension stroke, the elevation of point B must be as low as possible to comply with a low profile.

The position of point C, setting the rotation axis of the lower arm, is a consequence of the desired camber recovery and track variation.

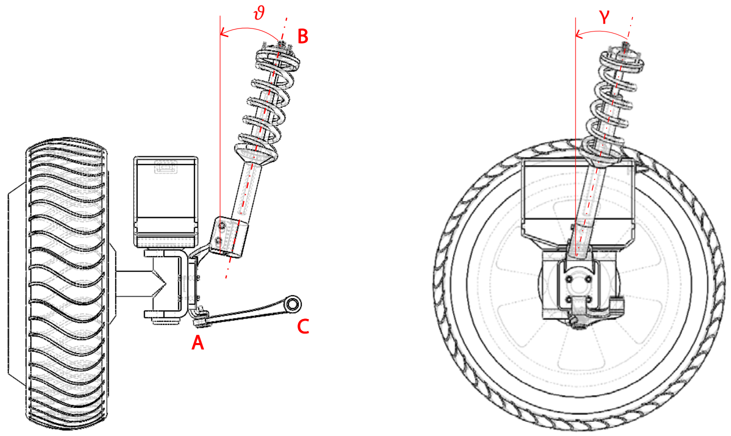

Figure 5.2: Geometric scheme and articulation points of a McPherson suspension

All these parameters are defined in such a way that the resulting position of the instantaneous rotation centers and conseguently of the roll and pitch centers, increases the stability of the vehicle, especially in situations of steering, braking or acceleration.

The instant center is the pivot point found through the intersection of the axis passing through the upper and lower linkages, Fig. 1.4.The first axis is perpendicular to the tilt of the shock absorber the second follows the extension of the lower arm; as the position of the linkages changes during the wheel bump the position of the center changes too. Considering the three dimensions, connecting the two points in front and side view the instant axis is obtained about which the suspension rotates.

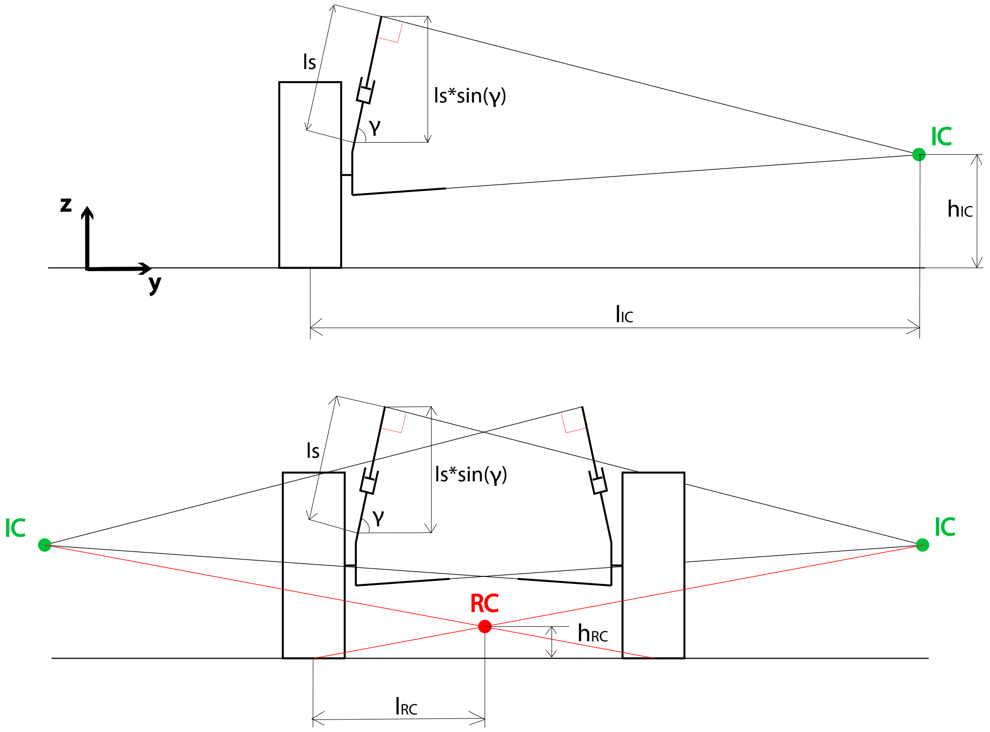

Figure 5.3: Geometric scheme and articulation points of a McPherson suspension

The aim is to determine a position of the roll center, obtained with the intersection of the two axes between the istant center and the contact patch, which is as suitable as possible for the application under consideration.

The roll center is infact the point where lateral forces are exchanged between unsprung and sprung masses: the lower the RC, the more the rolling moment increases. Furthermore, the more the height of the RC increases, the more the so-called jacking force increases, i.e. the forces that push the body upwards and cause significant variations in the drone's set-up. Finally, it is important to keep the RC height as low as possible to reduce load transfers.

Similarly to the roll center, the pitch center is determined in a lateral view.

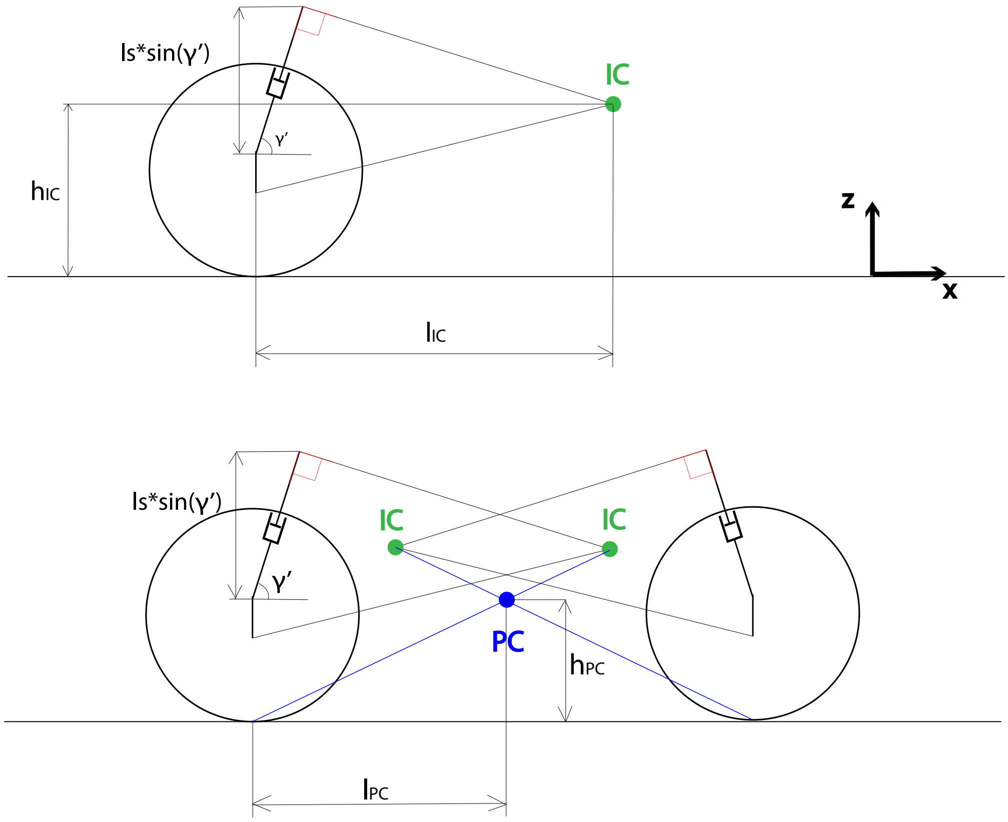

Figure 5.4: Determination of Pitch center position (blue dot)

We can therefore summarize in these tables the most relevant parameters found:

Suspension parameters and rotation centers							
	Value	Units		**X**	**Y**	**Z**	
Lower arm	152	*mm*	Instant center (x-y)	0	982	183	*mm*
Suspension length	230	*mm*	Instant center (z-x)	503	0	240	*mm*
King pin angle (γ')	13	°	Roll center	0	250	51	*mm*
Caster angle (γ)	15	°	Pitch center	350	0	173	*mm*

Table 5.1: Suspension geometry parameters

5.1.3 Stiffness evaluation

The vehicle model considered in this study is a quarter car model with two degrees of freedom. It consists of one-fourth of the body vehicle,including a single wheel with related suspension and the part of the body whose weight is imposed on it [18]. The assumptions of this quarter car model are as follows:

- The tire is modeled as a linear spring without damping;
- There is no rotational motion in wheel and body;
- The behavior of spring and damper are linear;
- Tire is always in contact with the road surface;
- Effect of friction is neglected so that the residual structural damping is not considered into vehicle modeling;

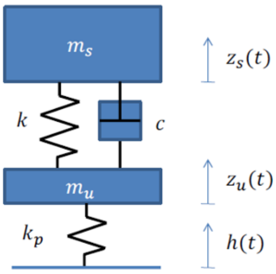

Figure 5.5: Quarter car model with two degrees of freedom

The dominant frequency present in the vehicle's vertical vibration response in most cases corresponds to the vehicle's sprung mass natural frequency and is around 1- 3 Hz depending on the vehicle type. For this reason, a natural suspension frequency of 2 Hertz is assumed for our Robot and the stiffness is calculated.

$$\omega_s = \sqrt{\frac{K_s}{m_s}(5.1)}$$

$$k_s = \omega_s^2 m_s \tag{5.2}$$

Because the acceleration of the sprung mass must be kept to a minimum value, a reasonable way to optimize the suspension is to choose a value of shock absorber damping from this expression:

$$c_{opt} = \sqrt{\frac{K_s}{m_s}} 2 \sqrt{\frac{K_p + 2K_s}{K_p}} \tag{5.3}$$

It is necessary to evaluate the tire stiffness k_p of the suspension assuming a natural frequency of the unsprung mass 10 times greater than the frequency of the sprung mass.

$$k_p = \omega_u^2 m_u \tag{5.4}$$

With a natural frequency m_u of 20 Hertz.

Suspension model		
m_s	15,25	*kg*
m_u	5	*kg*
ω_s	2	*Hz*
ω_u	20	*Hz*
K_s	2408	*N/m*
K_u	78957	*N/m*
c_{opt}	139,6	*Ns/m*

Table 5.2: Resulting data of the suspension 2DOF quarter car model

5.1.4 Stroke evaluation

It is fundamental to get the suspension displacements in order to understand which is the required space for the design of the wheel arch. Starting from the linear elastic law (Hooke's law) $F = Kx$, where F is the force of the spring, K is its stiffness and x the displacements, it possible to find these latter ones.

It has not to be forgotten that spring elastic characteristics of the suspensions coil spring shows a not perfect linear trend at the beginning and at the end of the characteristics due to the presence of the bump stop. In order to avoid an excessively long spring, bump stops are installed on the extremities of the spring itself (their intervention is represented by the green dashed lines at the extremities of the curve in Fig.6.7).

To evaluate the maximum suspension travel, the two most critical cases are examined and the maximum force that the suspension will undergo is defined. In the first case, the fully loaded drone is subject to the maximum lateral acceleration allowed for grip limits, in the second case it is analyzed with the maximum longitudinal acceleration. The situation that will present the higher force on the suspension, will be taken as a reference for the calculation of the stroke.

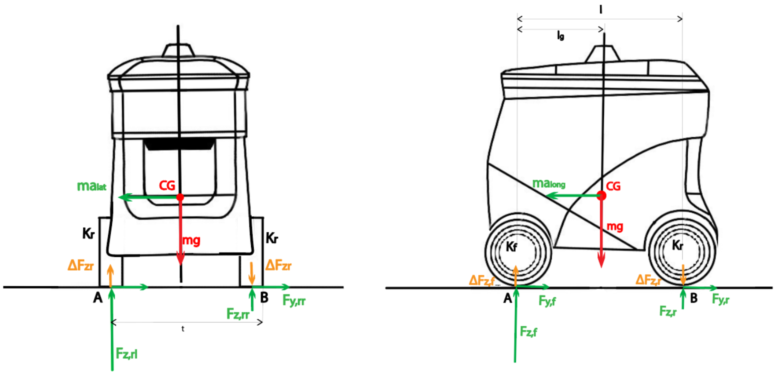

Figure 5.6: Lateral and longitudinal free body diagram

The equilibrium equations for rotations about the points A is:

$$\begin{aligned} ma_{lat}h_g - mg\frac{t}{2} + 2F_{z,rr}t = 0 \\ F_{z,rr} = \frac{m}{2}(\frac{g}{2} - \frac{a_{lat}h_g}{t}) \end{aligned} \tag{5.5}$$

$$\begin{aligned} ma_{long}h_g - mg\frac{l}{2} + 2F_{z,rl}l = 0 \\ F_{z,rl} = \frac{m}{2}(\frac{g}{2} - \frac{a_{long}h_g}{l}) \end{aligned} \tag{5.6}$$

The equilibrium equations for rotations about the points B is:

$$\begin{aligned} ma_{lat}h_g + mg\frac{t}{2} - 2F_{z,rl}t = 0 \\ F_{z,rl} = \frac{m}{2}(\frac{a_{lat}h_g}{t} + \frac{g}{2}) \end{aligned} \tag{5.7}$$

$$\begin{aligned} ma_{long}h_g + mg\frac{l}{2} - 2F_{z,fl}l = 0 \\ F_{z,fl} = \frac{m}{2}(\frac{a_{long}h_g}{l} + \frac{g}{2}) \end{aligned} \tag{5.8}$$

Where:

- a_{lat} is the minimum lateral acceleration between adhesion and capsize limit:

$$a_{lat} = min \begin{cases} a_{lat,max,adh} = CF_z\gamma \\ a_{lat,max,cap} = \dfrac{\dfrac{t_{cg}}{t} g\cos\alpha}{\dfrac{1}{2}\dfrac{d}{t} + \dfrac{a}{l}\dfrac{h_{rc}}{t}} \end{cases} \tag{5.9}$$

where C is the cornering stiffness coefficient and γ is the side slip angles present at each wheel.Typical values for the cornering stiffness coefficient are $0.16/^{o}$ for radial ply tires, while the slip angle is assumed of 3°. h_{rc} is roll center height, while h_{cg}, t_{cg} are referred to the position of center of gravity , d is the distance between roll and gravity centres, as illustrated in figure 5.6(a).

- a_{long} is the maximum longitudinal acceleration between adhesion and capsize limit:

$$a_{long} = min \begin{cases} a_{long,max,adh} = \mu_{x,max} g \cos\alpha - g \sin\alpha \\ a_{long,max,cap} = \dfrac{\dfrac{l_{cg}}{l} g \cos\alpha}{\dfrac{1}{2}\dfrac{d}{l} + \dfrac{t_{cg}}{t}\dfrac{h_{pc}}{l}} \end{cases} \tag{5.10}$$

where $\mu_{x,max}$ is the max tire friction coefficient and α the slope of the road. h_{pc}, is the height of pitch center and b is the distance between centre of gravity and pitch centre, as illustrated in figure 5.6(b).

Thanks to the presence of the suspensions the drone can have, in both steering or braking conditions, the maximum acceleration equal the one due to tires friction, because the overturning occurs at high accelerations. If it had been a rigid body the limit would have been the one for overturning. The results are summarize in the Table 5.3.

The vertical forces found and the geometry of the suspension designed allow to compute the force acting on the suspension in this two critical cases.

$$F_s = F_z \cos\theta \tag{5.11}$$

Where θ is the inclination of the suspension strut.
The stroke in the linear phase is:

$$x = \frac{F_s}{K_s} \tag{5.12}$$

For zero elongation the static load on the spring is the pre-load F_{s0}, when no external force acts on the vehicle. We can resume all the results in the table below, where vertical forces are divided by two number of wheels in front and rear axle:

From the Table 5.3 emerges as the most critical case is that of the steering, it is therefore chosen the stroke of the shock required by the vehicle, taking into consideration the maximum force that would act on the suspension in case of steering with maximum acceleration.

Braking			**Steering**		
$a_{long,max}$	4,9	m/s^2	$a_{lat,max}$	4,7	m/s^2
$F_{z,fl}$	174	N	$F_{z,rl}$	187,6	N
$F_{z,rl}$	51,5	N	$F_{z,rr}$	38	N
F_s	169	N	F_s	182	N
x_s	70	mm	x_s	75	mm
F_{s0}	109,5	N	F_{s0}	109,5	N
x_{s0}	45,5	mm	x_{s0}	45,5	mm

Table 5.3: Vertical forces acting on suspension strut

Thanks to the presence of bump, which considerably stiffens the resisting spring rate near the limit of its vertical movement, the suspension stroke set to 75 mm can support vertical loads up to about 290 N, as we can see in Fig. 5.7. The stop also isolates the sprung and unsprung members of the suspension under full deflection conditions so that none of the noise or vibrations are transmitted through to the body structure.

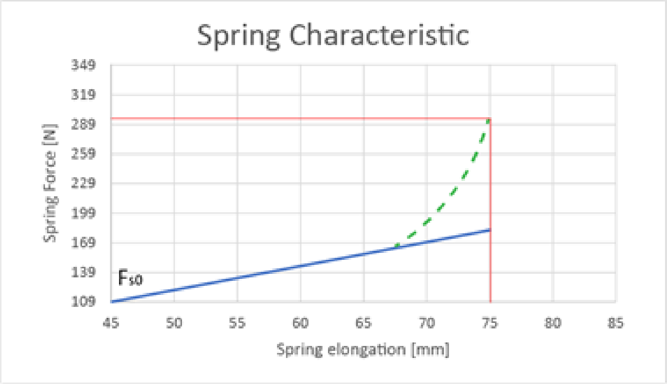

Figure 5.7: Suspension spring characteristic

5.2 Robot's vertical vibration response

In this section a complete analysis of the suspensions model from a design perspective, e.g., variation of suspension damping coefficient, stiffness and sprung mass in a frequency domain is being presented. The response of the model to random excitation is being studied through numerical simulations implemented in Simulink-Matlab environment.

Generally sinusoidal road excitation is used as road input to these models. However, the road surface has a lot of irregularities and hence, a vehicle is subjected to random excitation. So it is essential to study the response of a vehicle to random excitation.

5.2.1 Frequency response function

Three parameters are used to evaluate the suspension performance of a vehicle: the transmissibility, suspension travel and tire deflection/road holding. The three above mentioned parameters acts as trade-offs with respect to each other.

As we said in the section 5.1.3 the model chosen for our robot is the 2DOF Quarter car model where the 2 degrees of freedom are the translational displacement of the sprung mass and the translational displacement of the unsprung mass. These models are based on the assumption that the sprung mass and the unsprung mass are rigid. Frequency response functions are generally used to study the response. The linear suspension spring and viscous damping is assumed. Damping of the tire is neglected in the analysis.

It represents the automotive system at each wheel, the motion of the wheel assembly (z_u) and vehicle body (z_s) at any of the four wheels.
The equations of motion are:

$$\begin{cases} m_s\ddot{z}_s = -c(\dot{z}_s - \dot{z}_u) - k(z_s - z_u) \\ m_u\ddot{z}_u = -c(\dot{z}_u - \dot{z}_s) - k(z_u - z_s) - k_p(z_u - h) \end{cases} \tag{5.13}$$

In matrix form:

$$M\ddot{q} + C\dot{q} + Kq = Hh \tag{5.14}$$

Where $q= \begin{Bmatrix} z_s \\ z_u \end{Bmatrix}$ and $h= \begin{Bmatrix} h_r \end{Bmatrix}$ the road input profile

$$\text{Mass matrix } M= \begin{bmatrix} m_s & 0 \\ 0 & m_u \end{bmatrix}$$

$$\text{Damping matrix } C= \begin{bmatrix} c & -c \\ -c & c \end{bmatrix}$$

$$\text{Stiffness matrix } K= \begin{bmatrix} k & -k \\ -k & k+k_p \end{bmatrix}$$

$$\text{Forcing matrix } H= \begin{bmatrix} 0 \\ k_p \end{bmatrix}$$

For the evaluation of suspensions performance the following frequency response functions are analysed:

$$Trasmissibility = \frac{z_s}{h}$$

$$Unsprung\ mass\ deflection = \frac{z_u}{h}$$

$$Sprung\ mass\ acceleration = \frac{\ddot{z}_s}{h}$$

$$Handling = \frac{F_z}{k_p h}$$

All these frequency response functions are evaluated in a range of 0 to 180 rad/s, for three values of damping coefficient $[co, co/2, 2co]$, where co is the optimum damping and also considering the variation of vehicle mass during its mission in which it empties leaving packages to customers.

- The mdof FRFs can be calculated from the receptance matrix, i.e. the inverse of the dynamic stiffness matrix:

$$K_{dyn}(\omega) = (K + i\omega C - \omega^2 M) \tag{5.15}$$

$$R(\omega) = Kdyn^{-1} \tag{5.16}$$

$$R(\omega) = \begin{bmatrix} r_{1,1}(\omega) & r_{1,2}(\omega) \\ r_{2,1}(\omega) & r_{2,2}(\omega) \end{bmatrix} \tag{5.17}$$

$$\begin{aligned} \frac{z_s}{h}(\omega) &= r_{1,2}(\omega) \cdot k_p \\ \frac{z_u}{h}(\omega) &= r_{2,2}(\omega) \cdot k_p \end{aligned} \tag{5.18}$$

- Sprung mass acceleration can be computed from position:

$$\frac{\ddot{z}_s}{h}(\omega) = -\omega^2 z_s h(\omega) \tag{5.19}$$

- Handling is assessed computing the vertical force:

$$\frac{F_z}{k_p h}(\omega) = k_p(h - z_u)k_p h = 1 - z_u h(\omega) \tag{5.20}$$

5.2.2 Results and Analysis

Numerical simulations of the suspension model in section 2 have been implemented. Road input excitation is simulated by sine wave with constant amplitude and wavelength. The vehicle forward velocity is linearly increased, such that the excitation frequency rises up and the vehicle ride response can be depicted. In the analysis carried out the graphs relating to the acceleration and displacement of the sprung mass are used to improve the driving comfort of the vehicle, which even if it does not have passengers inside it must ensure the integrity of the most fragile parcels; graphs relating to the displacement of the unsprung mass and ground force are useful for the evaluation of vehicle stability.

The first simulation is developed by varying the damping coefficient.

Figure. 5.8 (a) shows how a shock absorber with a lower damping coefficient, transmits a greater vertical displacement to the mass of the vehicle body in the frequency range close to the natural frequency of the sprung mass. Whereas between the natural frequencies of the sprung and unsprung mass the behavior is opposite, so soft damping value reduces transmissibility, and then equalizes at the natural frequency of the unsprung mass.

From Fig. 5.8 (c) it can be noted that, close to the sprung mass natural frequency, the higher the damping ratio, the lower the sprung acceleration will be. For higher frequency range, trend changes and a lower damping ratio brings a lower sprung acceleration. At a frequency close to the natural frequency of the unsprung mass, in the case where neglecting the tire damping, the damping ratio has little effect on the response of the sprung mass. As the damping increases, the resonant peaks at sprung-mass natural frequency are attenuated, but the isolation is lost both at high frequency and at frequencies between the two natural frequencies of the system, sprung and unsprung natural frequencies. The lack of isolation between the two natural frequencies is caused by the increased coupling of the two degrees of freedom with a stiffer damper. The lack of isolation will result in a harsher vehicle ride and it may physically damage vehicle. Whereas a lightly damped suspension will yield a more comfortable ride, but would significantly reduce the stability of the vehicle during turns, as we can see from Fig. 5.8 (d). Therefore, a suspension design is an art of compromise between these two goals.

In conclusion as first analysis from these graphs you can see that a passive suspension with a damping coefficient tendentially stiffer than the optimal one is satisfactory for this type of application. Not having to take into account the comfort of the passenger and human sensitivity to the frequencies between the two natural frequencies, the most important aspect is the stability of the vehicle. The

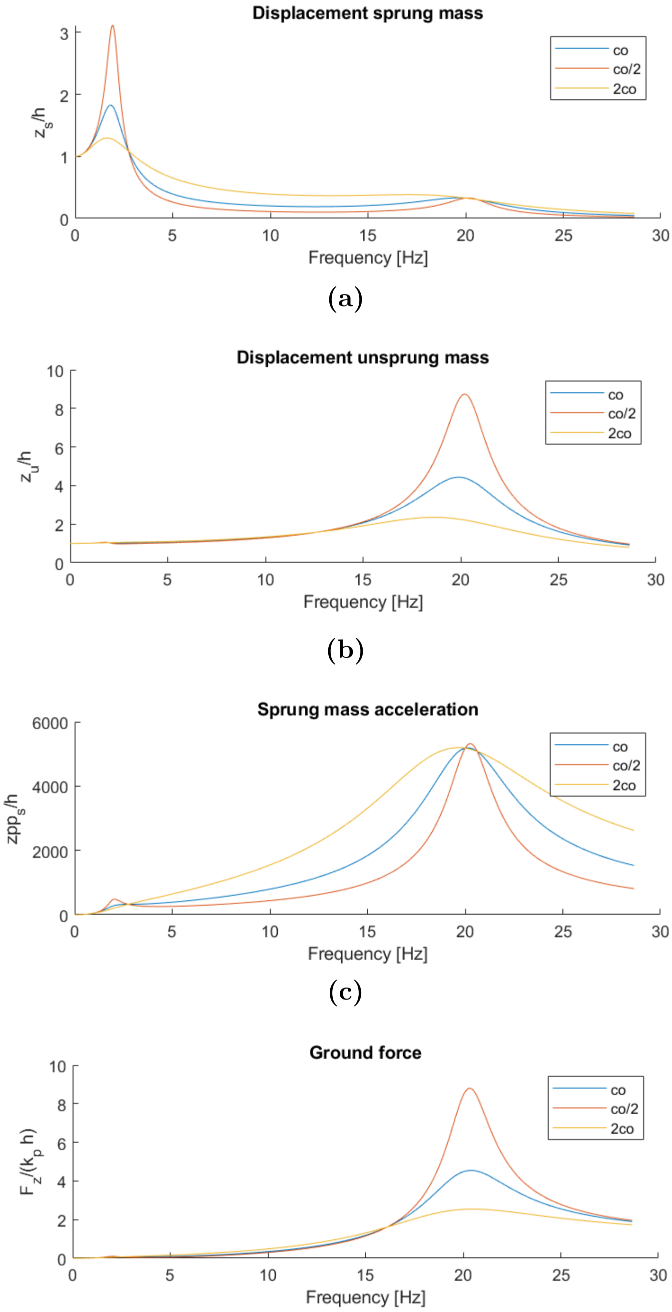

(a)

(b)

(c)

(d)

Figure 5.8: Frequency Response Functions of Vehicle Model by varying the damping coefficient

vehicle handling is dictated by the vertical force graph (5.8-d) and the displacement graph of the unsprung mass (5.8-b). From these two graphs it emerges that a suspension with stiffer damping coefficent is better as it reduces both the peaks of the two frequency response functions in correspondence of the natural frequencies of the vehicle body and the wheel. We therefore opt for a damping coefficient slightly higher than the optimal one, even if the comfort target is not required, too high vertical accelerations could damage fragile packs contained in the drone.

However, considering the primary function of the Drone it is also important to repeat the analysis of the response functions introducing a variation of the sprung mass. The vehicle examined during the completion of its mission will empty leaving the packages to the customer and this determines a different dynamic response to road stress.

Referring to Fig. 5.9 (c), it can be noted that below the sprung mass natural frequency, lower values of sprung mass reduces body vertical acceleration. With further increase of the excitation frequency, the body acceleration is increased for lower mass until the arrival to the natural frequency of the sprung mass, where the increase of the acceleration of the vehicle body in association of the reduction of mass is remarkable. To mitigate this effect, we opt for a reduction of the damping coefficient, bringing it back to the optimal value.

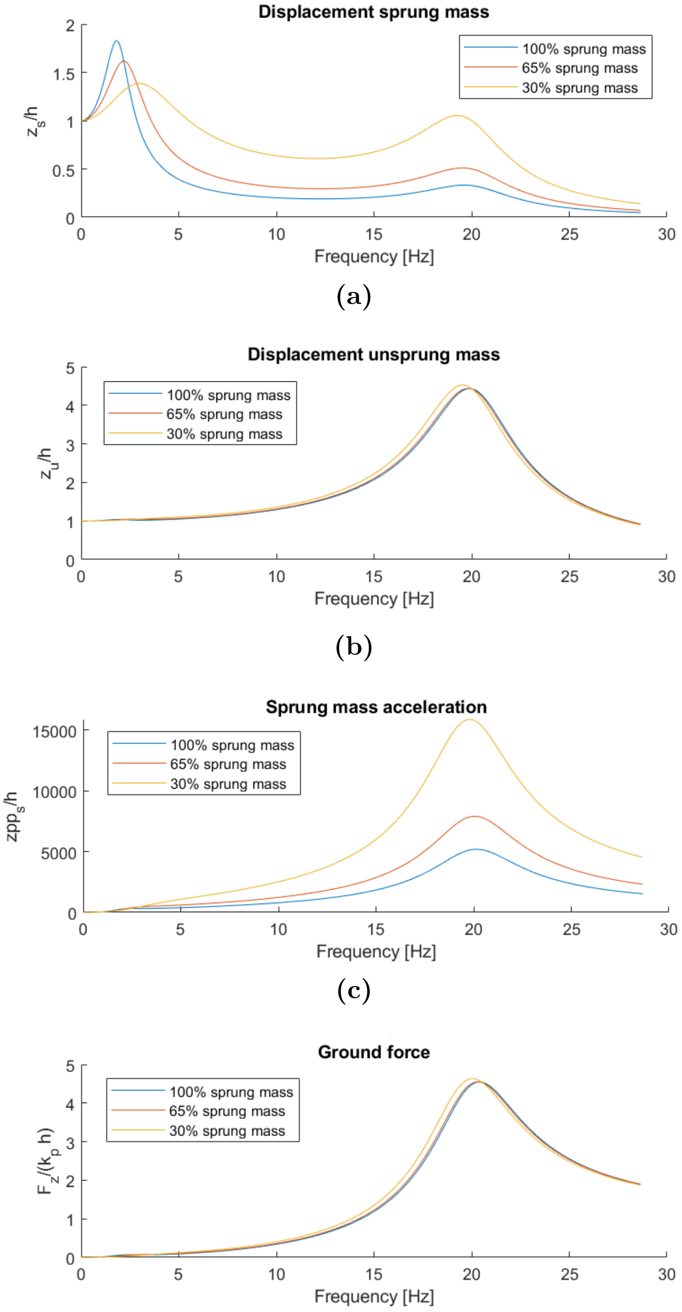

Displacement sprung mass

(a)

Displacement unsprung mass

(b)

Sprung mass acceleration

(c)

Ground force

(d)

Figure 5.9: Frequency Response Functions of Vehicle Model by varying mass of the vehicle body

5.3 Dynamic Robot simulation

In this section, the system model that has been used to study the passive suspension system behavior with parameters found in the precedent section, is presented. Firstly an overview of the overall model is given, then each component is addressed in order to give a more detailed insight, along with the equations that constitute their mathematical description.

The results of the simulation that have been run are presented through the analysis of the vertical body acceleration, the suspension travel and the roll angle in different testing condition that will be explained in detail in the following subsection. For the suspension components, it is assumed that the relationships existing between the elastic force and the displacement and the one existing between the damping force and the velocity, are of linear type [19].

5.3.1 System modeling overview

The Simulink model of suspension system is composed by three main blocks: the road profile generator, the robot's quarter car model,divided into the vehicle mass model and the wheel dynamic model as shown in figure 5.10. The main idea behind this structure, is to obtain the vertical acceleration profile of the drone and the sprung and unsprung mass displacement with the suspension system adopted, in accordance with a road profile as realistic as possible for the robot path.

The model that will be presented has been developed in order to simulate the behavior of vehicle in presence of some different driving situations: random road profile, step road profile and lateral acceleration in steering condition for roll angle analysis.

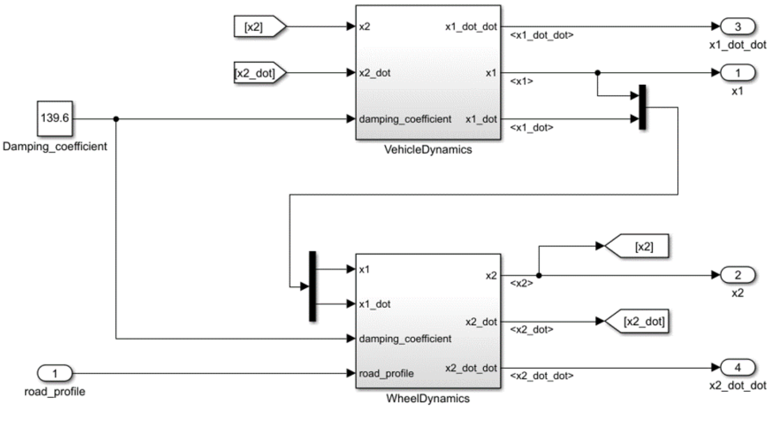

Figure 5.10: Simulink model of the suspension system, representing the plant of the Quarter car divided in 2 subsystems

Considering Equation of motion 5.13 the block referred to the sprung and unsprung mass are represented in the MATLAB-Simulink software as shows figure 5.11

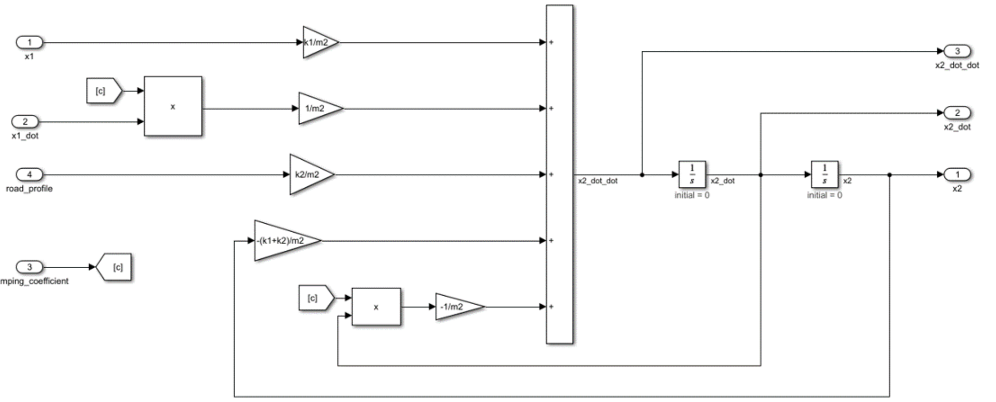

(a) *Wheel dynamics*

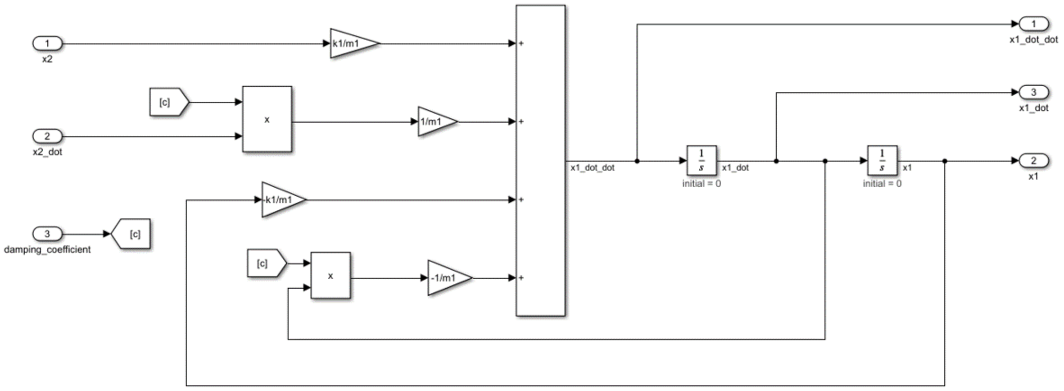

(b) *Vehicle dynamics*

Figure 5.11: Sprung mass and Unsprung mass Simulink model

5.3.2 Test 1: Random Road Profile

The aim of this simulation is to represent the classical scenario when the car hits a bump or a hole, in order to evaluate the vertical acceleration and the suspension travel [20].

The sub-system road profile selector generates a unique road profile by randomly switching among four samples of road profiles: bumps, holes, plains and flat with noise road profiles.

- Bump: is a trapezoid spanning from 0 $m\ to$ 0.06 m

- Hole: is a trapezoid spanning from 0 $m\ to\ -0.06\ m$
- Flat Profile: constant signal at 0 where a gaussian noise is added with amplitude between -0.001 and 0.001 simulating a flat road.

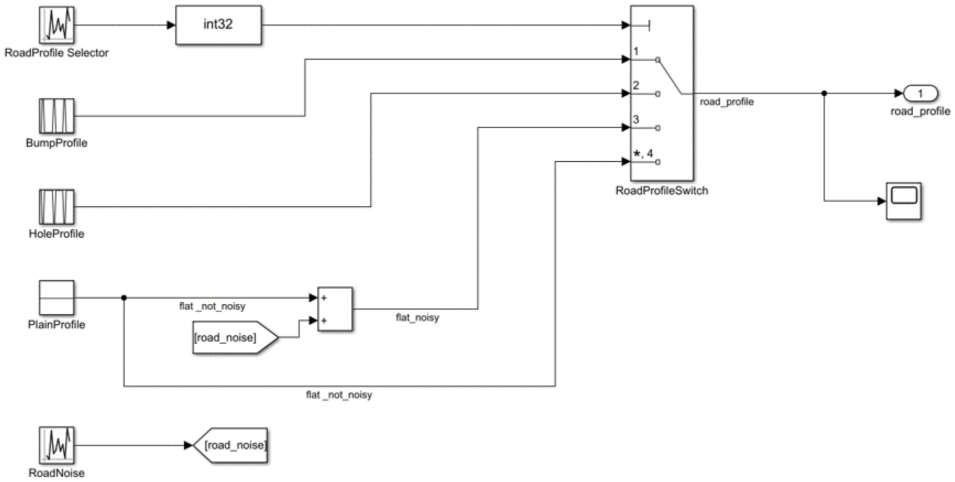

Figure 5.12: Simulink model of the road profile generator

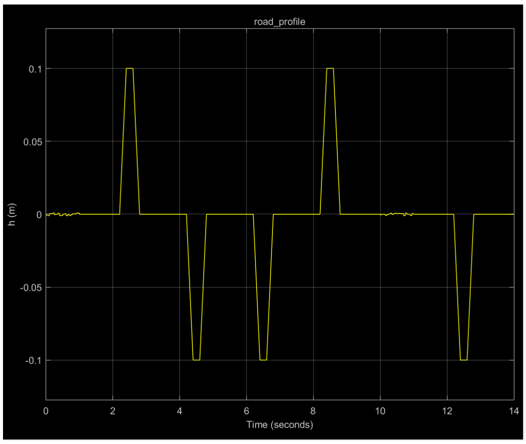

Figure 5.13: Road profile with bump, hole and flat configurtions

5.3.2.1 Results

The simulation was performed for a period of 14 seconds. The body acceleration and body displacement performances of the passive system are shown in Figure 5.14 and 5.15. From the figures, it is clear that the active system is able to significantly reduce amplitude of unwanted body motions in the forms of body acceleration. the acceleration range in fact goes from 50/ms for the wheel to about 7 m/s for the suspended mass when the vehicle exceeds a bump of 0.06 meters.

mettere i displacement

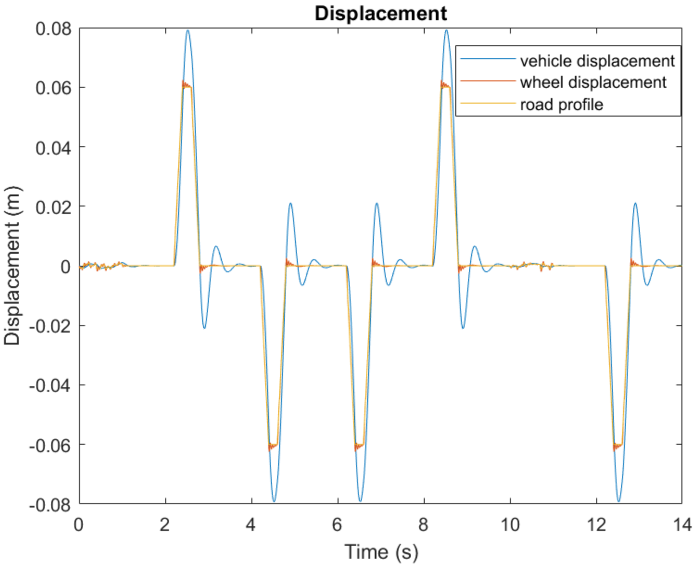

Figure 5.14: Vehicle and wheel displacements due to road irregularities

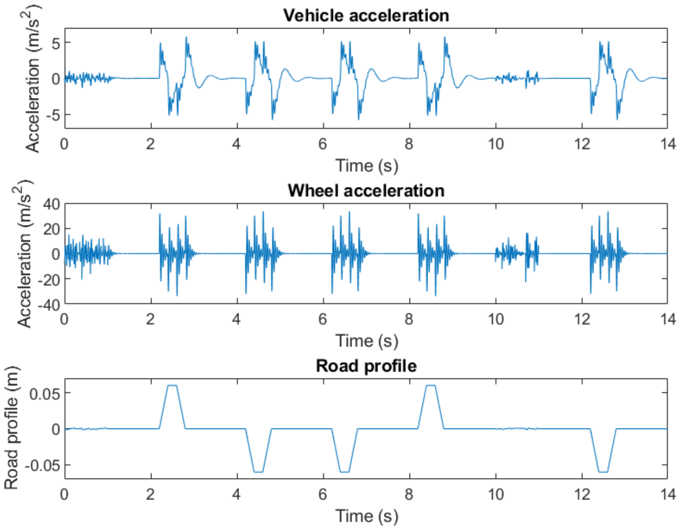

Figure 5.15: Vehicle and wheel acceleration due to road irregularities

5.3.3 Test 2: Step Road Profile

From the test of overcoming a step of 0.05 meters it is possible to analyze the overshoot, the suspension settling time and the damping force computed as the damping coefficient times the relative velocity between sprung and unsprung mass.

Suspension immediately after the step has a peak damping force of about 700 N, an overshoot of 0.03 m and regains its initial position after a time of about 2 seconds.

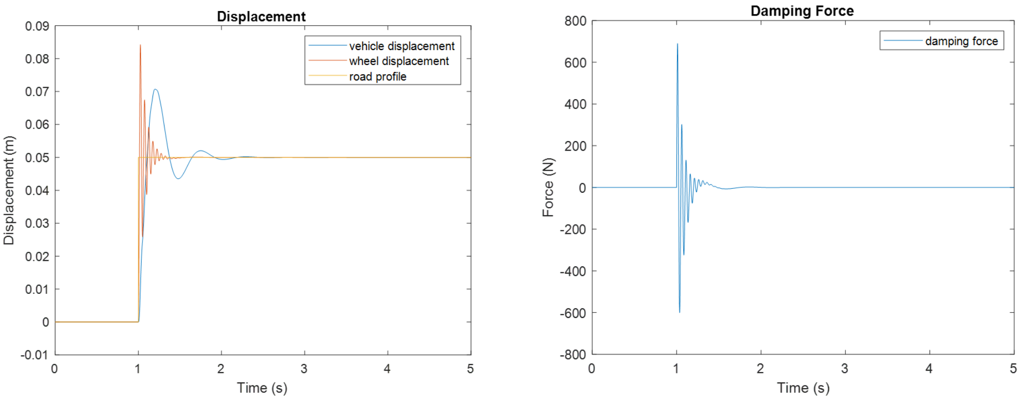

(a) **(b)**

Figure 5.16: Suspension response to road step excitation

5.3.4 Test 3: Body Roll Behavior

In this test is analyzed the capability of the system to cope with the roll behavior of the vehicle due to lateral load transfer during cornering. In particular, when the Robot undertakes a curve, the load shifting phenomenon takes place. Due to this phenomenon the vehicle will bend laterally, around the roll axis, forcing the suspension to compress in correspondence of one wheel of the axle and to extend on the other one. The suspension should be able to compensate for this situation by means of an appropriate stiffness and damping coefficient.

During cornering the vertical dynamic force on the tires can be calculated as:

$$F_{dyn} = (m_s + m_u) a_y \frac{h_{CG}}{T} \tag{5.21}$$

Considering the position of roll center of the suspension, the vertical forces exerted on the tires by sprung mass F_t can be calculated as:

$$F_t = m_s a_y \frac{h_{rc}}{T} \tag{5.22}$$

Where h_{rc} is the roll center height.
So vertical force on suspension due to cornering acceleration:

$$F_s = C_\gamma(F_{dyn} + F_t) \tag{5.23}$$

The coefficient C_γ equal to 0.95 are introduced since the struts are not exactly vertically mounted. The load transfer is based on the values calculated in the Table 5.3.

In particular, the load transfer and the consequent roll behavior can be represented in the quarter car model as a disturbance force which acts on the sprung mass. The profile of the load which is used to model the disturbance derives from [21], by changing data values according to our application. The realization in the Simulink environment of the force is shown in figure 5.17. As can be seen, it is represented as a force acting for 3s with a value of 66 N

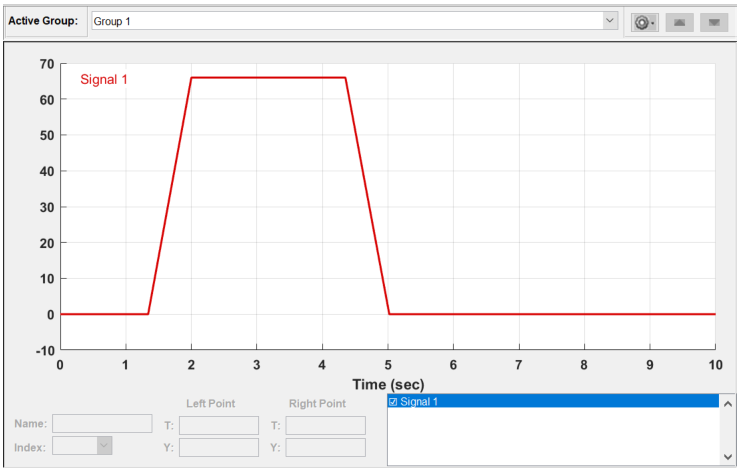

Figure 5.17: Simulink force profile representing roll behavior

In order to perform the test, the overall system model is modified with respect to the original scheme. In particular the road disturbance is set to zero, as only the behavior during cornering must be observed. Furthermore, in the sprung mass force balance is added the force term representing the load behavior (figure 5.18).

Always according to [21], the test conditions lead to a negligible displacement for the unsprung mass. As a consequence, its influence is not considered in the definition of the rolling behavior of the drone, which will be evaluated only basing on the sprung mass dynamics. Taking into account this last consideration, the observed quantity is defined as the the roll angle, which can be expressed starting from the sprung mass displacement:

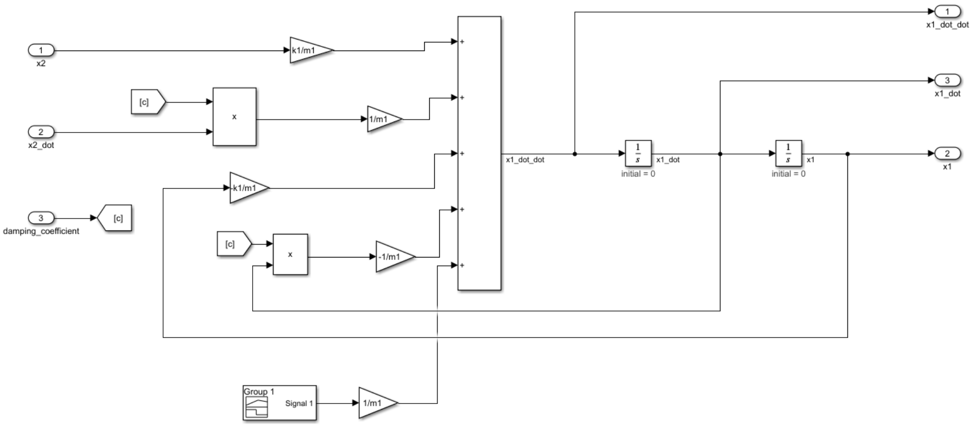

Figure 5.18: Simulink sprung mass scheme for roll behavior analysis

$$\phi = arctan(\frac{2z_s}{T}) \tag{5.24}$$

where z_s is the sprung mass displacement and T is the track width.

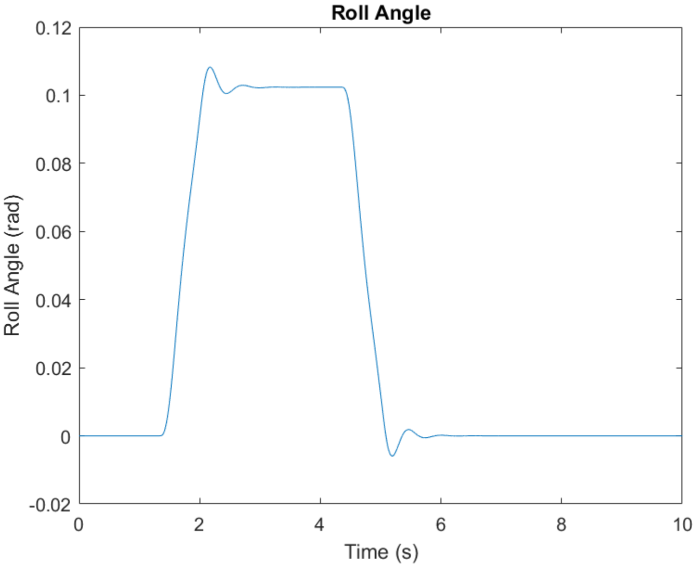

Figure 5.19: Roll angle during cornering manoeuvre

From the graph 5.19 you can see the obtained roll angle that is equal to about 0.11 rad that correspond to 6.3 degrees of inclination of the drone during a curve with maximum acceleration of 4.7 m/s^2. The suspension has a satisfactory behavior because the roll angle is fairly small, this allows a management of the internal packs without problems of contact between them during critical curve situations.

Chapter 6

Steering system

In this design phase, the study of various structural and technological solutions led to the realization of the final steering system. A delivery robot must definitely be equipped with high manoeuvrability, each maneuver must also be as accurate and precise as possible, which is why the design of the steering system requires special attention.

For the studio application, the four wheel drive steering system is the solution that best meets the requirements of accuracy and maneuverability and is, Moreover, able to obtain steering maneuvers with reduced radii of curvature that allow you to easily switch between pedestrians and architectural barriers of the city.

6.1 Design preliminary outline

6.1.1 Type of steering system

Steering manoeuvres can be implemented in the following ways:
- Slip steering: there is no steering mechanism. The steering occurs when the wheels or the track of one side, operate at a speed different from the opposite side and the system turns in the direction of the slower side, sliding on the ground. The two sides must, therefore, be moved independently and the wheels or track of the same side are usually mechanically locked and synchronized with each other. With this steering system the vehicle can easily change direction, making it a highly manoeuvrable mechanism, however, the steering capabilities depend on the terrain with which the vehicle enters contact: on rough surfaces with a low coefficient of friction, the steering manoeuvre becomes inaccurate. Its simple realization that you undoubtedly translates into a low cost, accompanied by high mobility, Unfortunately, it collides with a very low accuracy that makes it, therefore, not suitable for the application in the studio.

- Articulated steering: this steering system uses two or more elements belonging to the chassis and connected to one of the two axes, which joined together, rotate thanks to the action of one or more actuators, thus obtaining the steering manoeuvre. The cost, the complexity of the system and the control are low; however, the maneuverability of the system is not high, it is possible, in fact, to obtain trajectories with rather high radii of curvature
- Ackermann steering: two wheels of the same axis rotate around two different steering axes (called Kingpins), but their steering angles are controlled by a mechanical link. The connection meets Ackermann's conditions: that is, it makes the lines perpendicular to the middle planes of the steered wheels and passing through the point of contact of the wheels with the ground, both converge in the center of instant rotation of the vehicle. It is important, at this point, to make a simple consideration about the Ackermann mechanism: through a trapezoidal connection, like the one shown in figure 6.1, one can only approximate the Ackermann condition.
- Independent steering: 2WD or 4WD. The wheels can rotate independently, each around a certain axis, under the action of one or more actuators. Depending on the type of control used, the Ackermann conditions can also be met. At low speeds (generally less than 30 km/h), it is possible to orient the two front wheels and the two rear wheels in opposite directions obtaining a bend radius much smaller than all the other systems analysed above, In particular, the reduction of the bending radius obtained with a 4WS system of this type is less than about 40

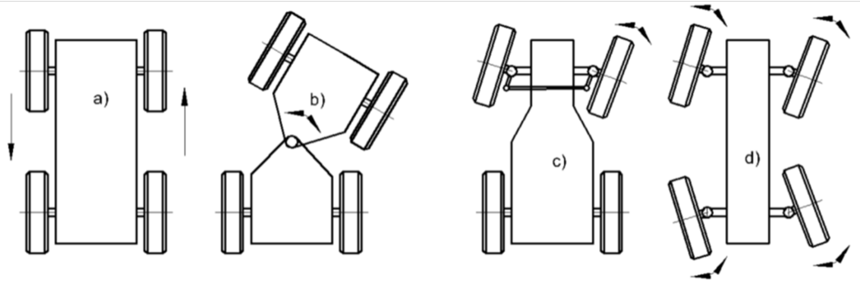

Figure 6.1: Steering system typology

6.1.2 Selected steering mechanism

For our vehicle we choose the configuration *d* of the figure 6.1. The set of connections for steering the two front and rear wheels is shown in the following figures. (6.2, 6.3)

The DC electric motor is positioned on a C bracket ,once actuated, the servo motor brings in rotation the gray arm that is connected with the center of the wheel. The latter thanks to the torque exerted by the servo motor can rotate by starting the entire steering system.

In the figure 6.3 are visible images of a steering left and a right for the front steering system.

(a) *Front wheel* **(b)** *Rear wheel*

Figure 6.2: Diagram of the steering mechanism

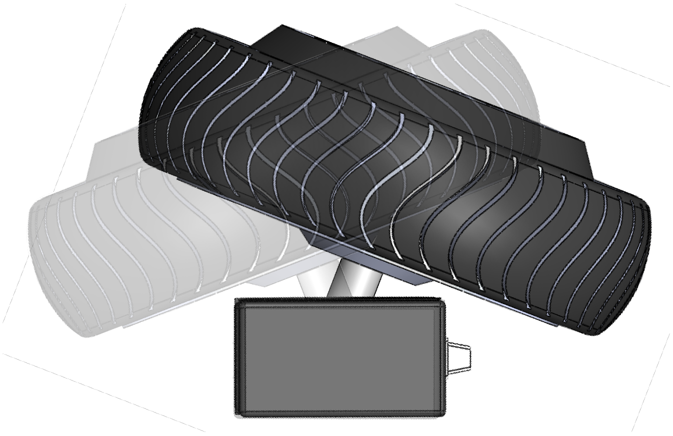

Figure 6.3: Operation of the proposed steering mechanism

6.1.3 Sizing of the servo motor

As seen in the previous section, the steering system is an autonomous system driven by four electric motors other than those used for propulsion. Each motor will be fixed on the mini wheel axle and will only actuate the steering mechanism of the single wheel. Before proceeding with the sizing and the choice of engines, it is necessary to know the torque necessary to operate the steering system that will be strongly influenced by the amount of friction present between the tyre and the ground and, obviously, by the longitudinal dimensions of the steering system. The concept underlying the calculation of the steering torque is that the torque required to steer the vehicle wheel must be greater than the resistant torque:

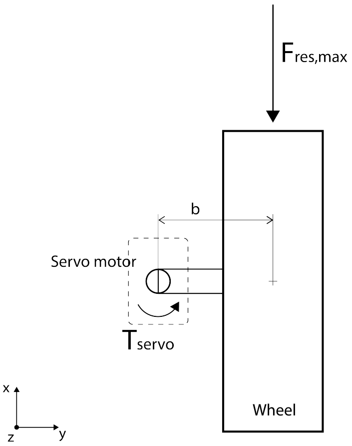

Figure 6.4: Torques acting on a steering wheel

The torque required to the servo motor will be:

$$T_{servo} = F_{res,max} \cdot b \tag{6.1}$$

Where b is the length of the shaft joining the wheel centre to the steering axle of the servo motor; the smaller the size r and the smaller the steering torque. The distance between the two axles, however, for a matter of physical encumbrances can not be too small: the tire, in fact, needs enough space to rotate without coming into contact with the frame or other parts fixed to it. The distance b shall be fixed at a value of 7 cm to ensure a maximum steering angle of 40 degrees. The maximum resistance force can be calculated as follows:

$$F_{res,max} = max(\frac{P_{wh}(t)}{v_{drive\ cycle}(t)}) \tag{6.2}$$

Where taking again the equations developed in chapter 3, we have:

$$P_{wh}(t) = P_{trac}(t) + J_{wh} \cdot \dot{\omega_{wh}} \cdot \omega_{wh} \tag{6.3}$$

$$P_{trac}(t) = M_v v(t)\frac{dv(t)}{dt} + P_{res}(t) \tag{6.4}$$

$$P_{res}(t) = (\mu_r M_v g \cos\alpha + \frac{1}{2}\rho C_d A_f v^2 + M_v g \sin\alpha)v \tag{6.5}$$

From the calculations performed on the Matlab file containing the driving cycle of the drone emerges a maximum torque required to the servo motor of:

$$T_{servo} = 11\ Nm \tag{6.6}$$

Once you notice the torque that each motor of the two different steering systems must apply, you can proceed with the sizing of the steering motor.

The steering rod shall rotate ± 40° in a time t of $2s$; in addition, the acceleration transients shall be assumed to be less than $200ms$:

$$\omega_{servo} = \frac{\delta_s}{t} = \frac{40°}{2s} = 0{,}35\frac{rad}{s} \tag{6.7}$$

corresponding to a rotation speed of 3,3 rpm and an acceleration of:

$$a_{servo} = \frac{\omega_{servo}}{t_t} = 1{,}74\frac{rad}{s^2} \tag{6.8}$$

The characteristics of the steering motor are, therefore:

- Rotation speed of at least 3,3 rpm, 0,05 rps;
- Torque delivered of at least 11 Nm;
- Power output of at least36 W.

The choice falls, also in this case, on an electric motor DC of brushless type, fed to 24 V. It is important to underline that the motors used for the handling of the two steering systems, will certainly not be required a continuous operation during the entire operation of the drone, but only in the steering manoeuvres necessary to move from one row to another and in those useful to avoid obstacles. For this reason, for the power supply of both engines the steering are not necessary other batteries as those used for the propulsion system have sufficient autonomy to power the two steering systems.

Servo Motor Parameters		
Max Torque	200	*Kg.cm*
	19,6	*Nm*
Imput power	24	*V*
No-load speed	0.33	*giri/sec*
Size	117x67x96,5	*mm*
Weight	650	*g*

Table 6.1: Data-sheet of selected servo motor

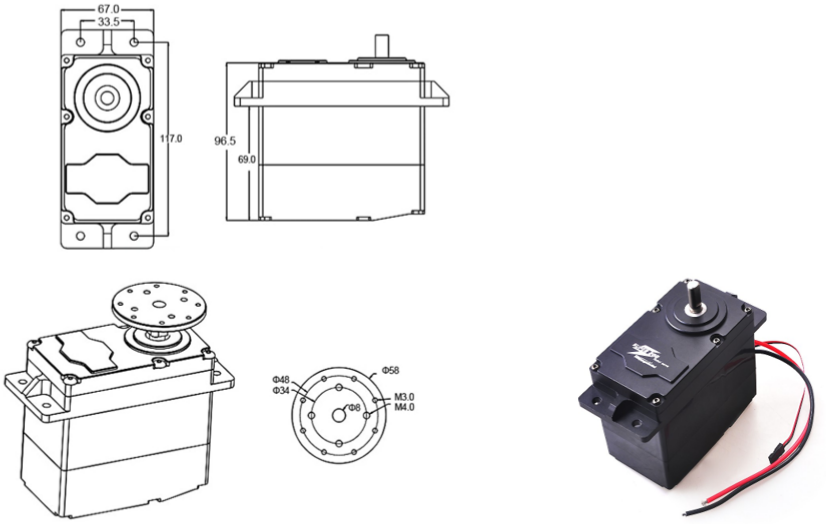

(a) *Dimensions* **(b)** *Device*

Figure 6.5: Technical drawing of selected servo motor

6.1.4 Wheel arch sizing and robot platform

In the following analysis, the aim is to evaluate an adequate dimensioning of the wheel arches and of the robot floor pan, taking into account all the different load conditions under which the vehicle itself is subjected and the maximum steering angle admissible.

Considering the vehicle in full load condition, we evaluated the values of the displacements reached by the vehicle in order to properly compute all the space required for the wheel arches, both in side view both in top view.

From the collected data of the servo motor dimensions on each wheel we are able to compute the maximum steering angle (40°) that avoids contact between wheel and engine leaving some proper clearance, like we can see in Fig. 6.6

It is necessary to consider that the wheel does not rotate around its contact point with the ground, but rotates around the point of application of the axis of rotation of the motor, which is 66 mm from the center of the wheel.

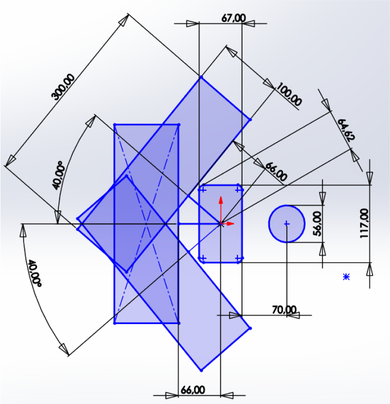

Figure 6.6: Available space for steering wheel avoiding contact with the motor

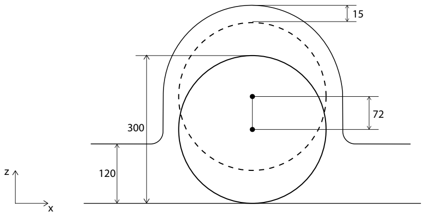

(a) *Side view*

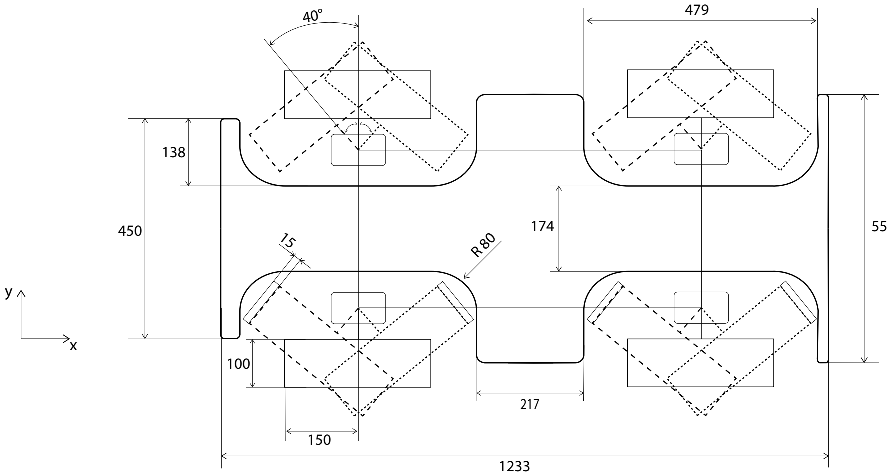

(b) *Top view*

Figure 6.7: Sizing of the wheel arches and of the robot floor pan

By taking into account also the snow chains and dirt thickness applied on the tire (about 15 *mm*), is possible to choose the proper space available in top view. For what concerns the lateral view, the key aspect was the evaluation of the displacements of the vehicle, passing through the computation of the stiffness of the springs of the suspensions.

In side view, relative displacement between tire and car body is set to the max suspension stroke evaluated in section 5.

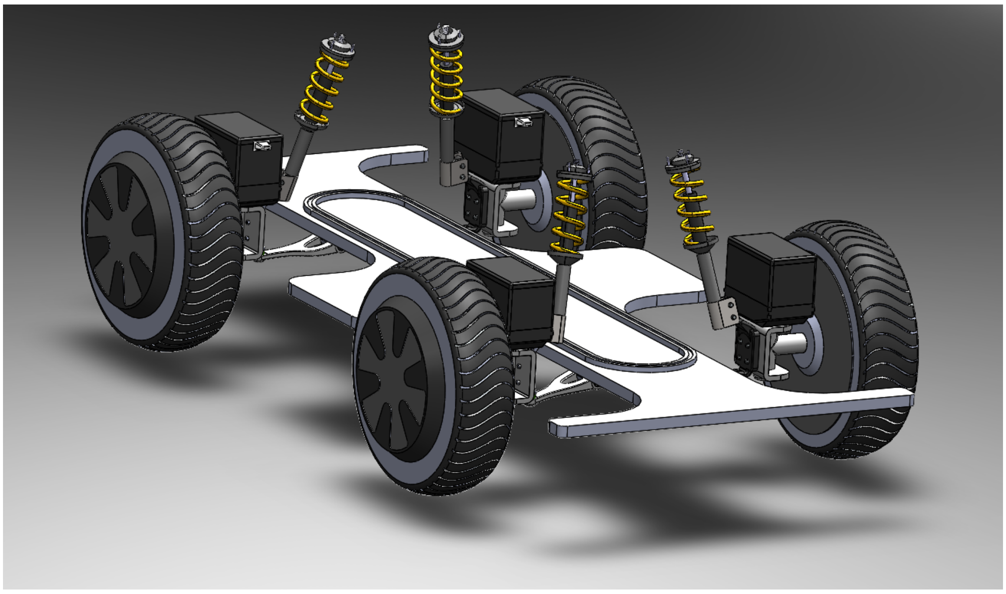

Figure 6.8: Three-dimensional design of the robot base with suspension and steering system.

The overall result is represented in the figure6.8, where we can also see the guide for the sliding of the piston that allows the release of the package selected by the customer. In the space between the guide will be placed the battery pack.

6.2 Graphical approach

The main specification to be met by the steering system is to enable steering manoeuvres with a reduced radius of curvature. The radius of curvature is simply the radius of the trajectory (similar to a part of circumference) that the vehicle makes during a turn. The calculation is made by considering the distance between the centre of mass of vehicle and the centre of the circumference described by the vehicle itself, as shown in the figure 6.9.

For the analysis of the steering manoeuvre and, consequently, for the calculation of the radius of curvature, reference is made to a simplified model called bicycle model or single track model [22].

The model presented below is based on a series of simplifying hypotheses useful for referring to a condition of use in which the vehicle has the least number of appreciable movements but is still capable of curving. It is assumed, initially, that the vehicle is moving on a flat and horizontal road with a constant feed speed v; in this way the movements of shaking (motion along the vertical axis) and pitching (rotation around the horizontal axis) are neglected. Disregarding also the inertia related to rolling, it is assumed indirectly that the vehicle runs on curves with relatively wide radii (vehicle length much less than the radius of curvature) with a low speed. Neglecting pitch, roll and shake motions implies that the vehicle moves with an exclusively flat motion.

The assumptions adopted are summarised below:

- The vehicle moves in a horizontal plane (there are no transverse and longitudinal gradients of the road);
- The wheels of each axle shall be condensed into a single equivalent wheel;
- The vehicle speed is set constant;
- The steering angles, drift and trim are very small;
- The radius of curvature of the trajectory is greater than the dimensions of the vehicle;
- Load transfers are neglected.

This also applies to kinematic steering conditions which, as indicated above, imply that the wheels are in the pure rolling condition: $\alpha = 0$ and lateral forces are zero. Applying all the assumptions of the bicycle model on a vehicle with type 4WS steering system and with opposite axle rotations, the following diagram is obtained (Fig. 6.9)

The points $F(x_f, y_f)$ and $B(x_b, y_b)$ are the center of the front and the rear axle of the vehicle, respectively. The point $M(x, y)$ is the geometric center of the vehicle, and the point C is the center of rotation of the vehicle.R denotes the radius of rotation of the vehicle. The wheelbase L is the distance between the front and rear axles, and the wheel track W refers to the distance between the left and right wheels. The heading angle ψ refers to the angle between the body direction and the X axis in the global coordinate system XOY. The center of mass slip angle β is the angle between the speed v_m at the point M and the direction of the body.

We can use the Sine law together with the trigonometric identity to determine the radial r_{cf} from (x_c, y_c) to the imaginary front center wheel. Similarly for r_{cb}. This yields:

$$\begin{aligned} r_{cf} &= L\frac{\cos(\delta_r)}{\sin(\delta_r - \delta_f)} \\ r_{cb} &= L\frac{\cos(\delta_f)}{\sin(\delta_r - \delta_f)} \end{aligned} \tag{6.9}$$

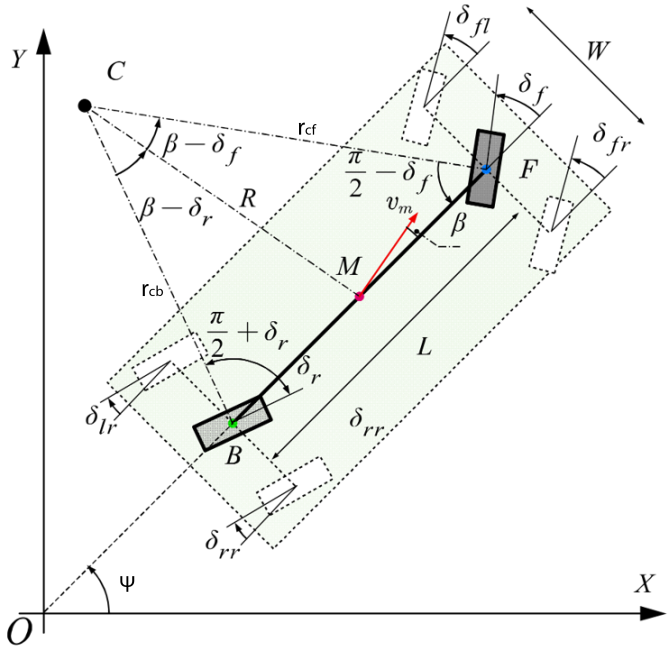

Figure 6.9: Bicycle model on a vehicle with 4WS steering system in opposite axle rotations

We can also calculate x_c, y_c quite easily once we know r_{cb}

$$\begin{gathered} x_c = -r_{cb}\cos(\delta_r) = -r_{cf}\cos(\delta_f) \\ y_c = r_{cb}\sin(\delta_r) \end{gathered} \tag{6.10}$$

Finally after calculating x_c and y_c, we can get r_{fl} and δ_{fl}.

$$\begin{gathered} r_{fl} = \sqrt{(x_c + \frac{W}{2})^2 + (L - y_c)^2} \\ \delta_{fl} = \arctan(\frac{L - y_c}{x_c + \frac{W}{2}}) \\ r_{fl,w} = r_{fl} - S \end{gathered} \tag{6.11}$$

Where S is the length of the shaft linked to the rotation point of servomotor. Now we can also calculate the remaining angles δ_{fr}, δ_{rr}, δ_{rl} as:

$$
\begin{aligned}
\delta_{fr} &= \arctan(\frac{L - y_c}{x_c - \frac{W}{2}}) \\
\delta_{rr} &= \arctan(\frac{-y_c}{x_c - \frac{W}{2}}) \\
\delta_{rl} &= \arctan(\frac{-y_c}{x_c + \frac{W}{2}})
\end{aligned}
\tag{6.12}
$$

So we now have the turning angles for our wheels in maximum turning angle.

Steering Angles			
2WS		4WS	
δ_{fl}	40°	δ_{fl}	40°
δ_{fr}	31°	δ_{fr}	25°
δ_{rl}	0°	δ_{rl}	-25°
δ_{rr}	0°	δ_{rr}	-40°
R	1 m	R	0,6 m

Table 6.2: Steering angle of each wheel in 2WS and 4WS mode

Where R is the turning radius obteined as:

$$
\begin{aligned}
R_{2WS} &= r_{cf}\cos(\delta_f) \\
R_{4WS} &= L \cdot \cot(\delta_f)
\end{aligned}
\tag{6.13}
$$

The table shows all the corners of the steering wheels in two driving configurations 2WS and 4WS starting from the maximum allowed angle and the out-of-phase steering for the 4WS. In this way it is possible to notice the variation of the minimum radius of curvature that the robot can reach in the two steering modes. As we can see we get a reduction of about 40% with the 4 steering wheels obtaining a minimum bending radius of 0.58 meters.

Given the desired speed of the vehicle as v_{cf} can calculate how fast the imaginary front center wheel must revolve.

ω_{cf} is the angular velocity of the imaginary centre front wheel:

$$
\omega_{cf} = v_{cf} \cdot 2\pi r_{cf} \tag{6.14}
$$

So if the desired rotation is ω_{cf} around the front center point, we have the angular speeds of each individual wheel:

$$\begin{aligned}
\omega_{fr,w} &= \omega_{cf}\frac{r_{fr,w}}{r_{cf}}\\
\omega_{rr,w} &= \omega_{cf}\frac{r_{rr,w}}{r_{cf}}\\
\omega_{fl,w} &= \omega_{cf}\frac{r_{fl,w}}{r_{cf}}\\
\omega_{rl,w} &= \omega_{cf}\frac{r_{rl,w}}{r_{cf}}
\end{aligned} \tag{6.15}$$

Where radius of each single wheel can be calculated as the Eq. 6.11.
The minimum time to travel a curve with a radius of curvature R and a $v_{cf} = 5km/h$ is expressed in the table 6.3.

	Time taken for 360° (sec)	Turning radius (cm)
2WS	5.52	103
4WS	3.07	58

Table 6.3: 2WS and 4WS turning radius and time comparison

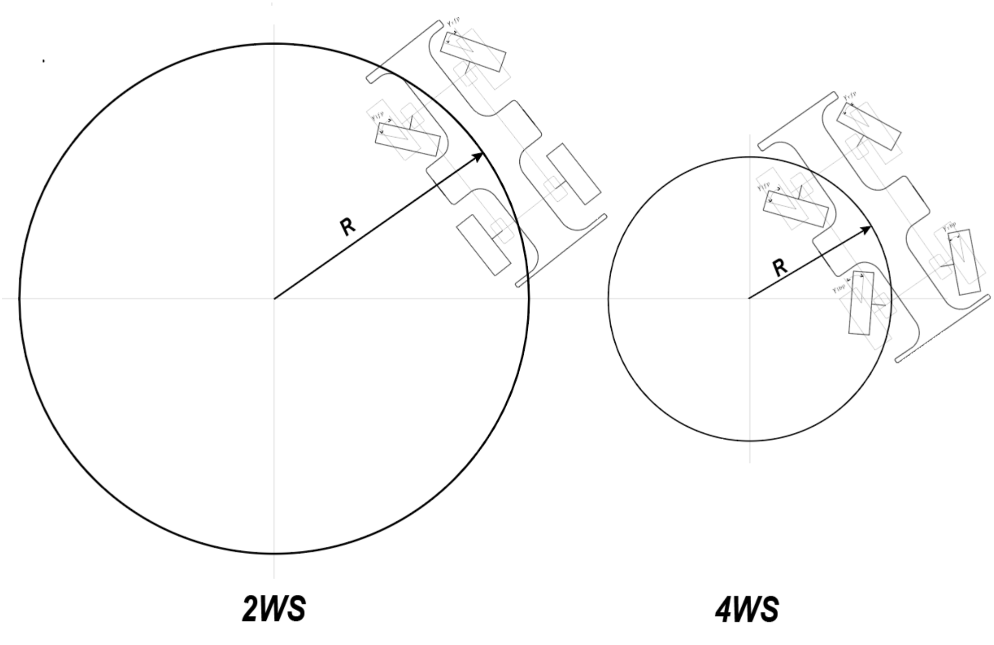

Figure 6.10: Turning radius in 2WS and 4WS robot

6.3 Dynamic approach

The dynamic approach takes into account the forces acting on a vehicle moving along a curved trajectory travelled at constant speed u.

In addition, we introduce the various assumptions made to evaluate the following dynamic equations of the model:

- Vehicle speed V is assumed to be constant;
- Side slip angles are considered to be sufficiently small for consider the linear part of the vehicle dynamics;
- Small wheel steering angles;

On the basis of the above assumptions, a model of vehicle is mathematically formulated. Then we have the following dynamic equilibrium equations in the longitudinal direction, lateral and balance at rotation around the vertical axis of the centre of gravity.

$$\begin{cases} ma_x = F_{F,x}\cos(\delta_F) + F_{R,x}\cos(\delta_R) + F_{F,y}\sin(\delta_F) + F_{R,y}\sin(\delta_R) \\ ma_y = F_{F,y}\cos(\delta_F) + F_{R,y}\cos(\delta_R) + F_{R,x}\sin(\delta_F) + F_{R,x}\sin(\delta_R) \\ J_z\ddot{\psi} = a[F_{F,y}\cos(\delta_F) + F_{F,x}\sin(\delta_F)] - b[F_{R,y}\cos(\delta_R) + F_{R,x}\sin(\delta_R)] \end{cases} \tag{6.16}$$

In cui:

- $\dot{\psi}$ is the angular velocity of the vehicle
- $v = \beta u$
- $F_{F/R,y}$ are the lateral forces born from wheel-ground contact, in this treatment the lateral force has a linear course and takes the form $F_{F/R,y} = C_{f,r}\alpha$ in which C is the sliding stiffness of the tire (coefficient depending on tread stiffness and footprint size)
- J_z the total inertia of the vehicle of mass

The absolute acceleration of the vehicle may be expressed in terms of components along the axles of the reference system integral to the vehicle:

$$a = a_x\mu + a_y v = (\dot{u} - \dot{\psi}v)\mu + (\dot{v} + \dot{\psi}u)v \tag{6.17}$$

It is therefore possible to rewrite it by replacing the expressions of longitudinal and lateral accelerations defined in and recalling the initial assumptions of small steering angles:

It is therefore possible to rewrite 6.16 by replacing the expressions of longitudinal and lateral accelerations defined in 6.17 and recalling the initial assumptions of small steering angles:

$$\begin{cases} m(\dot{u} - \dot{\psi}v) = F_{F,x} + F_{R,x} + F_{F,y}\delta_F + F_{R,y}\delta_R \\ m(\dot{v} + \dot{\psi}u) = F_{F,y} + F_{R,y} + F_{R,x}\delta_F + F_{R,x}\delta_R \\ J_z\ddot{\psi} = a[F_{F,y} + F_{F,x}\delta_F] - b[F_{R,y} + F_{R,x}\delta_R] \end{cases} \tag{6.18}$$

The most classic single-track model uses the last two equilibrium equations and the congruence equations. It is a dynamic system with two state variables.

From simple geometrical considerations and, remembering the relation $F_y = C\alpha$ they obtain the equations of congruence:

$$\begin{cases} \alpha_f = \delta_f - \beta_f = \delta_f - \arctan(\dfrac{v + a\dot{\psi}}{u}) \\ \alpha_r = \delta_r - \beta_r = \delta_r - \arctan(\dfrac{v - b\dot{\psi}}{u}) \end{cases} \tag{6.19}$$

$$\begin{cases} F_{yf} = C_f\alpha_f = C_f(\delta_f - (\dfrac{v + a\dot{\psi}}{u}) \\ F_{yr} = C_r\alpha_r = C_r(\delta_r - (\dfrac{v - b\dot{\psi}}{u}) \end{cases} \tag{6.20}$$

Combining the above equations and recalling the initial hypothesis of small β, which define the longitudinal and lateral velocity components of the centre of gravity as follows:

$$\begin{cases} u = V\cos(\beta) \approx V \\ v = V\sin(\beta) \approx V\beta \end{cases} \tag{6.21}$$

si ottiene il seguente sistema:

$$\begin{cases} m(V\dot{\beta} + \dot{\psi})V = (-C_f - C_r)\beta + (-\dfrac{C_f a}{V} + \dfrac{C_r b}{V})\dot{\psi} + C_f\delta_f + C_r\delta_r \\ J_z\ddot{\psi} = (-C_f a - C_r b)\beta + (-\dfrac{C_f a^2}{V} - \dfrac{C_r b^2}{V})\dot{\psi} + (C_f a)\delta_f - (C_r b)\delta_r \end{cases} \tag{6.22}$$

Referring to State-Space, the equation of the motion of the linear system can be transformed into a set of differential equations of the first order; the typical definition of the space state is written as follows:

$$\begin{cases} \dot{x} = Ax + Bu(t) \\ y = Cx + Du(t) \end{cases} \tag{6.23}$$

Both the vector of states and inputs defined as follows:

$$x = \begin{bmatrix} \beta \\ \dot{\psi} \end{bmatrix} \tag{6.24}$$

$$u(t) = \begin{bmatrix} \delta_f \\ \delta_r \end{bmatrix} \tag{6.25}$$

So it is worth rewriting the 6.22 by explaining the derivatives of the states as a function of the inputs and states:

$$\begin{cases} \dot{\beta} = (\dfrac{-C_f - C_r}{mV})\beta + (\dfrac{-C_f a + C_r b - mV^2}{mV^2})\dot{\psi} + \dfrac{C_f \delta_f + C_r \delta_r}{mV} \\ \ddot{\psi} = (\dfrac{-C_f a - C_r b}{J_z})\beta + (\dfrac{-C_f a^2 - C_r b^2}{J_z V})\dot{\psi} + \dfrac{(C_f a)\delta_f - (C_r b)\delta_r}{J_z} \end{cases} \tag{6.26}$$

We can now define the matrices A, B, C, D of the 6.23 as follow:

$$A = \begin{bmatrix} \dfrac{-C_f - C_r}{mV} & \dfrac{-C_f a + C_r b - mV^2}{mV^2} \\ \dfrac{-C_f a - C_r b}{J_z} & \dfrac{-C_f a^2 - C_r b^2}{J_z V} \end{bmatrix} \tag{6.27}$$

$$B = \begin{bmatrix} \dfrac{C_f}{mV} & \dfrac{C_r}{mV} \\ \dfrac{C_f a}{J_z} & \dfrac{-C_r b}{J_z} \end{bmatrix} \tag{6.28}$$

Before defining the matrices C and D it is necessary to say which are the desired outputs y; to have in output a lot of useful data for the analysis of the system we define:

$$y = \begin{bmatrix} \beta \\ \dot{\psi} \\ \rho \\ \alpha_f \\ \alpha_r \\ a_y \end{bmatrix} \tag{6.29}$$

Where ρ indicates the curvature of the vehicle. Remembering that $\rho = \dfrac{1}{R}$

$$\rho = \frac{(\dot{\psi} + \dot{\beta})}{V} \tag{6.30}$$

So then:

$$C = \begin{bmatrix} 1 & 0 \\ 0 & 1 \\ \dfrac{-C_r - C_f}{mV^2} & \dfrac{-C_f a + C_r b}{mV^3} \\ -1 & \dfrac{-a}{V} \\ -1 & \dfrac{b}{V} \\ \dfrac{-C_r - C_f}{m} & \dfrac{-C_f a + C_r b}{mV} \end{bmatrix} \tag{6.31}$$

$$D = \begin{bmatrix} 0 & 0 \\ 0 & 0 \\ \dfrac{C_f}{mV^2} & \dfrac{C_r}{mV^2} \\ 1 & 0 \\ 0 & 1 \\ \dfrac{C_f}{m} & \dfrac{C_r}{m} \end{bmatrix} \tag{6.32}$$

In order to define the model time response, the system is implemented via Matlab-Simulink software with the following data (Tab. 6.4):

Parameters	Value	Units
m	100	*kg*
a	0,40	*m*
b	0,30	*m*
J_z	160	kgm^2
C_f	52861	*N/rad*
C_r	39156	*N/rad*

Table 6.4: Vehicle parameters

In figure 6.11 the Simulink model used for various steering angles tests are reported.

The model is defined by several subsystems, Fig 6.11. First, you need to define the maneuver; this lock gives output the front and rear steering angles of the bicycle model of the vehicle. They represent the input of the State Space in which is defined the problem in the space of the states described by 6.23 and that returns in output the angle of attitude, speed and acceleration of yaw, the radius of curvature and the front and rear slip angles.

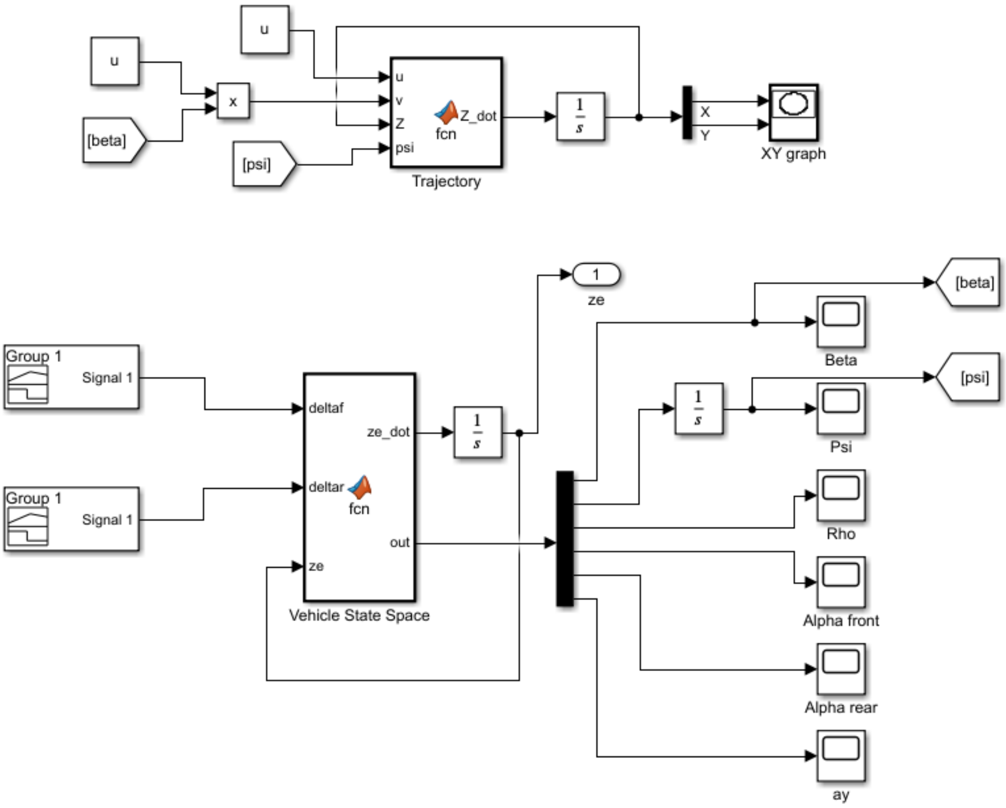

mat

Figure 6.11: Simulink block model at constant speed

In addition, there is a subset in which the trajectory of the vehicle is calculated during the required manoeuvre.

For the calculation of the trajectory it is necessary to insert the vehicle inside the reference system axles body as shown in the figure 6.12 [23].

As it is possible to observe from the diagram brought back in figure, the two variable u and v constitute the members of the absolute speed of the vehicle V along the axes X_b and Y_b of the tern axes body.

By projecting these speeds along the axis of the backhoe axes, it is possible to calculate the absolute speeds along the axes X_e and Y_e and then, through the integration of the two speeds, to obtain the coordinates of the centre of gravity (X, Y) in the reference system fixed to the ground.

$$\begin{cases} X = \int (u \cos\Psi - v \sin\Psi) dt \\ Y = \int (u \sin\Psi - v \cos\Psi) dt \end{cases} \tag{6.33}$$

In order to analyse the lateral behaviour of the vehicle, several simulation tests

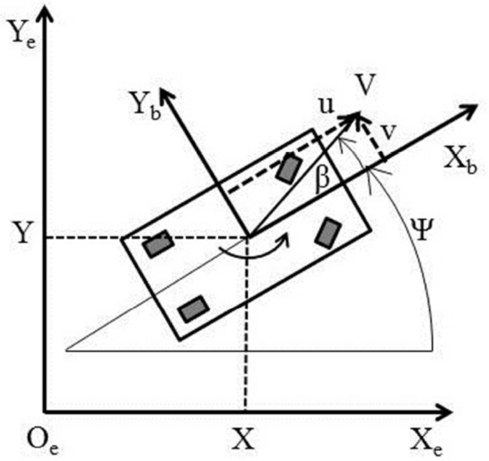

mat

Figure 6.12: Reference systems for vehicle trajectory

are carried out as shown in the following paragraphs.

6.3.1 Test 1: Circular trajectory

The cycling test is useful for analysing the stability of the system at a step input and the transient behaviour of the vehicle.

The manoeuvre consists of:

- Attach the vehicle to a given speed
- When this speed value is reached, a steering angle is applied; this consists in defining a growth of the latter up to a defined maximum value.

6.3.1.1 Speed 30 km/h, steering angle 5°

The first test is carried out by driving the vehicle at its maximum speed. With this test it is possible to understand the maximum steering angle and therefore the maximum radius of curvature that the drone will be able to travel before losing grip when it is at its maximum speed. The vehicle starts with a constant velocity, after an initial straight the vehicle goes into the curve. The steering system changes gradually the direction of the two wheels, starting from zero to the angle required to make the curve with the desired radius.

The trajectory followed by the vehicle is reported in Figure 6.13(a).The maximum steering angle the vehicle can perform when travelling at 30 km/h is 5 degrees. This turning value produces a circular trajectory with a radius equal to 9 meters.

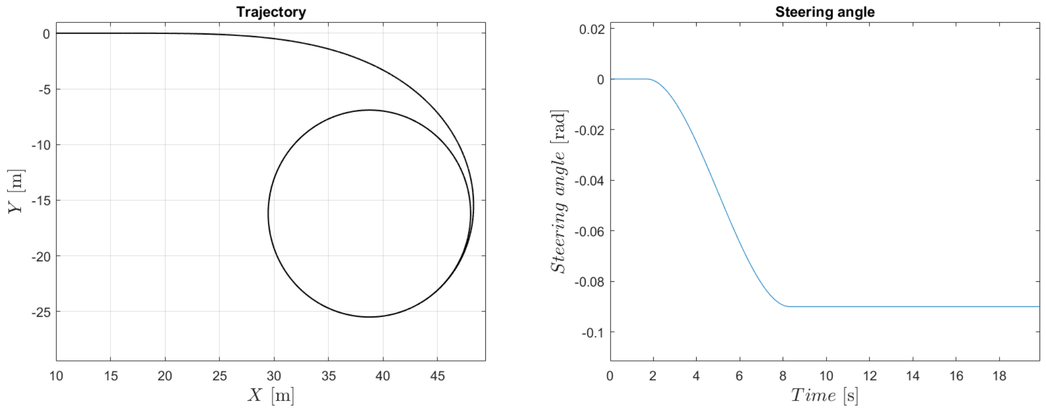

(a) *Circular trajectory* **(b)** *Front steering angle*

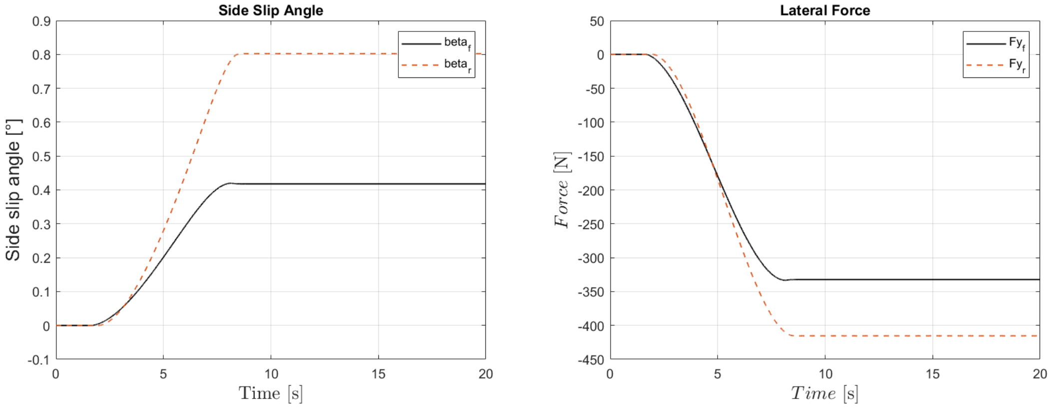

(c) *Front/rear side slip angles* **(d)** *Front/rear lateral forces*

Figure 6.13: Test on circular trajectory at speed 30 km/h and steering angle 5°

Due to the centrifugal force, the external wheels results to be more loaded. For this specific case, a left turn cause an increase of the vertical load on the right side tires. Whereas the vehicle is analysed in the condition in which the load is concentrated in the rear, so the lateral slip angles of the rear wheels are greater and consequently the resulting lateral forces on the rear side will also be greater.

The inner wheel of the front axle due to the low vertical load which is acting on the tire and to the low slip angle, generates a really low lateral force. This effect is higher as far as the speed increases and as far as the radius of curvature is diminished.

6.3.1.2 Speed 10 km/h, steering angle 36°

In this test is examined the maximum speed that the vehicle can travel with its maximum angle is steering without losing grip with the ground. The maximum wheel steering angle due to the servo motor is 40°, whereas the bicycle model of the vehicle is being used, the steering angle of the input will be set to 35 degrees so that the angle of the inner wheel will be 40° and that of the outer wheel 31 degrees, according to Ackermann's model calculations shown in the previous section.

The Simulink-Matlab software shows a maximum admissible speed of 10 km/h to cover the circular trajectory of about 2 meters of diameters resulting from the 35 degree angle set.

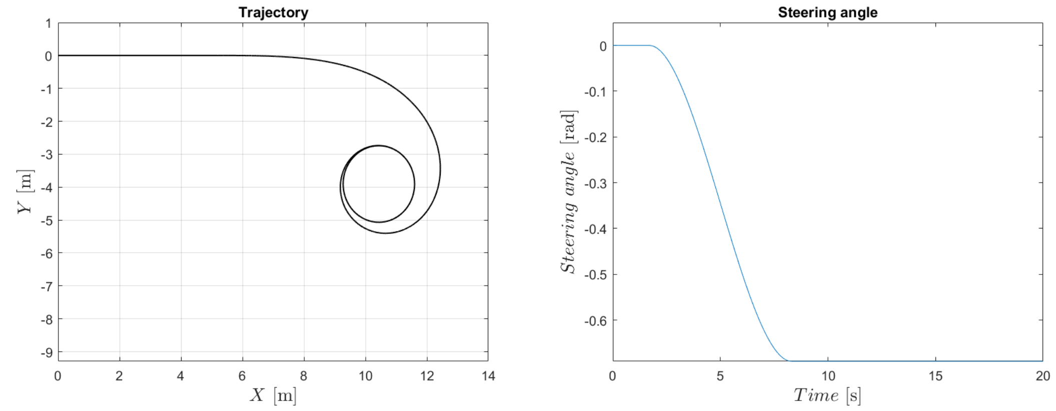

(a) *Circular trajectory* **(b)** *Front steering angle*

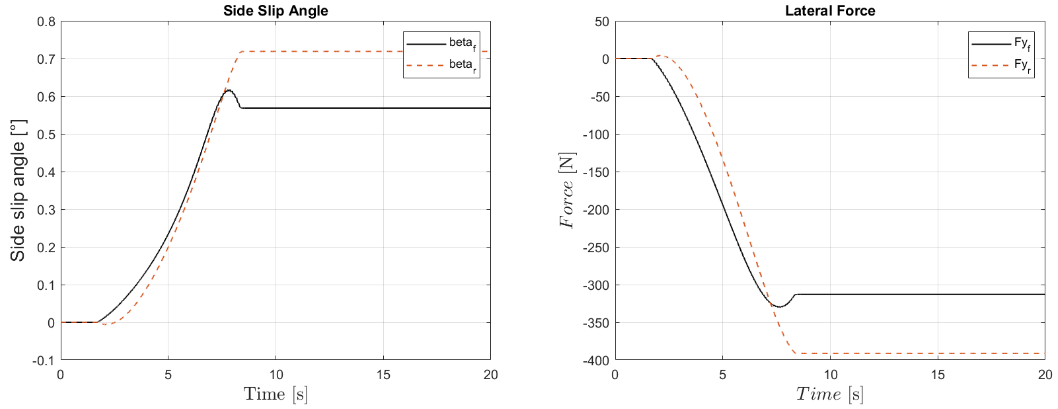

(c) *Front/rear side slip angles* **(d)** *Front/rear lateral forces*

Figure 6.14: Test on circular trajectory at speed 10 km/h and steering angle 36°

As we can see from the figure 6.14 the front side slip angle has been reduced compared to the previous test, while the rear one has increased.

Although the trajectory has been reduced considerably, the lateral forces in play have not varied strongly, this because also the speed has changed to a value much lower.

6.3.1.3 Speed 15 km/h, steering angle 25°

This test is carried out as it simulates a more frequent situation in which the vehicle travels at about its average speed and makes a left turn of 25°. According to Ackermann's bicycle model theory the steering angles of the inner front wheel and the outer front wheel will be 27° and 22° respectively.

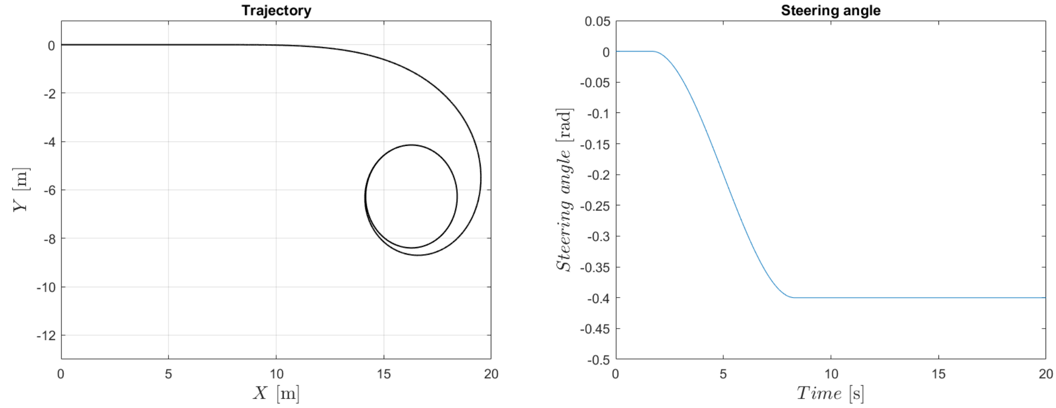

(a) *Circular trajectory* **(b)** *Front steering angle*

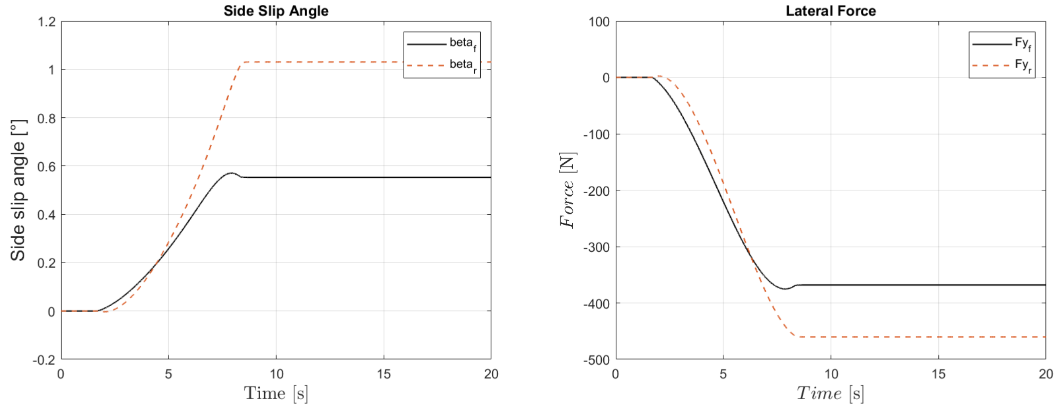

(c) *Front/rear side slip angles* **(d)** *Front/rear lateral forces*

Figure 6.15: Test on circular trajectory at speed 15 km/h and steering angle 25°

6.3.2 Test 2: Moose test

The Moose test consists of a lane change manoeuvre. It is described by the international standard ISO 3888 2 [24], after a revision by the Association of German Automotive Industry (VDA) [25]. The moose test is used to evaluate the handling performance of a vehicle. There is a path to follow, which is described by three cones lanes, where a double lane change is defined. The path needs to be performed at the vehicle maximum speed.

With reference to the normative, the track dimensions for the Moose test are defined in the Table (3.2).

Section	Length of section	Section width
1	15 m	1,1 x vehicle width + 0,25 m
2	30 m	
3	25 m	1,2 x vehicle width + 0,25 m
4	25 m	
5	15 m	1,3 x vehicle width + 0,25 m

Table 6.5: Moose test track dimensions

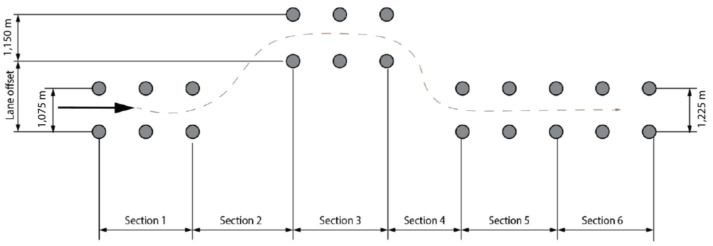

mat

Figure 6.16: Moose test path

In this specific case, the width is equal to 0,75 m and so, the section width results:

- $section1 = 1,1 \cdot 0{,}75 + 0,25 = 1,075$ m
- $section2 = 1,2 \cdot 0{,}75 + 0,25 = 1,150$ m
- $section3 = 1,3 \cdot 0{,}75 + 0,25 = 1,225$ m

After the entrance in the cones, the accelerator pedal is released and so the vehicle is moved only by its own inertia. The test is passed if no cones are hit. Usually the test starts with an initial speed of 60 km/h. The test is repeated many times until the car skids, hits cones, or spins around. Tipically the failure occurs at about 70/80 km/h. In this specific case, since the maximum speed is 30 km/h, the test is performed at the maximum vehicle speed. The test should be passed to demonstrate the safety of itself. Furthermore, since the vehicle without acceleration would be stopped in few meters, it has been tested with an entering speed of 30 km/h that remain constant.

6.3.2.1 Test results

The reproduction of a Moose test into Simulink environment is quite complex since the software is not provided with trajectories available. As consequence, the first task has been to reproduce a possible trajectory. It has been imposed a time dependent equation of motion to the steer and then and this is given as imput to the block model of the figure 6.11 through a signal group block as shown in the figure 6.17

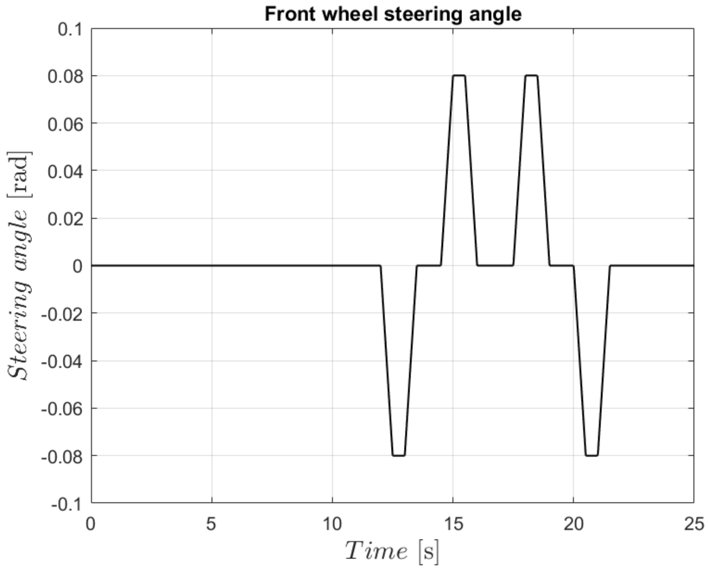

Figure 6.17: Moose test direction

The graph begins with a null angle then begin a series of curves in which the vehicle avoid the contact with the cones. The trajectory of the vehicle with this steering angle input and at its maximum speed is the following (Fig.6.18)

The resultant lateral forces and sideslip angle for each tire are finally shown in Figure (6.19) within the lateral acceleration. In conclusion, the vehicle is able to maintain its trajectory at the maximum speed and the set trajectory does not hit any cone, the test is considered to be passed.

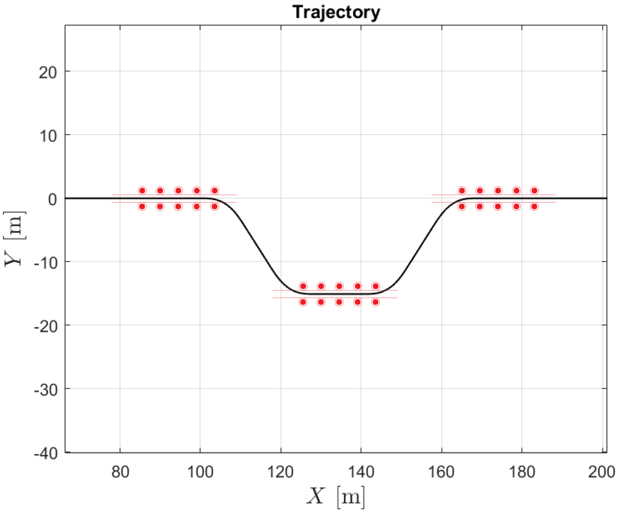

Figure 6.18: Moose test vehicle trajectory

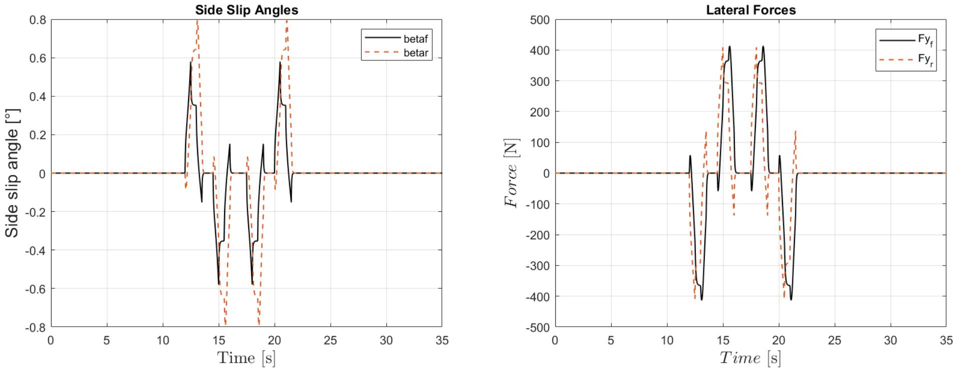

(a) *Front/rear side slip angles* **(b)** *Front/rear lateral forces*

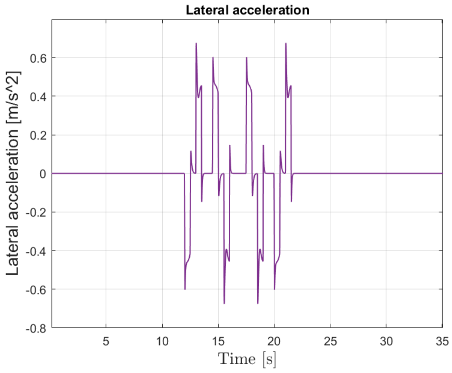

(c) *Lateral acceleration*

Figure 6.19: Moose Test lateral tire forces, side slip angles and lateral acceleration

Chapter 7

Conclusion and future work

At this point in the discussion, it is possible to analyse whether the project requirements have been met and if the results are satisfactory.

The aim of this thesis was to introduce a contribution to a growing activity such as deliveries for online purchases through the development of an innovative concept that brings improvements to the existing system of parcel distribution.

The goals of sustainability and efficiency were first achieved with the choice of a 100% electric and secondly, with the adoption of multiple technologies necessary to make accurate and reliable all the activities carried out by the Robot during its mission.

The obtained rover is constituted from the set of simple technologies easy implementable: the propulsion present in independent way in every wheel allows the absence of a motor gear and a transmission and doesn't preview the presence of differentials, the adoption of a simple and 4WS type steering system makes the rover easy to maneuver and able to make trajectories characterized by radii of curvature not too high, the entire structure, moreover, is simple and easily achievable.

The design process was shown to provide satisfactory results. Kinematic/Dynamic simulation models for the Pacci robot with passive suspension system have been developed and implemented in the MATLAB/Simulink environment with validation results.Robot dynamic stability had been improved with the proposed suspension design in the simulation environment.The robot state-space dynamic model for steering performance had been estimated with various tests.

In future work the robot model should be validated against real-world experiment data. Experimental tests could be carried out to demonstrate the efficiency and quantified performance of the proposed mathematical model and estimation approach. For example with the exact value of tire cornering stiffness a more precise tire model could be used, like the Pacejka model [23], introducing the coefficient calculated from a lateral tire slip test.A fair comparison between robots should be done with experiments that include identical deliveries executed with various robots.

This research can be considered as a launching point for introducing agile wheeled robot, which has the capabilities to adapt and interact with road irregularities. The following direction could be pursued improving the suspension dynamics by adding a powerful actuator that has high speed/force capabilities.

Another idea that could be developed is the possible presence of a photovoltaic panel on the top. Considering that the battery consumption is greatly influenced by all the accessories of which the drone is equipped, sensors useful for navigation (GPS antenna, lidar sensors) and for monitoring (infrared sensors, stereo cameras), the photovoltaic panel would be useful to feed them. An alternative for auxiliary power consumption is using sleep-mode for sensors and computation hardware, so also this aspect should be studied.

In a future society where buses will also be fully electric vehicles, and will therefore be structurally rethought, It will be possible to think about eliminating the additional rack in the back and build a special space for delivery robots under the seats of the bus itself.

Being a thesis born in collaboration with other engineers and designers it deals with the mechanical design of the drone, while the localization system, autonomous driving and robot control strategies will be analysed in a second thesis work directly related to this that develop a high-level control algorithm which allows the robot to operate autonomously.

At the end of this elaboration it is, therefore, possible, to affirm that the project presented, although it concerns a rover not yet realized, shows that the objective of obtaining a delivery system more and more precise, efficient and above all sustainable, it is easy to pursue, both in terms of accessibility to technologies and in terms of costs. The performance of the vehicle can undoubtedly be improved by modifying some of the technologies listed above, while keeping them simple and easily available at the expense of costs. All this, however, always taking into account that the success of delivery robots in particular not only depends on the energy efficiency but also on the public acceptance. A better efficiency robot might not be as widely accepted as another that is more aesthetically pleasing or which behaves in a way that better blends in with the people flow.

Bibliography

[1] Thomas Earl, Veronica Aneris, Heather Brooks, Carlos Calvo Ambel, and Lucien Mathieu. «Transport Environment (2019) Emission Reduction Strategies for the Transport Sector in Italy». In: (Jan. 2019) (cit. on p. 2).

[2] Ghajargar, M. Zenezini, and G. Montanaro. «Home delivery services: innovations and emerging needs». In: *IFAC-PapersOnLine* 49.12 (2016), pp. 1371–1376 (cit. on p. 8).

[3] Lund, S. Madgavkar, A. Manyika, J. Smit, S. Ellingrud, K. Meaney, and M. Robinson. «The Future of Work After COVID-19». In: *Tech. Rep. McKinsey Global Institute* (2021) (cit. on p. 8).

[4] Ahuja, K. Chandra, and V. Lord. «The rapid evolution of food delivery». In: *Tech. Rep. McKinsey Company* (2021) (cit. on p. 8).

[5] Pishue B. «US Traffic Hot Spots: Measuring the Impact of Congestion in the United States». In: *Tech. Rep. Transport Research International Documentation* (2017) (cit. on p. 9).

[6] Simoni M.D.and Kutanoglu E. and Claudel C.G. «Optimization and analysis of a robot-assisted last mile delivery system». In: *Transp. Res. E Logist. Transp. Rev.* 142.102049 (2020) (cit. on p. 10).

[7] Jennings D. and Figliozzi M. «Study of road autonomous delivery robots and their potential effects on freight efficiency and travel». In: *Transp. Res. Rec. J. Transp.* 9.2674 (2020), pp. 1019–1029 (cit. on pp. 10, 15).

[8] Starship. «Starship Technologies launches pilot program with Domino's Pizza Enterprises». In: (Accessed July 25 2018) (cit. on p. 13).

[9] Dolan S. «The Challenges of Last Mile Delivery Logistics and the Tech Solutions Cutting Costs in the Final Mile». In: *Business Insider* (Mar. 2021) (cit. on p. 16).

[10] Joerss M., Schröder J.and Neuhaus F., Klink C., and Mann F. «Parcel Delivery: The Future of Last Mile». In: *McKinsey Company* (Brussels 2016), pp. 1–32 (cit. on p. 16).

[11] T. D. Gillespie. «Fundamentals of vehicle dynamics (Society of Automotive Engineers - SAE)». In: (1992) (cit. on p. 22).

[12] R. N. Jazar. «Vehicle Dynamics. Theory and Applications». In: *Springer Science + Business Media* (2008) (cit. on p. 22).

[13] W. Tong. «Mechanical design of electric motors». In: *CRC Press* (2014) (cit. on p. 25).

[14] N. P. Quang and Dittrich et al. «Vector control of three-phase AC machines». In: *Springer* (2008), p. 24 (cit. on p. 32).

[15] Felix-A. LeBel, Louis Pelletier, Pascal Messier, and Jo ao Pedro Trov ao. «Battery Pack Sizing Method - Case Study of an Electric Motorcycle». In: *Centre de Technologies Avancees (CTA-BRP-UdeS)/ e-TESC Laboratory Faculty of Engineering - Universite de Sherbrooke* () (cit. on p. 37).

[16] P. Nelson, R.Vijayagopal, K. Gallagher, and A. Rousseau. «Sizing the Battery Power for PHEVs Based on Battery Efficiency, Cost and Operational Cost Savings». In: EVS27 Symposium Barcelona, Spain (Nov. 2013), pp. 569–571 (cit. on p. 37).

[17] Z. Junzhi, L. Yutong, and L. Chen. «New regenerative braking control strategy for reardriven electrified minivans». In: *Energy Conversion and Management* 82 (2014), pp. 135–145 (cit. on p. 45).

[18] Gigih Priyandoko and Goegoes Dwi Nusantoro. «PID State Feedback Controller of a Quarter Car Active Suspension System». In: (Nov. 2011) (cit. on p. 55).

[19] ISO-8608. «Mechanical vibration - road surface profiles - reporting of measured data». In: (1995) (cit. on p. 66).

[20] M. Agostinacchio, D. Ciampa, and S. Olita. «The vibrations induced by surface irregularities in road pavements a matlab R approach». In: *European Transport Research Review* 6(3) (2014), pp. 267–275 (cit. on p. 67).

[21] Gysen B. L. J., Janssen J. L. G., Paulides J. J. H., and Lomonova. «Design aspects of an active electromagnetic suspension system for automotive applications Efficiency, Cost and Operational Cost Savings». In: IEEE Transactions on Industry Applications, 45(5) (2009), pp. 1589–1597 (cit. on p. 71).

[22] William F Milliken and Douglas L Milliken. «Race car vehicle dynamics». In: *Society of Automotive Engineers Warrendale* 400 (1995) (cit. on p. 81).

[23] Ing. Gabriele Vandi. «Simulazione dinamica di un veicolo dotato di powertrain ibrido endotermico-elettrico». In: *Dottorato di ricerca in Meccanica e Scienze Avanzate Dell'Ingegneria Ingegneria delle Macchine e dei Sistemi Energetici* (2015) (cit. on p. 90).

[24] ISO 3888-2. «Passenger cars – Test track for a severe lane-change manoeuvre». In: (2011) (cit. on p. 95).

[25] VEHICO GmbH. «ISO Double Lane Change Test». In: (2017) (cit. on p. 95).